Control and Stability of Residential Microgrids with Grid-Forming Prosumers

Bowen Wang

Centre for Future Energy Networks

School of Electrical and Information Engineering

Faculty of Engineering

The University of Sydney

Candidate's ORCID

A thesis submitted to fulfil requirements for the degree of

Doctor of Philosophy

January 2022

For my family.

Statement of originality

I hereby declare that except where specific reference is made to the work of others, the contents of this dissertation are original and have not been submitted in whole or in part for consideration for any other degree or qualification in this, or any other university. This dissertation is my own work and contains nothing which is the outcome of work done in collaboration with others, except as specified in the text and Acknowledgements. This dissertation contains fewer than 50,000 words including appendices, bibliography, footnotes, tables and equations and has fewer than 100 figures.

Bowen Wang
August 2021

Acknowledgments

First of all, I would like to express my gratitude and acknowledgement to all my teachers and professors, all of whom stimulated my growth and inspired my passion to work towards the dream of a sustainable future. In particular, I would like to thank my supervisor, Dr. Gregor Verbič. You oriented me in the world of the smart power grid and sustainable energy. It is my great honour to be under your supervision. It means a lot to me. I would also like to express my gratitude to my auxiliary supervisors Dr. Weidong Xiao and Dr. Archie C Chapman, who continuously supported my research and whose comments, advice and encouragement have always been of much help. Additionally, I also want to give my thank to Dr. Jin Ma and Dr. Sinan Li who often offered me help when I felt confused.

I would also like to thank my colleagues in the Centre for Future Energy Networks at The University of Sydney. I personally know how crippling the lack of a support network can be, and you have all offered an amazing environment for our research to flourish. Yiju, Daniel, Jaysson, Donald, Zahra, Yifan, Yu, and visiting students Mitja and Fynn, have all been great friends which I'm very glad to have crossed paths. The same applied to researchers from other groups but with whom I also had the opportunity to bond, in particular Yuezhu, Samir, Huishi, Diwei, Feng, Zhengyang, and Mohammad.

Moreover, I would like to thank all my friends whom I met in China and Australia, and to all of them who offered support in the means of conversation a most sincere thank you, in particular Shufeng, Charles and Hestina. Special attention goes to Baoying, who has been my great friend since my bachelor study. Baoying came to the Sydney Uni in 2013, since when he offered me much information about the study and research environment here. I would not have started this adventure without his help.

In addition, I would like to thank The University of Sydney for providing me with financial assistance with the University of Sydney International Scholarship, and the School of Electrical and Information Engineering for the 2019 Norman I Price scholarship.

For my students throughout the three years of tutoring, I appreciate your vote of confidence and receptive attitude towards my enthusiastic teaching methods - and also thank you for your feedback. I hope my teaching has made a positive impact on each and all of you.

I also believe I must thank the reviewers for my work, both current examiners of this thesis and previous reviewers for my papers. I greatly appreciate all feedback provided towards improving my work.

Most importantly, I would thank the support from my family. My parents kept encouraging me during my Ph.D. research, relieving me from pressure and motivating me to get through all difficulties. They have always been expecting me to get further in my study and to become wealthy in knowledge, and this is why they named me “Bowen” which denotes “knowledgable” and “wise” in my mother language. I will always keep this in mind, orienting myself to be a better person. Specifically, I want to thank my girlfriend, or I can say my fiancee, Xindan Wang, whom I have already treated like my family. We met and fell in love in Sydney in the second year of my Ph.D. journey, from when I felt like meeting the one I have been waiting for for years. I cannot describe how tough this journey is especially when we think about the COVID-19 outbreak amid these years. Staying at home and friends drifting apart brought loneliness, but there is nothing I can do about it. When I look back on this journey, it is Xindan who always kept me company. It is hard for me to say how grateful I am to have her around me. It means a lot to me and I will never take it for granted.

Lastly, I would like to dedicate my thesis to all of mankind, and I hope we can move on towards a truly equal and sustainable future, away from secular practises which are negligent towards others or the environment.

Abstract

The rise of the prosumers (*pro*ducers-con*sumers*), residential customers equipped with behind-the-meter distributed energy resources (DER), such as battery storage and rooftop solar PV, offers an opportunity to use prosumer-owned DER innovatively. The thesis rests on the premise that prosumers equipped with grid-forming inverters can not only provide inertia to improve the frequency performance of the bulk grid but also support islanded operation of residential microgrids (low-voltage distribution feeder operated in an islanded mode), which can improve distribution grids' resilience and reliability without purposely designing low-voltage (LV) distribution feeders as microgrids.

Today, grid-following control is predominantly used to control prosumer DER, by which the prosumers behave as controlled current sources. These grid-following prosumers deliver active and reactive power by staying synchronized with the existing grid. However, they cannot operate if disconnected from the main grid due to the lack of voltage reference. This gives rise to the increasing interest in the use of grid-forming power converters, by which the prosumers behave as voltage sources. Grid-forming converters regulate their output voltage according to the reference of their own and exhibit load sharing with other prosumers even in islanded operation. Making use of grid-forming prosumers opens up opportunities to improve distribution grids' resilience and enhance the genuine inertia of highly renewable-penetrated power systems.

Firstly, electricity networks in many regional communities are prone to frequent power outages. Instead of purposely designing the community as a microgrid with dedicated grid-forming equipment, the LV feeder can be turned into a residential microgrid with multiple paralleled grid-forming prosumers. In this case, the LV feeder can operate in both grid-connected and islanded modes. Secondly, grid-forming prosumers in the residential microgrid behave as voltage sources that respond naturally to the varying loads in the system. This is much like synchronous machines extracting kinetic energy from rotating masses. "Genuine" system inertia is thus enhanced, which is fundamentally different from the "emulated" inertia by fast frequency response (FFR) from grid-following converters.

Against this backdrop, this thesis mainly focuses on two aspects. The first is the small-signal stability of such residential microgrids. In particular, the impact of the increasing number of grid-forming prosumers is studied based on the linearised model. The impact of the various dynamic response of primary sources is also investigated. The second is the control of the grid-forming prosumers aiming to provide sufficient inertia for the system. The control is focused on both the inverters and the DC-stage converters. Specifically, the thesis proposes an advanced controller for the DC-stage converters based on active disturbance rejection control (ADRC), which observes and rejects the "total disturbance" of the system, thereby enhancing the inertial response provided by prosumer DER. In addition, to make better use of the energy from prosumer-owned DER, an adaptive droop controller based on a piecewise power function is proposed, which ensures that residential ESS provide little power in the steady state while supplying sufficient power to cater for the demand variation during the transient state. Proposed strategies are verified by time-domain simulations.

Publications included in this thesis

I made a number of contributions in the papers listed below where I was the lead author in two journal articles and two conference publications.

Journal Articles

[JA1] **B. Wang** and G. Verbič, "Stability Analysis of Low-voltage Distribution Feeders Operated as Islanded Microgrids", *IEEE Transactions on Smart Grid*, vol. 12, no. 6, pp. 4681-4689, Nov. 2021.

Contributions made in this paper are incorporated in Chapters 2 and 4

Contributors	Modeling	Analysing the results	Writing the paper
B. Wang	90%	90%	70%
G. Verbič	10%	10%	30%

[JA2] **B. Wang**, G. Verbič, W. Xiao, and A. C. Chapman, "Enhanced battery controller for inertia support in residential microgrid based on active disturbance rejection control", *Electric Power Systems Research*, Volume 189, 2020.

Contributions made in this paper are incorporated in Chapters 2 and 6

Contributors	Modeling	Analysing the results	Writing the paper
B. Wang	90%	90%	70%
Others	10%	10%	30%

Conference Proceedings

[CP1] **B. Wang**, G. Verbič, and W. Xiao, "Power Sharing in an Islanded LV Distribution Network Fully Installed with PV-Battery Systems Based on Grid-Forming Control", *International Conference on Smart Grids and Energy Systems* (SGES 2020), Perth, Australia, November 2020.

Contributions made in this paper are incorporated in Chapters 2 and 3

Contributors	Modeling	Analysing the results	Writing the paper
B. Wang	90%	80%	70%
Others	10%	20%	30%

[CP2] **B. Wang**, G. Verbič, and A. C. Chapman, "Control Scheme for Bidirectional DC/DC Converter in PV-battery System based on Active Disturbance Rejection Control", *2018 Australasian Universities Power Engineering Conference* (AUPEC), Auckland, New Zealand, November 2018.

Contributions made in this paper are incorporated in Chapters 3 and 5

Contributors	Modeling	Analysing the results	Writing the paper
B. Wang	90%	80%	70%
Others	10%	20%	30%

Table of contents

List of Figures

List of Tables

Nomenclature

Sets

$\boldsymbol{x}$ Matrix variables

x Single variables

Δx Small-signal variations

$\dot{x}$ Derivative variables

x^* Reference values

X Steady-state operating values

Abbreviations

AC Alternating current.

ADRC Active disturbance rejection control.

BDC Bidirectional DC/DC converter.

CIG Converter interfaced generations.

DC Direct current.

DER Distributed energy resources.

DFIG Double-fed induciton generator.

DG Distributed generation.

DSTATCOM Distribution static synchronous compensator.

EMS Energy management system.

ESS Eenrgy storage systems.

FACTS Flexible alternating current transmission system.

FFR Fast frequency response.

FLL Frequency-locked loop.

HIL Hardware-in-the-loop.

HVDC High-voltage direct current.

IM Induction motor.

LV Low-voltage.

MPC Model predictive control.

MPP Maximum power point.

MPPT Maximum power point tracking.

MV Medium-voltage.

P&O Perturb and Observe.

PCC Point of coupling connection.

PI Proportional-integral.

PID Proportional-integral-derivative.

PLL Phase-locked loop.

PR Proportional-resonanct.

PV Photovoltaic.

PWM Pulse width modulation.

RES Renewable energy sources.

RoCoF Rate of Change of Frequency.

SG Synchronous generators.

SM Synchronous machine.

SMC Sliding mode control.

SOC State of charge.

SOGI Second order generalized integrator.

SPWM Sinusoidal pulse width modulation.

SVM Space vector modulation.

TD Transfer delay.

VOC Virtual oscillator.

VSG Virtual synchronous generator.

VSM Virtual synchronous machine.

Chapter 1

Introduction

1.1 Background and motivation

Increasing penetration of renewable energy sources (RES) is being observed amid the progressive transition of the electricity grid. Breaking the dependence on the use of fossil fuels in conventional power systems have been globally recognized as a must-do business mainly due to the environmental concern. As a result, the investment in clean energy transition accelerated in recent years and is expected to continue. In Australia, for example, the proportion of the electricity coming from clean energy sources increased from 17% to more than 27% from 2016 to 2020, with wind and rooftop solar leading the way [3].

Over the past 5 years, prices of rooftop PV installation have continued to decrease dramatically [4]. Many people in the solar industry expect the price of solar systems to continue to decline. This fact, together with the incentive policies supported by the government, have been changing the preferences of household energy consumers [5]. At the distribution level, residents have been increasingly installing rooftop PVs in their homes for the sake of both environmental commitment and economic benefits. According to [3], in 2020, Australia reported 378,451 new installations of rooftop solar systems throughout the year, easily beating the previous record of 283,952 in 2019. This new scenario changed the residents into prosumers (*pro*ducers-con*sumers*) who feed their excessive produced energy to the grid during the peak time [2]. Along with their rooftop solar systems, many prosumers also invest in energy storage systems (ESS) such as home batteries, fuel cells and micro-turbines. The emergence of such PV-ESS systems allows prosumers to store electricity from solar panels during the day for using it at night during which the electricity price is higher, reducing the reliance on the grid and thus reducing their electricity bills. For instance, the investment in residential battery storage across Australia has been increased from 7,500 installed systems in 2016 to 23,796 in 2020 [3]. Australian households' enthusiasm for batteries continues to build with the significant reduction in the cost.

Prosumers with PV-ESS systems are interfaced with the grid via power converters. Traditionally, these prosumers are integrated as controlled-current sources, which deliver active and reactive power to the network (known as *grid-following* mode). Power converters with grid-following control methods measure the frequency of the existing grid and then stay synchronized with it. However, these prosumers cannot operate without the grid because they lack the voltage reference. Comparatively, the other mode named *grid-forming* power converters keeps attracting the interest of researchers and inverter manufacturers [1]. Instead of being integrated as controlled-current sources, grid-forming power converters act as voltage sources. These converters set the voltage reference of their own and thus regulate the voltage with proper power sharing techniques and improved frequency response. Prosumers, when interfaced by grid-forming power converters, are enabled to provide many important services for the grid.

One of the services is to improve the resiliency of the low-voltage (LV) distribution feeder, especially in remote areas. The fact is that regional communities who depend on long stretches of powerlines connected to the electricity network easily experience power outages. Designing the LV network of such a community as an AC microgrid is an advanced solution due to its ability to conduct both grid-connected and isolated operations. To make this happen, a dedicated central generation such as a diesel generator or a large voltage-controlled battery can be installed near the community, powering the region during a loss of the main network. Such is the case in a Western Australian tourism city Kalbarri, whose LV network is designed as a microgrid with solars, wind farms and a battery energy storage system [6]. The battery operates as the dedicated generation by working as a voltage source. Normally, the network is supplied by the utility grid. Once the grid is lost either intentionally or contingently, the battery storage system starts to regulate the voltage and frequency on its own, providing reference to the rest power units along the feeder. At present, however, with the increasing number of prosumers installed by PV-ESS systems, a different way to solve the risk of a complete power outage is provided, which is to make prosumers interfaced by grid-forming power converters to the common feeder. Most inverters for small-capacity ESS own grid-forming mode. Instead of installing the dedicated infrastructures, prosumers can take advantage of their residential ESS to provide the voltage reference independently and share the loads. This is simple to be realized by shifting inverters to grid-forming mode along with power sharing techniques without changing the hardware. In this case, the LV network of the community is operated as a *residential microgrid*. Even though it is mostly operating in connection with the main grid, the resiliency is significantly improved by the voltage-sourced residential ESS who tide the community over the grid loss while the fix is happening.

In addition to this, these grid-forming prosumers offer the potential to improve the *genuine* inertia for the system. It is widely accepted that many modern electricity grids have the issue of low inertia due to the increasing replacement of conventional synchronous-generator-based power plants by distributed RES. In a conventional power system, inertia comes from the kinetic energy stored in the rotating masses of synchronous generators, which serves as an immediate source of energy that reduces frequency excursions following power imbalance. Most unconventional RES (e.g. wind and solar), however, provide no inherent inertial response in case of system disturbance as they depend on power electronic interfaces. Consequently, power systems dominated by inverter-interfaced generation would experience a high rate of change of frequency (RoCoF) immediately after a disturbance. As large system inertia is attributed to the large and instant power supplied by the kinetic energy of synchronous machines, a possible solution in inverter-dominated power systems is to provide fast frequency response (FFR) to the grid using RES. Due to the responsiveness of power electronic converters, FFR can be activated much faster than primary frequency response. The problem is that FFR traditionally provided by grid-following converters require a phase-locked loop (PLL) to measure the frequency, which introduces a time delay in the order of a few hundred milliseconds. Therefore, FFR is slower than inertial response because it cannot respond naturally to a disturbance. In comparison, grid-forming converters acting as voltage sources inherently respond to the changes in the loads. This is made possible by *extracting* energy from the DC-link capacitor much like synchronous machines extract kinetic energy from rotating masses. As a result, a genuine inertial response compared to a *synthetic* one provided by FFR. Accordingly, the energy stored in the DC-link capacitor can be regarded as equivalent to the rotor of a synchronous generator that serves as immediate energy storage to the grid, and thereby the genuine inertia is improved. The issue is that this energy is limited, so it needs to be augmented by an additional energy source such as a battery or a supercapacitor. Under this backdrop, the emergence of these grid-forming prosumers solves this issue as the ESS installed locally broadens the DC-link capacity. The point is how to implement the controller.

1.2 Research questions

1.2.1 Stability of LV feeders operated as residential microgrids

As explained before, the LV feeder can be designed as a residential microgrid to improve the resiliency of the LV distribution network. So it should be ensured that the LV feeder can transit from the grid-connected mode to islanded mode stably, and this requires the study of the dynamics immediately after the network separation in order to ensure stability. This includes the transient stability issue caused by the network separation and the small-signal stability issue resulted from the short-term small disturbance after the separation, which can be investigated by time-domain simulations and eigenvalue analysis of the linearised small-signal model, respectively.

It is known that LV networks mostly shape as radial networks due to the simplicity of design and implementation. Grid-forming prosumers can be integrated into the common feeder at their nearest nodes. Rich literature on the small-signal stability of microgrids mostly focuses on the influence resulted from the controller parameters, the types of loads and the modelling process. However, less attention has been paid to the impact of the topology, or in other words, how the system stability is influenced by the increasing number of grid-forming prosumers. As small-signal stability is highly related to the feedback controllers of the power converter, these grid-forming inverters need to be explicitly modelled in order to conduct the eigenvalue analysis.

In addition to that, multiple types of ESS exist in residential applications, such as supercapacitors, batteries, fuel cells, micro-turbines, etc. These primary sources, however, feature various dynamic responses, resulting in different levels of response speed. After the network separation, all loads in the system should be supplied by the prosumer-owned DER. Hence sufficient power is expected to be provided by the grid-forming inverters immediately after a system disturbance. However, some primary sources such as micro-turbines and fuel cells cannot provide instantaneous power due to their limited dynamic performance for load tracking. Dynamic response of fast ESS such as batteries is also diverse by the different types. Against this backdrop, the various dynamic response speeds from the primary sources may impact the microgrid stability.

As a result, in the scenario where the LV feeder is designed as a residential microgrid, it is crucial to study the impact from the increasing number of grid-forming prosumers and from the various dynamic response time of primary sources on the small-signal stability during islanded operation.

1.2.2 Advanced control of the DC-stage converter

On the DC side of the prosumer, DC-stage converters are often implemented to cater for the bidirectional power flow, optimal power extraction and DC-link voltage level. The controller of the DC-stage converter can also be enabled to regulate the DC-link voltage. To ensure the fast response from the ESS, the DC-stage converter controller should properly regulate the DC-link voltage to an expected reference, thus providing adequate power compensation for the varying loads. This requires advanced control of the DC-stage converter with requirements on fast response and disturbance rejection performance.

Conventional PI-based controllers for the DC-stage converter are based on the linearised small-signal model of the converter at a specific operating point. To make prosumer-owned DER provide FFR for inertia enhancement, the DC-stage converter should cater for fast power supply subject to large load disturbance, by which conventional linearised controllers might be unstable and ineffective. Therefore, advanced control methods which do not depend on the linearised model and feature effective disturbance rejection ability should be applied to control the DC-stage converter.

1.2.3 Using grid-forming prosumers to provide genuine inertia

As introduced at the beginning of this chapter, genuine inertia can be improved by the integration of grid-forming prosumers due to the fact that these voltage-controlled generation sources respond naturally to the load change of the system. There exist multiple types of grid-forming methods, which is to be introduced in Chapter 2. As grid-forming prosumers provide genuine inertia in the form of extracting the energy in the DC-link capacitor which is determined by the DC-link voltage, the relations between the DC-link voltage and the output frequency are expected to be considered when implementing the grid-forming approach to the inverter.

Moreover, on the DC side of the prosumer, ESS conducts the bidirectional power flow between the DC side and the grid. To enhance the inertial response, ESS should augment the limited capacity of the DC-link capacitor with a very fast response in case the capacitor is over-discharged which deteriorates the stability. This can be fulfilled by the DC-link voltage control. Therefore, cooperation of the DC-link control and the grid-forming approach is expected to be studied. The power sharing approach, on the other hand, should consider not only the proper frequency regulation but also the transients during the inertial response, in order to provide sufficient inertia for the system.

Power converters have a much faster response than conventional synchronous generators. Hence, the inertial response provided by the grid-forming inverters can be different. By comparing the inertial response from grid-forming inverters and generators, inertial enhancement strategies can be proposed to improve the inertial response of the integrated system.

In terms of the control of grid-forming inverters aiming to provide inertia, to make better use of the prosumer-owned ESS, it is expected that the ESS provide almost no power during the steady state and that they contribute to a large amount of power supply during demand variation. So the controller should feature adaptiveness according to the system condition.

1.2.4 Questions to be discussed

More specifically, this thesis aims to answer the following research questions:
Stability of residential microgrids

- Can a grid-connected LV feeder transition to an islanded residential microgrid stably with all prosumers integrated by grid-forming power converters?
- How is the small-signal stability of an islanded residential microgrid affected by the increasing number of grid-forming prosumers? What is the cause of the effect?
- Since the small-signal stability is highly related to the feedback controllers of power converters, how do the relevant controller parameters affect the stability? How is the stability enhanced or weakened by parameter adjustment?
- Is the stability related to the dynamic response time from the primary sources? How does the various dynamic responses influence the stability?

Control of grid-forming prosumers for inertia enhancement

- Can grid-forming converters provide genuine inertia like synchronous generators' physical inertia to improve the frequency response? How is the inertial response of grid-forming converters like?
- To make better use of the prosumer-owned DER, how to design the controller of grid-forming prosumers to make sure that a large amount of power is supplied by the residential ESS during demand variation while almost no power is provided from them during the steady state?
- Does increasing number of grid-forming prosumers help with the inertia support? How is the inertial response change by adding more grid-forming converters?

1.3 Thesis outline

This thesis begins with an introductory chapter, giving the current scenario of residential DER integration. Research questions are thus being proposed based on the idea of operating a LV feeder as a residential microgrid. Next, a literature review in Chapter 2 describes the relevant research of the main topics in this thesis, starting with the introduction and control in residential microgrids. Then, various types and control approaches of power converters are discussed, followed by a review of power sharing methods applied in DER. Studies on microgrid stability are then discussed. In particular, the low-inertia situation of many modern power systems is reviewed, along with relevant research on inertia enhancement strategies.

The manuscript continues with the explanation of the control structures for grid-forming power converters which are used in this thesis in Chapter 3. This can be divided into three aspects: the inverter control, the DC-stage converter control, and the control of the single-phase grid-forming prosumer. The inverter controller is being implemented by the grid-forming approaches. Specifically, the P/Q droop method and the matching control are applied in this thesis. Controllers for the DC-stage converters are discussed then. As prosumers typically use single-phase connections, the controller of single-phase grid-forming inverters is derived from the control structure of the three-phase one, with extra modification units added. After that, the chapter provides a case study of power sharing in an islanded residential microgrid based on matching and power sharing methods. This explains in detail how grid-forming and power sharing functionalities are validated by the controllers of both the inverter and the DC-stage converters.

After the basic control methods are discussed, Chapter 4 continues with the stability analysis of the islanded residential microgrid. The analysis focuses on the impact of microgrid expansion and the dynamic response time from the primary DC sources, which attracts less attention in the existing literature. The impact of microgrid expansion is first studied by explicitly modelling the grid-forming inverters and the feeder network. The eigenvalue analysis shows that with the increasing number of grid-forming inverters, the system becomes "practically unstable" with its critical eigenvalue approaching zero as progressively more inverters are added. After that, the analysis is extended by explicitly modelling the DC side dynamics, including the DC/DC converter with its controller and the inherent dynamic response of the DC energy source. Eigenvalue analysis shows that the DC voltage controller impacts the system stability by introducing new dominant eigenvalues. Also, the results suggest that the DC energy source should have a fast response to ensure a stable operation. The small-signal stability results, benchmarked against time-domain simulations, indicate that careful parameter tuning is required to ensure stable islanded operation of LV feeders. Furthermore, a more typical situation is taken into consideration, where the prosumers are single-phase.

Chapter 5 and 6 are about the inertia enhancement by grid-forming prosumers. An advanced controller for ESS's bidirectional DC/DC converters is proposed based on the active disturbance rejection control (ADRC) in Chapter 5. This control method is superior in rejecting the external disturbance, which is suitable for the case of inertia enhancement, as low inertia results from insufficient power compensation during the load change. The behaviour of such an ADRC controller is compared with the standard proportional-integral (PI) controller. Simulation results illustrate the superior performance of the ADRC controller.

Next, in Chapter 6, the inertia support problem is further discussed by using the grid-forming prosumers. The inertial response provided by synchronous generators in conventional power systems is analyzed first, which illustrates that instant power compensation provided by DER can help enhance the system inertia. After that, the inertia support by grid-forming prosumers based on the matching control is proposed. By the matching approach, the frequency regulation problem is translated into the DC voltage control problem, which is realized in the controller in DC-stage converters. Simulation results reveal that grid-forming converters provide a genuine inertial response similar to the synchronous machines, and this inertial response can be enhanced by a higher voltage droop coefficient and a larger number of grid-forming prosumers. Finally, to further enhance the inertial response from the grid-forming prosumers, a nonlinear droop method based on piece-wise power function is proposed. This nonlinear droop controller ensures that a small amount of power is provided by batteries in the steady state while a large amount of power is supplied during the transient state caused by load change, and thus an enhanced inertial response is provided by prosumers, leading to a smaller RoCoF.

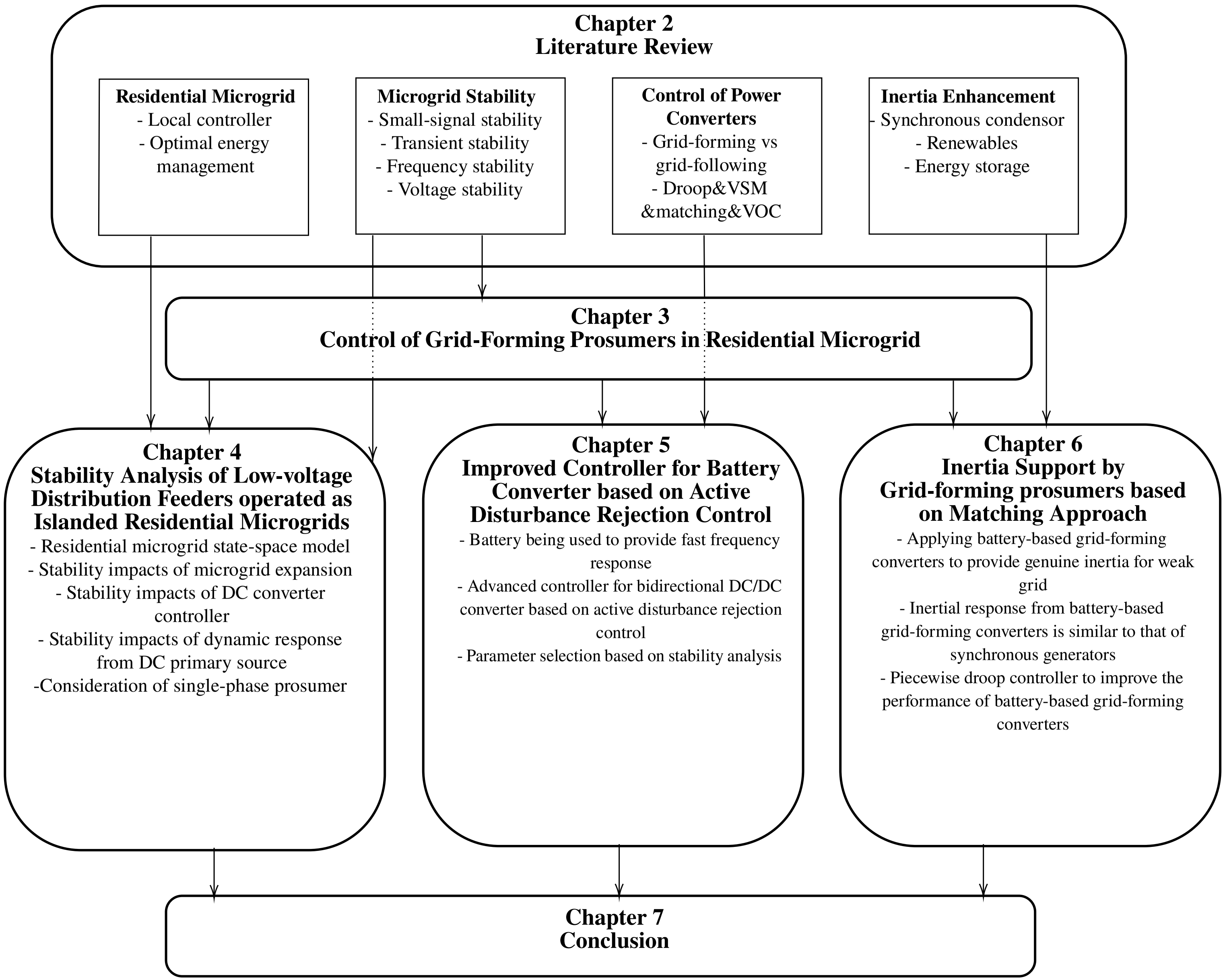

Figure 1.1: Thesis' structure, outlining general contents and contributions, and showing the connection between remaining chapters in this thesis.

Chapter 2

Literature Review

As discussed in Chapter 1, low-voltage (LV) distribution networks can be operated as residential microgrids by making use of the prosumer-owned distributed energy sources (DER) interfaced as voltage sources based on grid-forming control. These grid-forming prosumers not only improve the LV networks' resiliency but also help enhance the system inertia when large numbers of non-rotating renewable generations emerge. This strategy is made possible by the advances in infrastructure aspects, such as the increasing investment in behind-the-meter DER at the residential level, and the methodological aspects, such as the local controllers for power converters.

As such, the literature will start with the techniques in residential microgrids, discussing the existing research focus and methodologies. This is followed by an overview of the control techniques in power converters, mainly focusing on the local controllers at the prosumer level. In particular, the definitions of grid-forming and grid-following are clarified based on the applications in this thesis, as the classification of power converters is diversely defined by different literature.

Next, as the stability of such residential microgrids is one of the concerns in this thesis, an overview of the microgrid stability problems is given, which mainly discusses the case of the islanded operation. The review focuses on the stability issues in microgrids, discussing how the stability is influenced by different factors, and measures taken to enhance the stability. In particular, in the review of the frequency stability, low-inertia problems in modern power systems are emphatically discussed. Existing inertia enhancement strategies are then discussed. Attention is mainly paid to the services provided by DER with the help of their local controllers.

Finally, the literature gaps are discussed, paving the way for the remainder of the thesis to be elaborated.

2.1 Microgrids

A microgrid is defined as an integrated energy system consisting of different types of DER and loads, which can be operated in either grid-connected mode or islanded mode [7]. DER in a microgrid contain renewable energy sources (RES) such as solar PVs, small wind turbines and mini-hydro, as well as energy storage such as fuel cells, batteries and supercapacitors, which are required to be controlled in a proper manner. Microgrids can be found in both low and medium voltage operating ranges, typically from $400\,\mathrm{V}$ to $69\,\mathrm{kV}$ [8]. In the grid-connected mode, the microgrid is coupled with the main electricity network at the point of common coupling (PCC), ensuring the bidirectional power flow between them. In the islanded mode when the microgrid is disconnected from the main grid, the load demand in the system should be supplied by the powers from local generations. Seamless transition from grid-connected to islanded mode should be guaranteed.

Different from traditional power systems, the main generation sources are highly distributed in microgrids. These distributed generations (DGs) are interfaced with the system either directly (such as diesel generators) or by power converters (such as PV and energy storage units). In this context, the behaviour and characteristics of microgrids are much different from conventional power grids, which poses new challenges on the control, operation and protection.

Briefly, several main aspects of microgrid characteristics can be summarized as follows:

- Low system inertia. Unlike conventional generator-driven power systems whose inertia is provided by the kinetic energy stored in synchronous generators, most inverter-interfaced DGs in microgrids have no physical inertia.

- Larger time frame. Power converter-based DGs feature a faster response than synchronous generators. The transient response of the microgrid is composed of multiple transients varying from milliseconds (inverter control) to several minutes (generator control).

- DGs proximity to demand. As generations in microgrids are highly distributed, DGs can be located close to the load demand, which arises the requirement for control strategies.

- High R/X ratio. Microgrids are usually applied in LV networks, where the resistance of the transmission feeder is larger than the reactance, resulting in the coupling of voltage and frequency.

A generic microgrid is controlled in a hierarchical configuration. Similar to conventional power systems, a typical microgrid control system is constructed by a three-level configuration, with primary, secondary, and tertiary control [9]. Primary control deals with the power sharing among multiple DGs by adjusting the frequency and magnitude of voltage reference for DGs' local controllers. In particular, for inverter-interfaced DGs, the voltage reference is tracked by the inner controller generating the modulation signals for switching devices. Power droop control is often applied in this level, by which the microgrid frequency and magnitude deviate from the nominal value to adjust to the load change. The deviations are compensated next by secondary control, which works as a centralized automatic generation controller. Errors are processed to all the generation units by the communication system to adjust their power output and thus restore the output voltage frequency and amplitude. Finally, the tertiary control level is used mainly for economical concerns. Power references for all units are generated based on the optimization process, which considers both the supply-demand balance and the marginal generation costs.

2.2 Residential microgrids

A residential microgrid is a particular case of microgrids. A typical residential microgrid is composed of RES, energy storage systems (ESS) and aggregated loads distributed in local households. Prosumers are integrated by a common feeder which shapes like a radial network [10]. Such a network is able to work in both grid-connected and islanded modes. Despite the rich microgrid literature, residential microgrids have so far attracted little attention. Briefly, the key distinction between a *conventional* and a *residential* microgrid is that the latter is supplied exclusively by prosumer-owned DER. Notably, residential customers typically use single-phase connections [5, 10–12]. According to [11], a three-phase residential microgrid can typically consist of three separate single-phase systems. With a sufficient number of DER, various prosumers located on a single-phase line can form a microgrid that could operate in islanded mode. A benchmark residential microgrid was given in [10] and [11] with considering the single-phase connection situation of household prosumers. The primary feeder is stretched from the substation and then separated by three single-phase secondary feeders. All prosumers are assumed to own rooftop PV systems and storage installed in their houses. Back-to-back converters are used to connect separate phases, allowing the intra-phase power exchange. This scenario can serve as a typical structure of modern residential microgrids which are exclusively supplied by DER.

Existing works on residential microgrids mainly focus on the design of the local controllers of power converters [10, 11, 13–15], and the optimal local energy management within the residential microgrid [5, 16–18].

2.2.1 Local controller of power converters

An important focus of residential microgrids is the local controllers for the power converters of prosumers. As residential microgrids can be a combination of single-phase and three-phase generations, the power flow among various generations is vital for the appropriate operation of the network, including the power exchange within each phase, among the three phases, and between the three-phase generations and the single-phase network. The intra- and inter-phase balance management were studied in [10, 11, 13]. Typically, the power exchange between different phases is ensured by back-to-back converters with dual full-bridge rectifiers. Authors in [13] proposed a controller for the back-to-back converter for the intra-phase power management based on the change of the DC-link voltage. The study case contains both single-phase prosumers and three-phase generation sources, while [10, 11] studied the case with single-phase prosumers only. The management strategy is based on a multi-segment power droop control, which sets the droop gains according to different frequency ranges. Intra-phase power exchange is controlled via back-to-back converters as in [13], and it only takes place when the power balance in one phase cannot be maintained locally.

In comparison, [14, 15] studied the issue of power quality and seamless mode transition of the residential microgrid. Authors in [15] adopted distributed incremental adaptive filter to enhance the power quality. Furthermore, the state of charge (SOC) is taken into consideration when designing the controller. The study case is only based on one prosumer with a PV-battery hybrid system. Active powers absorbed by respective residents are controlled with constant reference in [14] to avoid the influence from the load uncertainty. However, the system voltage reference in islanded operation is provided by a dedicated unit with lots of PVs and a large battery. Residential prosumers, comparatively, are integrated by grid-following converters.

2.2.2 Local energy management

As introduced in Chapter 1, LV feeders with grid-forming prosumers can operate as islanded residential microgrids after separation from the main grid. Once the separation happens and the islanded system stably transitions to islanded operation, the next step is to manage the power flow of the whole microgrid by prosumer energy management systems (EMS). The EMS not only maintains the power balance between generations and loads but also optimizes the powers from each prosumer to maximize the use of DER. The coordination between prosumers can be done using a central controller or in a fully decentralised fashion [19].

Optimal energy management should consider the inherent behaviour of the DER as constraints, for example, the SOC of batteries and the instant power that can be provided by DER [20]. Authors in [5] considered the batteries' SOC limitation as optimization constraints to design a cooperative energy management system among household prosumers, and [21] proposed a detailed battery lifetime estimation model to minimize the energy cost as well as meeting the requirement of total loss of the power supply. Many existing works focus on the optimal energy management on the level of central controller with the aim of minimizing the economic cost [5, 16–18]. Among these, [16, 17] are based on the fuzzy logic, while [5, 17] focuses on the influence from the demand response.

2.3 Control of power converters

Power converters are the key actuators to interface the DC primary sources of prosumers with the AC grid. Based on power electronic devices, these actuators are responsible for providing multiple services for the grid, such as delivering active and reactive power, providing fast frequency response, load sharing, voltage regulation, and so forth.

2.3.1 Classification

Classification of power converters is reported in [22], in which power converters are classified into "grid-forming", "grid-feeding" and "grid-supporting" converters. Under the definition in this paper, a grid-forming converter is controlled to work as an ideal AC voltage source with a given voltage reference (amplitude and frequency). This voltage reference is set as a constant, as shown in Fig. 2.1 (a). ω^* and v^*_{mag} are the frequency and magnitude references of the output voltage. Due to the inherent voltage-source feature, such converters can operate in the islanded mode by supplying loads

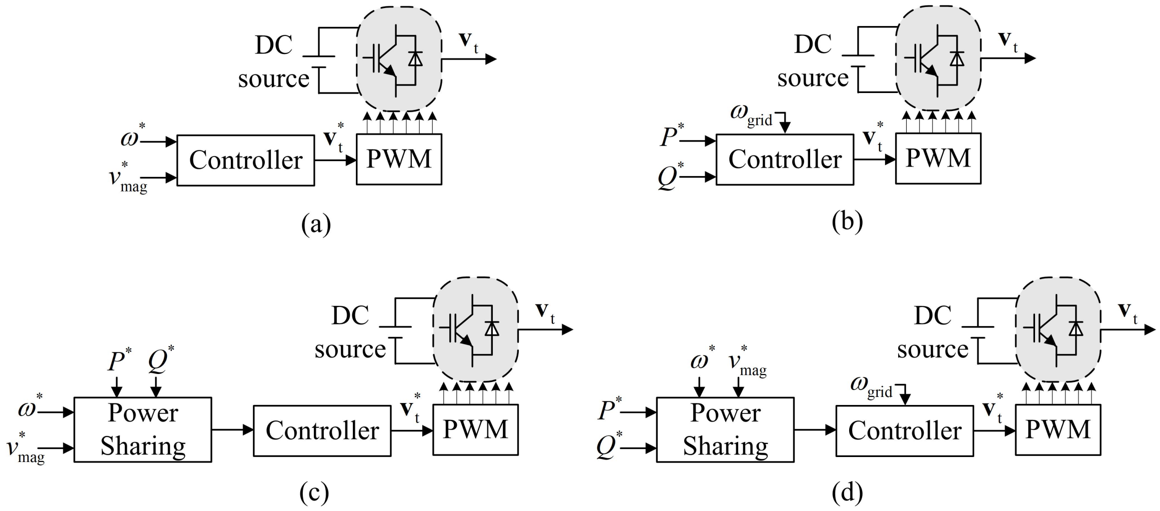

Figure 2.1: Simplified representation of grid-connected converters.

in a standalone system. The grid-forming control structure is often implemented into the dedicated equipment which provides the voltage reference for the rest synchronized generations.

In comparison, a grid-feeding converter is like a controlled current source, as shown in Fig. 2.1 (b). These converters are controlled to deliver the desired amount of active and reactive powers P^* and Q^*, as well as participating in the control of grid voltage and frequency. A synchronization unit such as a phase-locked loop (PLL) should be applied to ensure the grid-feeder converters stay synchronized with the grid. These power converters are suitable to operate in parallel with other grid-feeding power converters. However, they can never operate without the grid or a grid-forming generation that sets the voltage reference.

Fig. 2.1 (c) and (d) show typical configurations of two types of grid-supporting converters, The converter in Fig. 2.1 (c) works as a voltage source, while the one in Fig. 2.1 (d) works as a controlled current source. The working principle of these two converters is similar to that of grid-forming converters and grid-feeding converters as shown in Fig. 2.1 (a) and (b), respectively. The difference is that such converters exhibit power sharing with other generations. Both grid-supporting converters can operate in parallel with other converters, while only the voltage-sourced grid-supporting converter (Fig. 2.1 (c)) can work in the islanded mode.

2.3.2 Declaration

According to the classification in Section 2.2.1, it is clear that power converters are interfaced with the grid in two main types: voltage sources (grid-forming and voltage-source-like grid-supporting) and controlled current sources (grid-feeding and current-source-like grid-supporting). In this thesis, as a simplification, the categories of power converters can be summarized by two main definitions. Converters who behave like voltage sources are referred to as “grid-forming” converters, while converters who behave like controlled current sources, on the other hand, are referred to as “grid-following” converters, as defined in [1, 23, 24]. The voltage reference in grid-forming converters can be set either as a constant or based on power sharing methods, which enables the parallel connection of

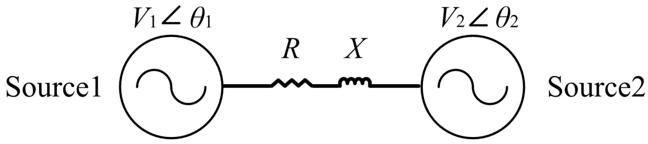

Figure 2.2: Two-source transmission system

multiple converters.

2.3.3 Grid-forming control

Compared with grid-following control, the main difference of the grid-forming control is the independence of the frequency measurement unit. The voltage reference, especially the frequency reference, is determined by the controller of its own, which avoids the time delay resulted from the frequency measurement unit such as a PLL. Paralleled grid-forming converters should exhibit proper load sharing with or without dedicated communication lines. It is expected that grid-forming converters will serve as a cornerstone of future power systems, which support load sharing, frequency response, and system strength enhancement [1].

The main idea of grid-forming control is to mimic the characteristics of conventional synchronous machines. Based on different focuses, many grid-forming methods have been reported, which can be generally categorized as droop control, virtual synchronous machines, matching control and virtual oscillator control [1, 23].

Droop control

Droop control is widely used as a baseline solution for grid-connected power converters. This idea comes from the inherent droop property of the generators, by adjusting the active and reactive power output according to the change of frequency and magnitude of the grid voltage. By considering a simple power transmission system shown in Fig. 2.2. Two sources 1 and 2 are connected by a transmission line. The active and reactive powers that are delivered from Source 1 to Source 2 can be expressed by

$$P_1 = \frac{V_1}{R^2 + X^2}[R(V_1 - V_2\cos\theta_{12}) + XV_2\sin\theta_{12}], \tag{2.1a}$$

$$Q_1 = \frac{V_1}{R^2 + X^2}[-RV_2\sin\theta_{12} + X(V_1 - V_2\cos\theta_{12})], \tag{2.1b}$$

where P_1 and Q_1 are active and reactive powers from Source 1. V_1 and V_2 are voltage values at Source 1 and Source 2. θ_{12} corresponds to the phase-angle difference between the two voltages, and R and X are the transmission line resistance and reactance, respectively [22].

In an inductive grid such as a high-voltage and medium-voltage network, R is negligible compared to X. Assuming $\sin\theta_{12} \approx \theta_{12}$ and $\cos\theta_{12} \approx 1$, (2.1) can be rewritten as

$$P_1 \approx \frac{V_1}{X}V_2\theta_{12}, \tag{2.2a}$$

$$Q_1 \approx \frac{V_1}{X}(V_1 - V_2), \tag{2.2b}$$

which shows a direct relationship between the power angle θ_{12} and the active power P_1, as well as between the voltage difference $V_1 - V_2$ and the reactive power Q_1. Therefore, the grid frequency and voltage can be regulated by controlling the values of powers for each individual generation in the form of

$$f^* - f = -m_{\mathrm{P}}(P^* - P), \tag{2.3a}$$

$$V^* - V = -n_{\mathrm{Q}}(Q^* - Q), \tag{2.3b}$$

where superscript $*$ denotes the reference values for the regulated variables.

Droop controls for power converters have been widely adopted to achieve power sharing between multiple converters either in the grid-connected or the islanded mode without communication lines. However, some issues associated with conventional droop control such as the frequency deviations, power-sharing errors, and stability concerns cannot be simply solved by adjusting the droop gains. This provides the motivation for the study on improved droop controllers. Supplementary droop characteristics were applied in [25–28]. A derivative term of power was added to the droop controller to improve the transient response of the microgrid with paralleled inverters, including large load variation and microgrid isolation. Relevant derivative parameters are calculated based on the optimization algorithm in [26]. Authors in [25] modified the active power droop as a proportional-integral-derivative (PID) block to reduce the circulating current during the transient state. In addition, in a microgrid case where several DGs are connected to a single feeder with series connections, a droop approach with the algorithm-based feeder flow control is proposed in [29] to regulate the significant frequency change by excessive loading during the transition from grid-connected to islanded operation. Economic problems relevant to active power sharing should also be considered in the design of droop controller. A nonlinear scheme based on generation cost of the microgrid is proposed in [30], and a linear cost-prioritized droop scheme presented in [31] achieved optimal active power sharing and minimized generation cost.

Despite the wide application of conventional droop control, P/f and Q/V relations are impacted by the existence of transmission line resistance R as illustrated in (2.1). In a LV network where R cannot be neglected, the conventional droop method should be modified to adjust to the relatively high R/X ratio.

A modified droop method by using P/V and Q/f droop in resistive networks is proposed in [32–34]. By neglecting X in (2.1), the droop relations between P and V as well as Q and f are detected. To solve the problems like line impedance dependency, inaccurate active power or reactive power regulation and slow transient response, improved P/V and Q/f droop is proposed in [34–36]. Authors in [36] supplemented the P/V droop with a proportional-integral (PI) power compensator. [35] proposed the voltage-power droop/frequency-reactive power boost (VPD/FQB) control scheme with considering the resistive network character. Multiple converters contribute to the regulation of the microgrid voltage and frequency, allowing the operation in both islanded and grid-connected modes. As a general case, the combined effect of the resistive and inductive line impedance components are taken into account in the droop control equations in [22, 34, 37]. The frequency and voltage droops are determined by both active and reactive powers.

Instead of applying modified droop approaches, the conventional droop can be improved with the impedance value being modified. As the mismatch of P/f and Q/V droops in LV networks is resulted by the large R/X ratio, a large inductor can be added between the power converter and the network. This method equivalently increases the inductance in the network and thus modifying the line impedance. The disadvantage is that introducing an inductor increases the voltage drop, reducing the overall efficiency. The implementation of the virtual impedance can solve this issue [38–40]. The virtual impedance modifies the power converter output voltage reference as

$$\boldsymbol{v}_{\mathrm{ref}} = \boldsymbol{v}^{*}_{\mathrm{ref}} - Z_{\mathrm{v}}\boldsymbol{i}_{\mathrm{abc}}, \tag{2.4}$$

where Z_{v} is the dynamic virtual impedance and $\boldsymbol{i}_{\mathrm{abc}}$ are the converter output currents. Improved virtual impedance has been reported in [36, 41–43], including the adaptive virtual impedance for the sake of reducing the harmonics [36, 42, 43], and the frequency-coordinated virtual impedance by considering the various dynamic response from different DGs [41].

Virtual synchronous machine

The underlying idea behind the virtual synchronous machine (VSM) concept is to emulate the essential behaviour of a real synchronous machine (SM) by controlling a power electronic converter [23]. Basically, VSM implementation contains more or less explicitly a mathematical model of a SM instead of only emulating the droop characteristics. The most common SM model that is applied by the VSM is the swing equation

$$J\frac{d\omega_{\mathrm{r}}}{dt} = T_{\mathrm{m}} - T_{\mathrm{e}} - D_{\mathrm{m}}\omega_{\mathrm{r}}, \tag{2.5}$$

where J, D_{m}, T_{m}, and T_{e} are the moment of inertia constant, damping coefficient, mechanical torque, and electromagnetic torque of the generator, respectively. The emulation of the inertial characteristic and damping of the electromechanical oscillations are common features for every VSM implementation.

A VSM algorithm is the primary part of the system which are interfaced like synchronous machines [44]. Several VSM topologies have been proposed based on different VSM algorithms [45–48]. The first proposal of a VSM was referred to as “VISMA” [45]. After that, an ISE topology was proposed in [46]. The frequency and voltage are measured at the PCC. A KHI topology was developed then [44]. An automatic voltage regulator and a governor unit are applied to generate the voltage reference of the virtual machine, after which the current reference for a synchronous generator is generated according to algebraic phasor representation. The common feature of these topologies is that the grid frequency is measured in the algorithm to mimic the SM’s behaviour. In comparison, a topology without frequency measurement named synchronverter is proposed in [48–50]. Similar to the synchronous generator output power regulation, the output power of the inverter is regulated by frequency droop and the emulated swing equation. Moreover, the damping factor and moment of inertia can be adjusted to cater for different operation conditions. Synchronverters behave like voltage sources as the inverter output voltage reference is computed without measuring the grid frequency.

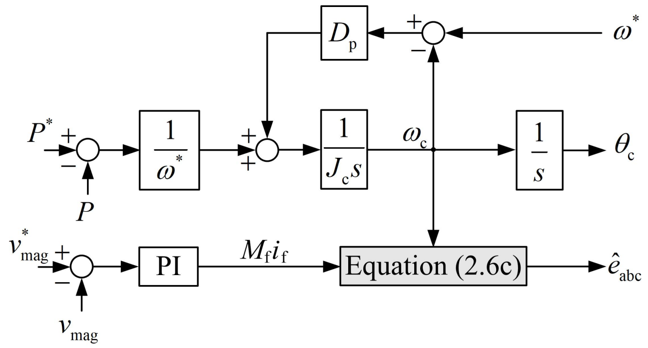

Figure 2.3: Basic diagram of virtual synchronous machine [1].

The basic control principle of a synchronverter can be represented by

$$\dot{\theta}_c = \omega_c, \tag{2.6a}$$

$$J_c \ddot{\theta}_c = \frac{1}{\omega^*}(P^* - P) + D_p(\omega^* - \omega_c), \tag{2.6b}$$

$$\hat{e}_{abc} = 2\omega_c M_f i_f \dot{\theta}_c \widetilde{\sin}\theta_c, \tag{2.6c}$$

where θ_c and ω_c are the emulated rotor angle and frequency of the converter, respectively. J_c and D_p are the virtual inertia and damping coefficient, respectively. $\hat{e}_{abc}$ is the emulated electromagnetic force (output terminal voltage) of the converter. M_f is the mutual inductance amplitude, and i_f is the excitation current. $\widetilde{\sin}\theta_c = \begin{bmatrix}\sin\theta_c & \sin(\theta_c - \frac{2\pi}{3}) & \sin(\theta_c + \frac{2\pi}{3})\end{bmatrix}^\top$. A basic control diagram is shown in Fig 2.3. With the emulation of the inertia and damping coefficient of synchronous generators, VSMs are widely applied in the frequency control of highly renewable-penetrated microgrid, providing system inertia and damping to improve the dynamic frequency response [51–54]. Proper reactive power sharing is studied in [55–57], considering the effect of the line impedance and load fluctuation. The issue of unbalanced and distorted grid connection can also be improved by the application of VSM [58–60].

Matching control

Matching control is based on the idea of mimicking the behaviour of synchronous generators (SG). This control approach is proposed on the basis of the structural similarities between SG and two-level power converters [24, 61–64]. The core part of matching control is to link the converter DC-link voltage v_{dc} and SG rotor angular frequency ω_r with a constant factor η. Hence, the energy stored in the DC-link capacitor is linked with the kinetic energy in the rotor consequently. Matching control makes it possible to regulate the frequency by simply controlling the DC-link voltage.

Take the example of an averaged 3-phase converter model shown in Fig. 2.4 [65]. The AC variables are represented in the stationary αβ0 frame. The similarity between the two-level converter model and the generator model can be illustrated as follows [61].

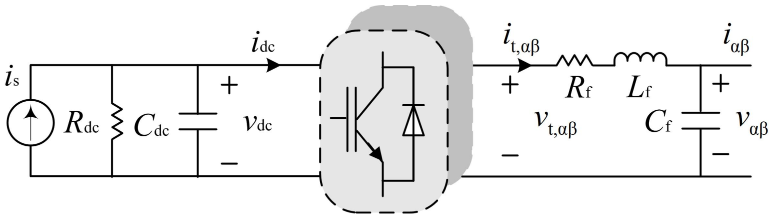

Figure 2.4: A two level converter.

Converter model:

$$C_{dc}\dot{v}_{dc} = i_s - \frac{1}{R_{dc}}v_{dc} - i_{dc}, \tag{2.7a}$$

$$L_f\dot{\boldsymbol{i}}_{t,\alpha\beta} = \boldsymbol{v}_{t,\alpha\beta} - R_f\boldsymbol{i}_{t,\alpha\beta} - \boldsymbol{v}_{\alpha\beta}, \tag{2.7b}$$

Generator model:

$$J\dot{\omega}_r = T_m - T_e - D_m\omega_r, \tag{2.8a}$$

$$\dot{\boldsymbol{\psi}}_{s,dq} = \boldsymbol{v}_{s,dq} - R_s\boldsymbol{i}_{s,dq} - \begin{bmatrix} 0 & -1 \\ 1 & 0 \end{bmatrix}\boldsymbol{\psi}_{s,dq}, \tag{2.8b}$$

where $\boldsymbol{\psi}_{s,dq}$, $\boldsymbol{v}_{s,dq}$ and $\boldsymbol{i}_{s,dq}$ denote the stator winding flux, voltage, and current in dq0-coordinates (See [66], Fig. 3.1), respectively. By observing the similarity between (2.7) and (2.8), it is clear that the equivalence of the two models can be achieved by the controller as

$$\boldsymbol{m}_{\alpha\beta} = \mu \begin{bmatrix} -\sin\theta_c \\ \cos\theta_c \end{bmatrix}, \tag{2.9a}$$

$$\dot{\theta}_c = \eta v_{dc}, \tag{2.9b}$$

where θ_c is the angle for the DC-AC converter output (the same as the emulated rotor angle in VSM), and $\mu \in [0, 1]$ represents an amplitude for the modulation signal. In this case, the control approach can be applied by following

$$\omega_c = \eta v_{dc}, \tag{2.10}$$

where $\eta = \omega^*/v_{dc}^*$ encodes the ratio between the nominal grid frequency and the DC voltage reference. Based on this method, the frequency shift in the grid is translated into the DC-link voltage change. This can be explained by observing the power balance immediately after a disturbance. A power change in the grid is initially compensated by the energy stored in the DC-link capacitor, similar to the inertial response coming from the kinetic energy stored in the rotating mass of a synchronous machine. Hence the voltage regulation basically applies an i_s/v_{dc} droop control, which mimics the conventional P/ω droop characteristic, and the DC current reference is determined by the sum of the droop controller output and the power injection feed-forward to adjust the power output [1]. The basic diagram of the matching control approach is shown in Fig. 2.5.

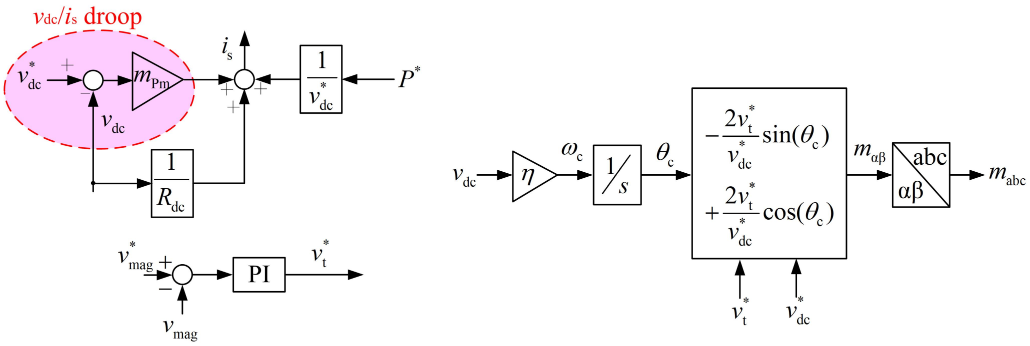

Figure 2.5: Basic diagram of matching approach.

Detailed modelling process and experimental verification are discussed in [62–64]. Compared with the conventional droop method and the VSM technology, matching control builds a direct relation between the DC-link voltage and the frequency. Consequently, the frequency regulation problem is translated into the DC voltage control problem, which is realized in the design of the DC-voltage controller. [67] applied matching control into the battery-based inverter to provide inertia for the system, as well as contributing to the frequency control. It is concluded in [1] that matching control is relatively robust to the DC source limitation due to the fact that frequency regulation is based on the DC-side voltage. [68] proposed a matching-based electronic synchronous machine with a detailed design process of the matching controller. The paper considers cases for the sake of both the synchronization to a stiff grid and the regulation of a weak grid, which offers comprehensive guidance on the implementation of the matching approach.

Virtual oscillator

Virtual oscillator (VOC) is a novel grid-forming control strategy. Unlike the grid-forming methods explained above, VOC is not directly inspired by synchronous machines [23]. Instead, this strategy is based on synchronization theory and nonlinear control methods.

Basically, due to the AC dynamics of power converters, the inverter-based power network can be regarded as a connected undirected graph where inverters serve as coupled oscillators. Synchronization of inverters in islanded operation is translated into the problem of synchronization and coordination of coupled systems with limited or no communication. This concept was first adopted in [69, 70] with the application of droop control and modified Kuramoto model in the coupled oscillators. However, the voltage dynamics of inverters was not considered. Controlling inverters as virtual Liénard-type oscillators provides promising solutions as VOC is able to globally synchronize an inverter-based power system. Based on that, dispatchable VOC was developed in [71] considering the network dynamics. The droop characteristic in dispatchable VOC can be revealed as

$$\dot{\theta}_c = \omega^* + m_{voc}\left(\frac{P^*}{v^{*2}_{mag}} - \frac{P}{v^2_{mag}}\right), \tag{2.11a}$$

$$\dot{v}_{mag} = m_{voc}\left(\frac{Q^*}{v^{*2}_{mag}} - \frac{Q}{v^2_{mag}}\right)v_{mag} + \frac{n_{voc}}{v^{*2}_{mag}}\left(v^{*2}_{mag} - v^2_{mag}\right)v_{mag}, \tag{2.11b}$$

where m_{voc} and n_{voc} are the positive control gains.

2.4 Microgrid stability

Stability is defined as the ability of a system to recover to a new steady state after being subjected to a disturbance [72]. It is one of the most important concerns in the operation of power systems. Due to the microgrid unique intrinsic features and systemic differences, the stable operation of microgrids is more challenging than that in conventional power systems. According to the physical phenomenon of instability, traditional power system stability problems are classified into three categories: rotor angle stability, voltage stability, and frequency stability, focusing on different parts of the power system [73].

- Rotor angle stability is caused by the power angle of a generator, which is defined as the angle between the electromagnetic force and the terminal voltage. It represents the ability that generators remain in synchronism after being subjected to a disturbance, which is essentially the balance between the electromagnetic torque of the generator rotor and mechanical torque. The rotor angle stability is classified as small-disturbance angle stability and large-disturbance transient stability.

- Voltage stability refers to the ability that the power system maintains steady voltage on all buses after subjecting to disturbances. Voltage instability is mainly caused by long transmission lines, which limit the power transfer between generations and loads. The voltage stability applies to both short-term and long-term stability issues, and they are also subject to small disturbances and large disturbances in the system.

- Frequency stability refers to the ability that the power system can maintain the steady frequency under a variety of conditions. It essentially indicates the power balance in the whole power system, which can be either short term or long term.

According to the definition, conventional power system stability issues are dominantly addressed by the control and coordination of synchronous generators.

In the microgrid, however, power generation units are constructed by a wide variety of equipment and technologies, including a large number of inverter-based RES and ESS. These generation sources have no physical inertia, which results in considerably lower inertia in the microgrid, jeopardizing the frequency stability significantly. As stability is highly related to demand-supply power balance, high penetration of variable and intermittent RES probably influences the stability negatively. In addition, as microgrids are relatively smaller in size, the short circuit capacity is relatively lower, especially in islanded microgrids. Such a system may experience large voltage and frequency deviations even with small disturbances. Furthermore, voltage and frequency in microgrids are highly correlated due to the higher R/X ratio in the network, changing the relationships between voltages, frequencies, and power flows. The aforementioned aspects in microgrids make the stability issues in such a system more complicated [74].

In this context, studies on microgrid stability are carried out mainly focused on factors that pose risk on stability, mathematical modelling of microgrids, assessment methods, and stability improvement methods for microgrids. According to the causes of stability issues, microgrid stability can be categorized as small-signal stability, transient stability, frequency stability and voltage stability. Based on the operation mode, these stability issues can be further classified by grid-connected stability and islanded stability, focusing on different targets in the microgrid [75].

2.4.1 Small-signal stability

Small-signal stability corresponds to the system subjected to small disturbances such as the connection or disconnection of a single load or generator. It is analyzed with a linearised state-space model combining the micro sources, network dynamics and loads. A disturbance is considered small if a linearised set of equations can adequately represent the system behaviour [73, 76, 77]. Eigenvalues of the state matrix derived from the linearised model determine the small-signal stability of the system. To assure stability, the real part of characteristic roots must be negative. A satisfactory damping margin is also expected when focusing on the position of complex eigenvalues, ensuring less oscillation during transient response.

Linerised modelling of microgrid

Studies on the suitable modelling of microgrids are many. In particular, much attention is paid to the modelling process of inverter-dominated microgrids. As a large number of state variables are involved in the linearised model, the analysis of microgrid will be computationally more demanding. Hence, some papers proposed reduced-order microgrid models to decrease the complexity. In [78], the microgrid model was built without considering the effect of microgrid high-frequency models. The paper focuses on the electro-mechanical transient of the system. Moreover, [79] neglected both the inner controllers and the output filters in the model. The simplification is effective in some cases. However, in systems highly penetrated by inverter-based generations, controllers play an important role in small-signal stability, and thus should be modelled in detail.

In this context, small-signal stability analysis was proposed in [80] with regards to a system with two paralleled inverters. Based on the proposed model, optimal droop gains and the cutoff frequency of the filter can be chosen appropriately. However, this work neglected the model of the inner voltage/current regulators, which ensure the inverters track the voltage reference accurately. Parameters relevant to the inner controllers determine the accuracy of the microgrid model and thus should be considered. As a result, a systematic modelling approach for an autonomous microgrid was proposed in [81], which combined dynamic models of individual inverters, the network and loads with constant impedance. The proposed model is a general model which can be applied by any number of inverters. Moreover, inverters were first modelled in their individual reference frames and then transformed into a common reference frame in the network. In particular, the DC input was simplified as a constant DC voltage source. Nevertheless, the simplification of the DC link cannot be applied to all cases as DC side dynamics is dependant on the DC-side configuration.

Based on the modelling concept in [81], authors in [82] included the DC dynamics in the small-signal model. The DC side and AC side are linked by the active power balance. However, the DC-side source was represented by a large capacitor. Only the dynamics of this capacitor was taken into consideration. [83] improved the microgrid model by including the model of the DC converter between the DC source and the inverter. The double-looped DC voltage controller was also included in the linearised model. The dynamic response from various primary DC sources were studied by introducing a first-order system in [84]. Such model was applied in [85] with further studying the DC-side current limitation on system stability.

Linearised models mentioned above are all based on the dq0-coordinate system, in which AC variables are transformed into the rotating dq0 reference frame by Park transformation. Variables in the dq0 frame are DC with constant steady-state operating values, thus enabling the microgrid model to be linearised around the equilibrium points. In addition to this method, microgrid modelling can also be conducted with phasor-based methods [86] and harmonic linearisation [87–89].

Stability analysis tools

Commonly, there are two major analysis tools used for small-signal analysis: the state-space method and the impedance-based method [90]. The state-space method uses the system's state-space model for analysis. It is comprehensive with detailed consideration of the system topology and control parameters of individual inverters. Undamped and unstable modes can be investigated by analysing the state matrix. The issue is that the state-space method requires the extensive knowledge of the system and control parameters, which are sometimes not fully accessible. The impedance-based method, on the other side, can be easier to formulate ad validate. The idea behind this method is that all components in the system are modelled by their Thevenin or Norton equivalent circuits. Stability can be investigated by seeing if the impedance ratio satisfies the Nyquist stability criteria. This method is very useful for analysing high-frequency dynamics and the impact of interactions between a certain inverter and the grid. A disadvantage is the limited observability of certain states [91].

Due to their certain advantages and disadvantages, these two methods can often be used in a complementary manner. In Chapter 4 where the stability of LV feeders is discussed, the state-space method is applied to investigate the reasons for certain unstable modes.

Stability impacts

Based on linearised models, the small-signal stability of a microgrid can be investigated. Studies of stability impacts are mainly focused on feedback controllers, the types of loads and the network R/X ratio. Small-signal stability is highly related to the parameters in the feedback controllers, and specifically, the droop gains. The impact of droop gains on the microgrid stability was investigated in [7, 27, 75, 81, 92–97], Studies show that a large droop gain may result in the low-frequency dominant eigenvalues approaching the right-hand side of the complex plane, indicating the instability.

In terms of the load model, [81, 82, 95] considered the loads with constant impedance, whilst microgrids are often penetrated by some non-linear loads such as rectifier-inverter-fed induction motors (IMs). The nonlinear dynamics challenges the stability, resulting in rather unrealistically large stability operating region [98]. The impact from the IM loads was investigated in [93, 98–100]. In particular, [100] detailed the modeling procedure by a composite load model with a static load and an IM. Though the composite load model is not strictly necessary for oscillatory behavior accuracy, it is important when the load margin must be assessed. Similarly, by combining the static and dynamic loads, the relationship between the low frequency instability and motor dynamics was discussed in [101].

Another impact comes from the high R/X ratio of the microgrid network, which results from the predominantly resistive LV power lines. The investigation of the R/X ratio on microgrid small-signal stability was carried out in [33, 92, 102]. Studies show that when the power controller applying conventional P/f and Q/V droop control, a smaller R/X ratio helps push the system to a more stable region. However, when the reverse droop by P/V and Q/f is applied, the system tends to be unstable when R/X ratio is small.

Stability improvement

According to the stability impacts, the droop controller is one of the most important causes of the microgrid small-signal instability. As a result, methodologies of stability improvement are mainly focused on the modified droop controllers. [25, 95, 103] worked on the supplementary loops. An adaptive droop control with additional derivative terms of power was proposed in [25]. The addition of derivative terms improves the transient response without influencing the steady-state behavior. [95] supplemented the droop controller by the change of the d-axis voltage reference. The approach pushes the dominant poles further from the unstable region, which ensures a high droop gain is used for proper load sharing, especially in weak grids. The supplementary terms in [103] are based on the total real and reactive power generations in the whole system.

In addition, some papers modified the droop controller with new characteristics. [102, 104] designed the droop controller by an Arctan droop curve, by which the droop slope is determined by the algorithm based on arctan functions. The stability margin is largely improved with the proposed method. [105] proposed an adaptive feedforward compensation that alters the dynamic coupling between a distributed-resource unit and the host microgrid. The feedforward compensation is modified periodically according to the system steady-state operating point. The proposed method enhanced the robustness of the system stability to droop coefficients and network dynamic uncertainties. [106] designed the power controller with both the frequency and amplitude of the voltage determined by both the active and reactive powers. In [107], a gain-scheduled decoupling control strategy was proposed which reshapes the characteristics of the conventional droop controller with additional control signals. The control signals are based on the local power measurement and supplementary dq voltage references. The transient response is improved as the microgrid dynamics is decoupled with the droop gains.

2.4.2 Transient stability

Transient stability refers to the rotor angle stability caused by large disturbances such as grid-connected/islanding transitions, large load steps, loss of multiple distributed generations, and electrical faults. Unlike the analysis of small-signal stability issues, a linearised set of equations cannot adequately represent the system behaviour when the system exhibits large perturbations. The assessment of transient stability issues can be performed by using Lyapunov-based non-linear models, time-domain simulations, and hardware-in-the-loop (HIL) approaches [75].

Studies on the transient stability of microgrid are mainly about the impacts from the DG penetration level, the types of DG, locations of faults and islanded microgrid transient stability.

Penetration level of DG

The percentage of DG penetration is a critical issue for the microgrid transient stability. Various types of DGs exist in the microgrid, posing different impacts on the microgrid according to the penetration level. Authors in [108] studied the impact of distributed synchronous generators on the transient stability of real distribution network. The disturbance results from the islanding of the microgrid. DG with smaller inertia tend to lose their synchronism more easily. A microgrid with high penetration of wind turbines was studied in [109]. Simulation results show that increasing wind penetration tends to reduce the damping of the system. The impact of high penetration level of power converters was investigated in [110], showing that the maximum rotor speed deviation is increased with increasing interface of converters due to the low inertia. The penetration of ESS is proved to have positive impact on the microgrid frequency response, as these ESS help smooth the active power variation [111]. As a result, the transient stability can be enhanced by the penetration of ESS.

Types of generation sources

Various types of generations exist in microgrids which are conceptually and physically different from synchronous generators. The influence of the penetration of asynchronous generators in microgrids was studied in [112]. It was shown that asynchronous generators increase the rotor speed damping of the main synchronous generators considerably. Also, they have a negative impact on the steady-state voltages in the power system. Systems with wind powers are commonly based on doubly-fed induction generators (DFIGs). System faults and dynamic loads pose impacts on the behaviour of DFIGs significantly [74]. The impacts of PV systems on microgrid stability have been widely studied. The operating characteristics of residential PV systems under various transient disturbances were tested in [113]. Based on the testing results, proper measures to meet fault ride-through requirements can be investigated. Stability analysis of distributed solar units and centralized solar farms were presented in [114], which shows that the distributed solar PV generators contribute more to the microgrid stability than solar farms. As a commonly-used energy storage, dynamics models of fuel cells were proposed in [115, 116]. The transient behaviour of fuel cells with their interfaced inverters was thus investigated in [117], showing that fuel cells help improve the microgrid transient stability when power and voltage controllers are implemented.

Loads, faults, and clearing time

The transient stability of microgrids is also related to the conditions of loads and system faults. Similar to the small-signal stability analysis, the non-linear load with IM is the main source of impact from load characteristics, which was investigated in [109, 118]. These works also investigated the location of faults, showing that faults that are initiated in areas with high DG penetration have significant impacts on the transient stability. Due to DG proximity to the loads, a suitable design of the DG placement can improve the transient stability of the transmission systems. In addition, fault clearing time is crucial for microgrids' stable operation, which challenges the ride-through capability of the system. Authors in [119] studied such impact by calculating the critical clearing time for all generators. showing that DG may lose its stability if the faults are not cleared within a specific period.

Stability improvement

Transient stability can be improved by suitable control strategies [120, 121], sizing and siting of DG [114, 122, 123], the use of energy storage [111, 124], and load shedding [125, 126].

In [120], a novel inverter controller by applying virtual inertia in the power loop was proposed to improve the frequency response of microgrids under disturbances involving large frequency deviations. The control strategy proposed in [121] modified the voltage control loop and the frequency measurement in the controllers for electronically coupled DER. The control strategy improves the performance of the host microgrid under network faults and transient disturbances.

As analyzed previously, the transient stability of microgrids is also affected by the sizing of the DG, as well as their locations in the distribution system. Therefore, optimal placement of DG helps improve the stability margin. In [122], the authors detected the critical buses based on mixed-integer nonlinear programming. Buses that are sensitive to voltage profile are put in priority and thus the voltage stability margin is highly improved. A novel stability index considering stable node voltages was presented in [123], while [114] investigated the impact of solar PV generators with different sizes and locations.

Islanded microgrids tend to experience large frequency deviations when a large disturbance occurs. The installation of energy storage systems can help balance the disturbance if their capacity is enough, as ESS are capable of smoothing the power response flexibly. [111, 124] applied ESS to enhance the microgrid stability, A battery-ultracapacitor system was used in [111] while [124] applied the ESS with a fuel cell and ultracapacitor hybrid system.

Even though ESS can compensate the large disturbance, a large inrush current during the transient state might threaten the performance of these ESS. This issue can be solved by proper load shedding. In [125], the authors applied the local meteorological data into a Markov two-state model to determine the shed load. In [126], the power line network was used as a propagation and communication medium, predicting the electromagnetic interference generated by all household devices and thus determining the load shedding strategy.

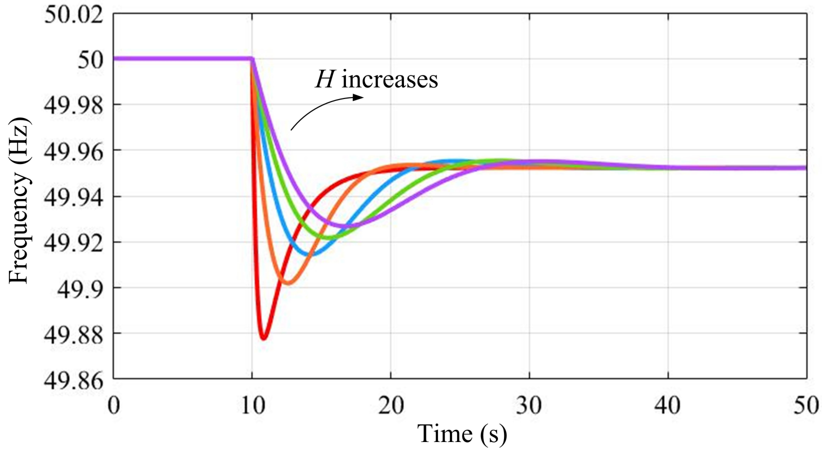

Figure 2.6: Frequency response of a generator under step-up load change (H = 1, 3, 5, 7 and 10).

2.4.3 Frequency stability

Frequency stability is caused by power imbalance between generation and demand in a power system. It is associated with inadequate power supplies and poor coordination between controllers and protection systems. When large demand changes apply while efforts by primary controllers cannot entirely compensate the load change, the system frequency will continuously drop, resulting in the disconnection of several synchronous generators.

In power systems with a high penetration of inverter-interfaced generation sources, and in microgrids in particular, the frequency stability is highly related to the low system inertia resulting from the lack of rotating machines. The increasing penetration of non-rotational generation poses risks to the microgrid frequency stability if the frequency controllers are not properly designed. This issue can also be observed in modern large-scale power systems, where many generation units are highly distributed, variable, and based on power electronics converters.

System inertia in traditional power system

In traditional power systems where the electricity comes from synchronous generators in power plants, the system inertia refers to the kinetic energy stored in the rotating parts of these machines. As the grid frequency is inherently linked with the rotating speed, rotors feature natural reactions to the contingencies in the system, which results in frequency fluctuations. With the high physical inertia of rotors, the large amount of the stored kinetic energy serves as an immediate source of energy that reduces frequency excursions following power imbalance. This stored energy helps with frequency regulation by catering for the load change or compensating the power lost from the failed generators. This inertia can be represented by a per-unit inertia constant H, whose value determines the ability to maintain the frequency during events. A typical frequency response of a generator during a load change is illustrated in Fig. 2.6, where the contingency occurs at $10\,\mathrm{s}$. The curves show the trend when H increases from 1 to 10. It is clear that a higher inertia contributes to a higher frequency nadir and a lower RoCoF, while the frequency deviation at steady state is not influenced by H.

Comparatively, RES such as solar PV and wind turbines provide no physical inertia because of

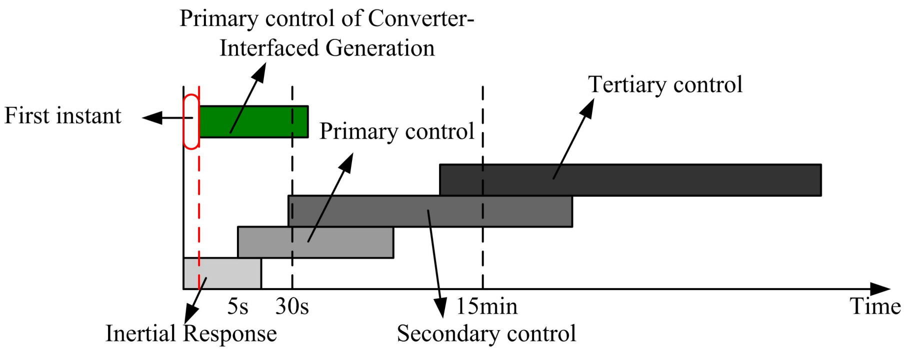

Figure 2.7: Time scales of frequency-related dynamics in conventional power systems and converter-interfaced DER [2].

the application of power electronic interfaces. Hence, a high RoCoF will be caused in response to contingencies. Unacceptable high RoCoF poses risks on generating units in terms of pole-slipping and protective tripping [127]. Large frequency excursions may also cause undesirable load-shedding, cascading failures, or even large-scale blackouts [76]. Moreover, the frequency stability is largely jeopardized especially in islanded microgrids. As a result, lack of system inertia is becoming a big concern in modern power systems.

Inertia enhancement in modern power system

To address this issue, a straightforward solution is to install synchronous condensers in the system, while this inevitably introduces higher costs. Hence more economical possible solutions consider making power-converter-interfaced DER participate in frequency control. Power converters are generally fast and can thus allow non-synchronous generators to provide a primary frequency control faster than conventional power plants. Authors in [2] compares the frequency-related dynamics in conventional generator-dominated system and the frequency control that can be provided by converter-interfaced DER in terms of time-scale process, which is shown in Fig. 2.7. In a conventional power system, the inertia of synchronous generators takes effect in the first instants after a contingency such as a step load change, which is known as the inertial response. This is not a controlled but a natural response of generators depending on the inherent characteristic. After this period, the primary, secondary, and tertiary controls by the system governors start to matter in a row. In comparison, the frequency control by converter-interfaced DER cannot capture and thus compensate the power balance in the first instants after contingencies as they do not respond naturally to the load change. Even though their primary frequency control is much faster than that of synchronous generators, the uncovered first instants tend to result in high RoCoF.

Against this backdrop, the research on dealing with the low inertia issue considers emulating the dynamic behaviour of synchronous generators, thus providing virtual inertia. Control strategies for DFIGs were proposed in [128–131] for wind turbines by emulating the inertial response of synchronous generators. Even though wind turbines also store kinetic energy in the blades, this energy cannot be directly used for energy compensation as rotational speed is decoupled from the grid frequency by power converters. To emulate the inertial response, the derivative of grid frequency $\frac{df}{dt}$ is measured to calculate the expected torque of wind turbines. One concern of this strategy is the speed recovery of wind turbines after frequency control. Some papers consider to use solar PVs to provide FFR to the system [132, 133]. The strategy in [132] measured the frequency first and then generates power feedforward for the DC-link voltage controller. A maximum power point (MPP) estimation algorithm was applied in [133] to predict the PV maximum power in real time and then provide fast and accurate control of active power. However, to be enabled to provide extra power, PVs have to operate below the MPP at the sacrifice of maximum power capacity. As a result, such strategy is only applicable in PV-rich areas. Among the primary sources of these power-converter-based generations, energy storage units are effective sources to provide inertia. This is mainly due to the feature of fast response and flexible power dispatch.

One effective method for inertia support is to utilize the energy stored in the DC-link capacitor. Active power regulation can be achieved by adjusting the DC-link voltage. Inertia enhancement approaches based on DC-link voltage control were reported in [52, 134–139]. Virtual synchronous generators (VSGs) were applied in [52, 134–136, 139] to implement the generators' swing equations in the power converter. Authors in [135] proposed a self-tuning method for the inertia and damping coefficients, while [136] divided the inertial response of a single VSG into four periods, and the inertia and damping coefficients are adjusted by different values to ensure the stability and to deal with the tradeoff among the RoCoF, the frequency nadir, the overshoot, and the settling time. In [52], the inertial response of VSGs were improved by employing a fuzzy controller in both grid-connected and islanded modes of AC microgrids.

Although arbitrarily assigning the virtual inertia of VSGs can be simple and straightforward, it is based on the assumption that VSGs can output or absorb infinitely large power, which is far from being proven. In fact, in order to produce the desired inertia, energy storage units have to be incorporated into VSGs. Without energy storage, the virtual inertia of VSGs would be limited by their DC-link capacitance [140]. Therefore, [134] applied a VSG sourced by a battery/ultracapacitor hybrid energy storage system. An observer-based transient frequency drift compensation was proposed in [141], using a battery for inertia support. The frequency drift compensation contains: transient state detection by an integral window; a proportional-derivative (PD) controller to regulate the frequency error; a Luenberger observer to observe the load disturbance.

The inertia enhancement strategies mentioned above are based on frequency measurement by PLLs. However, a PLL often fails in weak grids especially after severe faults, resulting in PLL instability issues and the inaccuracy of frequency estimation. Moreover, the implementation of swing equations should use the derivative of the grid frequency, while direct differentiating process introduces high-frequency noises. To deal with this issue, the PLL instability was investigated and improved in [142–145], aiming to provide inertia support and FFR. Improved frequency-locked loop (FLL) was reported in [146] for inertia enhancement. This paper studies a case in which a voltage-controlled VSM and a battery-based power converter are connected in parallel, supplying a changing load. It adopts a second-order generalized integrator (SOGI) in a FLL to generate the derivative of the estimated frequency, which is then used to calculate the desired compensated power from the battery. Authors in [139] proposed a self-synchronized VSG which is not dependant of the frequency measurement.

The grid synchronization function is realized in the DC-link voltage controller which generates the expected output frequency.

2.4.4 Voltage stability

An important stability issue in microgrids is to maintain terminal voltages at each bus within acceptable limits, and such ability is referred to as the *system strength* as one of the power system capabilities [147]. A strong grid can be thought of as an ideal voltage source in series with a low impedance. System strength is reduced when synchronous machines are replaced by inverter-interfaced generation connected to weak grids, i.e. distribution networks possibly far away from transmission substations. Grid-forming inverters, on the other hand, can help strengthen the grid because they can be represented by ideal AC voltage sources behind a low output impedance [22]. As a result, the voltage stability is enhanced by the penetration of grid-forming inverters.

Reactive power limits, load dynamics, and tap changers are the main sources of voltage stability issues in microgrids. Particularly, voltage stability issues are closely related to the reactive power limits, especially during islanded operation [148]. As microgrids commonly depend on short feeders, any changes in the DER terminal voltages are almost immediately reflected in the rest of the system [149]. Lack of sources of reactive power poses a risk on the system even with small disturbances. Therefore, proper reactive power compensation and management is crucial in microgrids for voltage stability enhancement. A control strategy of additional power converters connected in parallel with main converters is proposed in [150] to support extra reactive power for the microgrid. The low voltage ride-through capability is augmented with the added converter, which withstands the severe voltage dip. In [151], system stability is enhanced by a distribution static compensator (DSTATCOM) in an autonomous microgrid with multiple DG. The connected DSTATCOM provides ride-through capability during power imbalance in the microgrid. In addition, voltage stability can be improved by proper reactive power sharing among DER. Optimized droop equations have been reported in [152–154] for accurate reactive power sharing under feeder impedance mismatch. Adaptive and enhanced virtual impedance has been proposed in [36, 41–43] for the modification of conventional droop approaches. Moreover, algorithm-based reactive power sharing methods with graph theory were proposed in [155–157]. Reactive power sharing is improved with the schemes on the secondary control level.

2.4.5 Newly-added stability issues in modern power systems

The modern power system has been transformed significantly by the increasing integration of power electronic converters. In addition to the penetration of RES and ESS as introduced in previous subsections, novel transmission technologies such as flexible AC transmission systems (FACTS), high voltage direct current (HVDC) transmission lines and power-electronic-based loads change the character of modern power systems. The classification and definition of power system stability is extended in [158] by two new categories: converter-driven stability and resonance stability.

Converter-driven stability

The converter-driven stability is introduced by the interaction between converter-interfaced generations (CIG) and the networks. Controllers for CIG often feature multiple control loops with various bandwidths, resulting in dynamic phenomena with a wide range of time constants. For example, the inner current loops of CIG are much faster than the outer power and voltage loops. Similarly, components in power networks are with various dynamics, including fast-response components like passive filters and slow-response units like electromechanical dynamics of synchronous generators. In this regard, the interactions between fast-response units of CIG and networks cause high frequency oscillations, while interactions between slow-response units result in low-interaction stability issues. Proper design of control strategies and parameter tuning for CIG helps enhance the converter-driven stability.

Resonance stability

Resonance stability results from the growing oscillations in voltages, currents and mechanical torques. Such oscillations occur with power exchanges periodically in an oscillatory manner. The cause of resonance stability issue is twofold as classified in [158]: torsional resonance and electrical resonance. Torsional resonance is due to the interactions between the series compensations and the turbine-generator shaft. When large amount of power is exchanged between the network and a turbine-generator, the oscillation can be resulted with poor damping or even negative damping, which threaten the mechanical integrity of the shaft. Electrical resonance occurs when the system is penetrated by DFIG, which are essentially inductive generators connected directly with the grid. The series compensated capacitors and the effective inductance in the DFIG may form resonant circuits, causing electrical resonance. Authors in [159] showed that such electrical resonance can be mitigated by supplementary control loops for DFIG.

2.5 Literature gaps

2.5.1 Stability of the residential microgrids

The existing residential microgrid literature focused on the local controllers, optimal energy management, and simulation setup. However, the studies neglected stability issues. Despite the rich literature in microgrid stability studies, not much attention has so far been paid to the impact of the topology on microgrid stability. Authors in [160] used graph theory to show that a microgrid becomes "practically unstable" as progressively more inverters are added to a radial feeder. Based on the concept of algebraic connectivity, they concluded that the system's critical eigenvalue approaches zero with the microgrid expansion. However, they modelled inverters as ideal voltage sources without an explicit representation of the inverter control. Because the small-signal stability of a microgrid is related to feedback controllers [7], residential prosumers should be explicitly modelled in stability analysis.

Additionally, many studies neglected the explicit model of the DC-side configuration, which were often simplified as ideal voltage sources [81, 97, 161, 162]. Some papers included the model of DC dynamics in their study, such as the DC-link capacitor behavior [82], the DC-stage converter controller [83], and the representation of the dynamic responses in DC primary sources [84]. However, impacts from the DC dynamics have not been specifically studied, and these are parts of the gaps that this thesis aims to fill.

2.5.2 Inertia enhancement in low-inertia system

Existing literature mostly considered to provide fast power compensation for the system by measuring the frequency deviation and thus generating desired power output. The provided inertia via methods depending on frequency measurement are basically emulated inertia which is not genuine inertia like that in synchronous generators. To enhance the genuine inertia, power converters need to be integrated as voltage sources. The inherent inertial response is thus provided by the DC-link capacitor like the release of energy in the rotors. Consequently, the DC-link voltage is highly related to the system frequency.

Some literature designed inertia support strategies by linking the powers in the DC-link capacitor and the frequency deviation, such as the cases in [134, 140]. However, the DC voltage and the system frequency are not directly linked, and the expected power is calculated by the measured frequency deviation. Therefore, this thesis argues that grid-forming inverters acting as voltage sources can enhance the inertial response by releasing the energy in the DC-link capacitor instantly, providing genuine inertia to the system. There exists several grid-forming control methods as discussed in Section 2.3. This thesis discusses how matching control which directly links the DC voltage and the frequency contributes to the inertia enhancement.

2.6 Summary

This chapter reviews recent research relevant to the control and stability of residential microgrids. A brief introduction of microgrids and the basic hierarchical control structure are discussed first, followed by the literature review of residential microgrids, which consist mostly of single-phase prosumers. Due to the fact that prosumers are integrated into the microgrid via power converters, literature relevant to the control of power converters is reviewed, followed by a definition of grid-forming control and grid-following control which are applied in this thesis. To construct a residential microgrid, prosumers should be controlled by grid-forming methods. Hence, researches on different categories of grid-forming control methods are discussed then, among which the droop control and matching control are adopted in subsequent chapters. After that, research works on microgrid stability are reviewed. One of the stability issues is the frequency stability mainly caused by the low inertia. Thus, focusing on the inertia improvement, relevant literature is reviewed for dealing with the low inertia in modern power systems.

The literature gaps are discussed after the overview of existing works on relevant topics. The gaps that this thesis mainly aims to fill are twofold: the stability of residential microgrid with increasing number of grid-forming prosumers and limited DC dynamic response, and the inertia enhancement with voltage-source-like grid-forming converters which are adopted by the matching approach. The basic control structure of grid-forming prosumers is to be introduced and discussed in the next chapter, serving as the foundation of the research in this thesis.

Chapter 3

Control of Grid-Forming Prosumers in Residential Microgrids

Grid-forming prosumers represent prosumers whose distributed energy sources (DER) are integrated to a common low-voltage (LV) feeder as voltage sources by being controlled in the grid-forming mode. As discussed in Chapter 1, we consider designing a LV feeder as a residential microgrid by integrating grid-forming prosumers to the feeder, in which case the resiliency is highly improved. Therefore, control techniques for grid-forming prosumers are important to the proper operation of such a system.

Prosumer-owned DER are mostly in the DC form (e.g. solar PV, battery energy storage, etc). Hence, these prosumers are integrated into the common feeder by DC-AC inverters based on power electronics switching devices controlled by pulse width modulation (PWM) technique. To avoid high-order harmonics caused by the switching devices which negatively impact sensitive loads in the network as well as producing losses, the inverter should be integrated to the network via proper filters.

Basically, three common output filters are used to attenuate the high-order harmonics of the inverter, which can be classified as *L*, *LC*, and *LCL* filters. First-order passive *L*-type filters are normally used for grid-tied inverters. However, they may require a very large inductance, which increases not only the price but also the losses due to the large voltage drops. In comparison, the inductance of an *LCL* filter can be selected with lower value, thereby reducing the losses. The main drawback of the *LCL* filter is that it introduces a resonant frequency which might cause instability. *LC*-type filters have been widely applied to regulate the output voltages at the AC terminals, and it is mostly used for supplying a single load. Power converters with *LC* filters are often integrated into the system by coupling inductors to provide a reasonable coupling impedance between the inverter output and the connection bus [81], which makes the filter shaping as the *LCL* filter.

In practice, an *LCL* filter should be designed with passive or active damping methods for the sake of ripple attenuation and avoiding high-frequency resonance [163]. This thesis, however, does not focus on the high-frequency dynamics resulted by switching process. Hence, the damping method is not considered when studying the grid-forming prosumers. A simple *LCL* filter without the damping part is considered as a general representation. Interested readers can refer to [163–165] for more details on the damping methods for *LCL* filters.

In terms of the DC-side generation, residential prosumers tend to install solar PV and energy storage systems (ESS), such as batteries, fuel cells, and micro-turbines. The combination of PV and storage system is a good option for reducing the energy expenditure of the prosumer and ensuring coordinated energy flow management for the community. At the output side of the DC energy source, a DC-link capacitor is used to improve the decoupling between the energy source and the inverter. In terms of a three-phase inverter, the relations between AC terminal voltages and the DC-link voltage are

$$\boldsymbol{v}_{\mathrm{t,abc}} = \frac{v_{\mathrm{dc}}}{2}\boldsymbol{m}_{\mathrm{t,abc}} = \frac{v_{\mathrm{dc}}}{2}\begin{bmatrix} m\left(t\right)\sin\left(\omega_{\mathrm{c}}t+\theta_0\right) \\ m\left(t\right)\sin\left(\omega_{\mathrm{c}}t+\theta_0-\frac{2\pi}{3}\right) \\ m\left(t\right)\sin\left(\omega_{\mathrm{c}}t+\theta_0+\frac{2\pi}{3}\right) \end{bmatrix}, \tag{3.1}$$

where $m(t)$, ω_{c} and θ_0 are the amplitude, frequency and the initial phase of the modulating signals for the inverter, respectively. As $0 < m(t) < 1$, the minimum DC-link voltage is limited by

$$v_{\mathrm{dc}} \geq 2v_{\mathrm{mag}}, \tag{3.2}$$

where v_{mag} is the magnitude of the output voltage. This limitation allows current controllability and avoids over-modulation. Minimum required DC-link voltages for different modulation cases can be determined as [166]:

$v_{\mathrm{dc}} \geq v_{\mathrm{mag}}$ for single-phase systems;
$v_{\mathrm{dc}} \geq \sqrt{3}\, v_{\mathrm{mag}}$ for three-phase systems with space vector modulation (SVM) scheme;
$v_{\mathrm{dc}} \geq 2v_{\mathrm{mag}}$ for three-phase systems with a sinusoidal PWM scheme (SPWM).
To meet the DC voltage requirement, DC-DC converters are often employed between the DC energy sources and the inverters, which helps optimize the power extraction from the sources and regulate the DC-link voltages.

Therefore, control techniques are applied on the inverters and the DC stage converters to integrate local prosumers. The general configuration of a grid-forming prosumer with a single line diagram is shown in Fig. 3.1. A prosumer can be either three-phase or single-phase. As discussed in Chapter 2, grid-forming control strategies are categorized as P/Q droop control, virtual synchronous machines, matching control and virtual oscillators. In this thesis, the P/Q droop control method and matching control are applied in different chapters. The P/Q droop method is adopted in Chapter 4 with the low-level cascaded V-I controllers as a typical control structure of grid-forming inverters. The matching control, on the other hand, is adopted in Chapter 3 and 6.

This chapter starts with the explanation of the control methods of the inverter, the DC-stage converter, and the single-phase grid-forming prosumer. The inverter controller is being implemented by the grid-forming approaches. Controllers for the DC-stage converters are discussed then, which ensure PV's maximum power point tracking (MPPT) and the bidirectional power flow of the energy storage system. The single-phase grid-forming prosumer controller is derived from the control structure of the three-phase one, with quadrature-signal generation units. After that, the chapter provides a case study of power sharing in an islanded residential microgrid based on matching control. In particular, how to

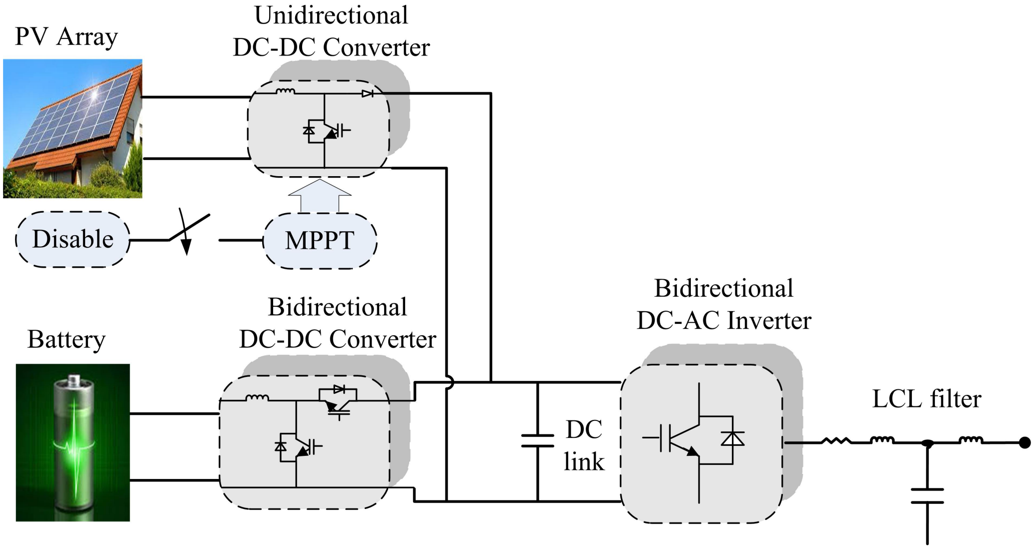

Figure 3.1: Single-line diagram of a grid-forming prosumer.

implement the matching control with the power-sharing method is discussed. Such implementation is also adopted for the genuine inertia enhancement in Chapter 6. This explains in detail about how grid-forming and power-sharing functionalities are validated by the controllers of both the inverter and the DC-stage converters.

3.1 Inverter control approaches

3.1.1 *P/Q* droop method

The inverter control strategy defines the behaviour of the inverter. When grid-forming inverters are integrated into the common LV feeder, the LV network is designed as a residential microgrid. To ensure the stable operation of the residential microgrid, the active and reactive powers in the microgrid should be properly shared. According to Chapter 2, the droop control method is widely applied due to its role of the well-developed power-sharing method without the use of communication lines.

The *P/Q* droop methods applied by grid-forming inverters are expressed as

$$\omega_{\mathrm{c}} = \omega^* - m_{\mathrm{P}} P, \tag{3.3a}$$

$$v^*_{\mathrm{mag}} = v_{\mathrm{nom}} - n_{\mathrm{Q}} Q, \tag{3.3b}$$

where ω^* and v_{nom} are the nominal frequency and the magnitude of the converter terminal voltage, respectively; m_{P} and n_{Q} are active and reactive droop coefficients, respectively; P and Q are the filtered active and reactive powers, respectively. The amount of the shared power is determined by the values of droop gains. In terms of the active power sharing, the frequencies generated by each inverter are taken as identical in steady state [166]. Thus the relations can be written as

$$m_{\mathrm{P1}} P_1 = m_{\mathrm{P2}} P_2 = \cdots = m_{\mathrm{P}n} P_n, \tag{3.4}$$

where n is the number of converters that conduct load sharing. The droop gains $m_{\mathrm{P1}} \sim m_{\mathrm{P}n}$ can be selected as identical to make the active power equally shared among the prosumers. As a comparison,

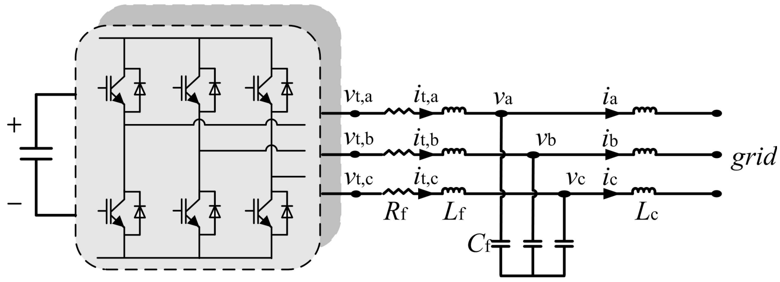

Figure 3.2: Three-phase inverter with *LCL* filters.

the sharing of reactive power presents an error when the droop coefficients are chosen equal because the voltage amplitude is a local variable. This droop method is also improved by supplementary techniques such as virtual impedance, adaptive droop and supplementary power controllers to cater for some additional requirements, especially in predominately resistive LV distribution networks. This thesis takes consideration of the basic droop method in (3.3a) and (3.3b) as a general control scheme for grid-forming prosumers.

3.1.2 Low-level cascaded control in the dq0 frame

The low-level cascaded control is to ensure that the output voltage of the inverter tracks its desired reference. Based on the PI controller, the control structure contains an inner current controller and an outer voltage controller, and all control variables are transformed into the dq0 frame due to the fact that PI controllers cannot achieve zero-error tracking of the AC variables, such as the three-phase voltages and currents. Considering a balanced three-phase system, the three-phase AC variables can be transformed from abc to dq0 frame by

$$\boldsymbol{x}_{\text{dq0}} = \frac{2}{3}\begin{bmatrix} \sin\theta_{\text{c}} & \sin\left(\theta_{\text{c}} - \frac{2}{3}\pi\right) & \sin\left(\theta_{\text{c}} + \frac{2}{3}\pi\right) \\ \cos\theta_{\text{c}} & \cos\left(\theta_{\text{c}} - \frac{2}{3}\pi\right) & \cos\left(\theta_{\text{c}} + \frac{2}{3}\pi\right) \\ \frac{1}{2} & \frac{1}{2} & \frac{1}{2} \end{bmatrix} \boldsymbol{x}_{\text{abc}}. \tag{3.5}$$

A system diagram of the two-level three-phase inverter with a *LCL* filter is illustrated in Fig. 3.2. Control objectives are output three-phase currents $i_{\text{t,abc}}$ and three-phase voltages v_{abc} as shown in Fig. 3.2. Therefore, the cascaded controller can be designed according to the current loop and the voltage loop, respectively.

Current control loop

Following the circuit diagram in Fig. 3.2, the inverter output currents for the three-phase system can be expressed as

$$L_{\text{f}}\dot{i}_{\text{t,a}} + R_{\text{f}}i_{\text{t,a}} = v_{\text{t,a}} - v_{\text{a}}, \tag{3.6a}$$

$$L_{\text{f}}\dot{i}_{\text{t,b}} + R_{\text{f}}i_{\text{t,b}} = v_{\text{t,b}} - v_{\text{b}}, \tag{3.6b}$$

$$L_{\text{f}}\dot{i}_{\text{t,c}} + R_{\text{f}}i_{\text{t,c}} = v_{\text{t,c}} - v_{\text{c}}. \tag{3.6c}$$

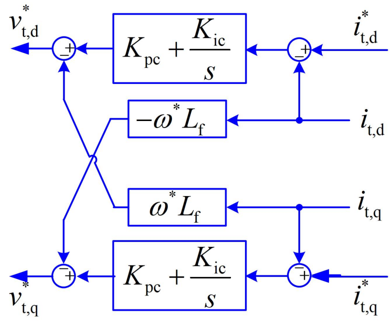

Figure 3.3: Current loop controller.

Apply (3.5) to the three-phase model results in

$$L_f \dot{i}_{t,d} + R_f i_{t,d} - \omega_c L_f i_{t,q} = v_{t,d} - v_d, \tag{3.7a}$$

$$L_f \dot{i}_{t,q} + R_f i_{t,q} + \omega_c L_f i_{t,d} = v_{t,q} - v_q, \tag{3.7b}$$

where $\boldsymbol{v}_{t,dq}$, $\boldsymbol{v}_{dq}$, and $\boldsymbol{i}_{t,dq}$ are the corresponding variables in the dq0 frame. It can be seen in (3.7) that the dynamics of $\boldsymbol{i}_{t,dq}$ are coupled to each other by the terms $\pm\omega_c L_f \boldsymbol{i}_{t,dq}$. Therefore, a pair of cross-decoupling terms will be added to the voltage references to simplify the control structure. The current controller diagram is shown in Fig. 3.3. K_{pc} and K_{ic} are the proportional and integral gains, respectively.

Voltage control loop

The voltage controller is to ensure that the output voltages $\boldsymbol{v}_{abc}$ track the voltage references generated by the power controllers. As voltage controllers serve as the outer loop of the cascaded controller, the output of the voltage loop are the references for the inner current controllers. Similar as the current control loop, the voltages are controlled in the dq0 frame, and the dq variables are mutually coupled, which is shown as

$$C_f \dot{v}_d - \omega_c C_f v_q = i_{t,d} - i_d, \tag{3.8a}$$

$$C_f \dot{v}_q + \omega_c C_f v_d = i_{t,q} - i_q. \tag{3.8b}$$

Therefore, the current references will be generated with cross-decoupling terms, which is shown in Fig. 3.4. K_{pv} and K_{iv} are the proportional and integral gains, respectively. $\boldsymbol{v}_{t,dq}$ and $\boldsymbol{i}_{t,dq}$ can also be integrated as extra feed-forward terms based on the output voltage $\boldsymbol{v}_{dq}$ and currents $\boldsymbol{i}_{dq}$ to different extents, depending on the design requirements.

Briefly, in the grid-forming inverter control approach, the voltage references are generated by the P/Q droop method or the matching control approach, and are then tracked by the low-level cascaded controller.

3.1.3 Control of single-phase inverters

Residential microgrids typically use single-phase generation sources because the power service to individual houses is generally single phase. In a distribution network, several houses are typically

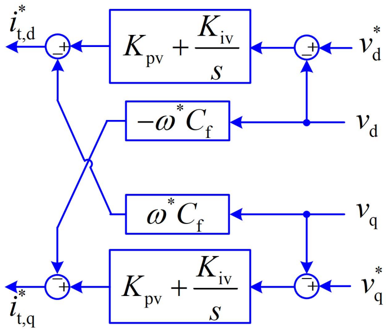

Figure 3.4: Voltage loop controller.

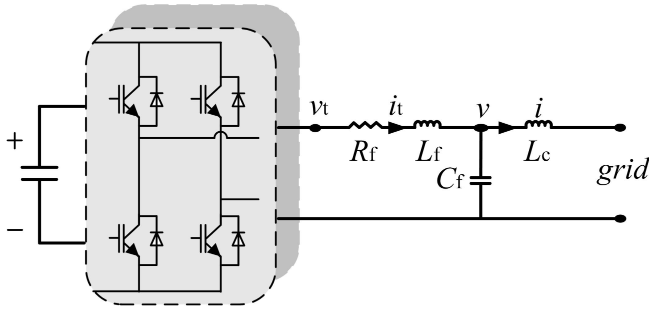

Figure 3.5: Single-phase inverter with an *LCL* filter.

supplied from a single-phase feeder that draws power from a distribution transformer. Against this backdrop, a three-phase residential microgrid is structurally formed by three separate single-phase systems. A typical single-phase inverter is shown in Fig. 3.5. Hence, the controller for single-phase grid-forming prosumers needs to be derived.

Unlike three-phase inverters, single-phase systems cannot be directly controlled in the dq0 frame as the single-phase AC variables do not inherently have a quadrature component. In this case, the reference output voltage and current of the inverter are sinusoidal time-varying signals following the phase calculated from the grid-forming method. Based on the internal model principle, PI controllers cannot properly track this reference due to the absence of the internal model of the sinusoidal input [167]. Therefore, the proportional-resonant (PR) controller applied in [11,168,169] as the resonance frequency equal to that of the reference (the frequency of the output voltage in this case) is adopted in the controller. The transfer function of a basic PR controller is given as

$$G_{\text{PR}}(s) = K_{\text{pr}} + \frac{K_{\text{ir}} s}{s^2 + \omega_{\text{res}}^2}, \tag{3.9}$$

where K_{pr} and K_{ir} are the proportional and the integral gains of PR controllers, respectively. From the transfer function, the PR controller has an infinite gain at a particularly resonant frequency ω_{res} which can be set as the output voltage frequency ω_{c}, making it capable of tracking an AC reference signal.

However, AC components are not easy for the stability analysis based on small-signal model. AC quantities are not kept constant during the steady-state operation, which disables the linearisation of the system with small-signal state variables. For the sake of stability analysis in this thesis, the single-phase inverter controller is also expected to be designed in the dq0 frame in which the quantities are DC components [170].

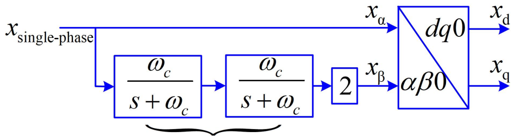

Figure 3.6: Quadrature signal generation with a standard transfer delay.

A possible solution is the quadrature signal generation method. A fictitious quadrature signal is created based on the single-phase voltage/current and then transformed into the dq0 frame. Multiple methods for generating the fictitious quadrature signal have been proposed [171]. A typical approach is to use the transfer delay (TD), as shown in Fig. 3.6. $x_{\text{single-phase}}$ represents the single-phase AC variables (v_{t}, i_{t}, v, i). The quadrature signal is constructed by delaying the original single-phase signal by a quarter of its period. The original and the fictitious quadrature signals serve as the αβ0 components which are transformed to the dq0 frame based on

$$\boldsymbol{x}_{\text{dq0}} = \begin{bmatrix} \sin\theta_{\text{c}} & -\cos\theta_{\text{c}} & 0 \\ \cos\theta_{\text{c}} & \sin\theta_{\text{c}} & 0 \\ 0 & 0 & 1 \end{bmatrix} \boldsymbol{x}_{\alpha\beta0}. \tag{3.10}$$

The $T/4$ delay is realized by two identical first-order systems in series. The cut-off frequency of the first-order system is the AC output frequency ω_{c} which is generated by the grid-forming method. A single first-order system gives a $\frac{\sqrt{2}}{2}$ gain and $-\frac{\pi}{4}$ phase shift as expressed in

$$|G(j\omega)|_{\omega=\omega_{\text{c}}} = \left|\frac{\omega_{\text{c}}}{j\omega_{\text{c}}+\omega_{\text{c}}}\right| = \frac{\sqrt{2}}{2}, \tag{3.11a}$$

$$|\varphi(j\omega)|_{\omega=\omega_{\text{c}}} = \angle\frac{\omega_{\text{c}}}{j\omega_{\text{c}}+\omega_{\text{c}}} = -\frac{\pi}{4}. \tag{3.11b}$$

Therefore, when two identical first-order systems connected in series, the input signal is halved in magnitude and shifted by $-\frac{\pi}{2}$ in phase, which creates the quadrature signal. This method is more accurate in the application of grid-forming inverters than that of grid-following inverters based on phase-locked loops (PLLs) because the frequency is generated by the individual inverter. Based on this method, the single-phase inverter can be controlled by the low-level cascaded control loops as shown in Section 3.1.3.

3.2 DC-stage converter control approach

On the DC side of the inverter, DC-stage converters are often applied to integrate the DC generation sources with the inverter for the sake of the DC-link voltage requirement, the charging/discharging current control for energy storage and the MPPT for solar PVs. Depending on the power flow directions, DC-stage converters are classified as unidirectional and bidirectional converters. Bidirectional DC/DC converters (BDCs) are applied for the energy storage as a result of the energy flow in both forward and reverse directions, while unidirectional DC/DC converters are implemented to cater for the one-way power flow in the case of solar PVs.

As previously discussed, grid-forming inverters owned by prosumers are often implemented by droop control to exhibit load sharing. This means the generation from the DC side needs to adjust its power output to supply the load increase. However, most solar PVs are controlled by MPPT to generate the maximum power [172]. If nothing changes in the environment (e.g. temperature and irradiance), the power from PVs is constant. In other words, PVs controlled by MPPT have no extra power to supply the increasing load unless the operation point deviates from the maximum power point, and this is not acceptable to the prosumers due to associated financial loss. At the distribution level, even though some PVs are recommended to operate below the maximum power point or even to be curtailed for the sake of feeder voltage control [173], these PVs cannot be purposely designed for sharing extra loads as the power generation is inherently dependent on the environment. In comparison, ESS feature flexible power generation and fast response, which is much easier to manage. Hence, using ESS to supply grid-forming converters makes more sense.

At the demand side of the energy supply chain, consumers increasingly invest in rooftop PV-battery systems [174, 175]. In such systems, batteries and PVs are connected in parallel and interfaced with the AC grid by a hybrid inverter. The advantage of such PV-battery systems is that the PV can operate in MPPT while the battery can serve as backup energy supply for the extra load sharing. Excessive power from the PV can be used either to supply the load or to charge the battery. The MPPT control only needs to be disabled when the battery's state of charge (SOC) is beyond the maximum limitation. Therefore, the BDC for the energy storage is expected to conduct the control of the DC-link voltage and the charging/discharging current, while the unidirectional DC/DC converter for the PV mainly achieves the MPPT to extract the maximum power.

3.2.1 Control of the bidirectional DC/DC converter

A BDC is required to process bidirectional power flow between the batteries and other generation units in the network [176]. Based on the presence of an isolation device, BDCs are mainly classified into isolated and non-isolated converters. A non-isolated bidirectional converter is realized by multiple power-electronic switches and diodes based on the topology from conventional DC/DC converters such as Buck, Boost, Cuk, etc. Non-isolated topologies feature small size and low weight. Such topology is suitable for applications with relatively low voltage step-up gain ratio. A fundamental non-isolated topology is based on the original buck and boost converter shown in Fig. 3.7. In Fig. 3.7, L_{conv} and C_{dc} represent the inductor connected at the side with lower voltage level and the DC-link capacitor connected at the side with higher voltage level. R_{bat} indicates the internal resistance from the energy storage (taking a battery as the example). This topology applies the topology of conventional Buck and Boost converters. The only difference is that this topology contains two controllable switches S_1 and S_2, which are controlled by two mutual-complementary switching signals generated by the duty cycle d. The power flow direction depends on the power difference between the battery and the system. Such topology is easy to implement and the control approach can be designed based on the control of the Boost converter.

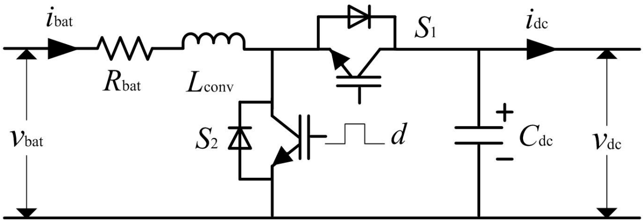

Figure 3.7: Buck/boost bidirectional DC/DC converter.

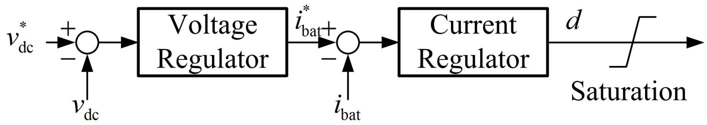

Figure 3.8: Cascaded Control for the Buck-Boost bidirectional DC/DC converter.

By contrast, the isolated bidirectional converter converts DC voltages to AC, followed by a high-frequency transformer that steps up or down the voltage to the required level. Then the converted AC voltage is rectified to DC. The voltage ratio of isolated topologies is generally higher than non-isolated ones. The disadvantage is the leakage inductance effect of the transformer.

In this thesis, we use the fundamental non-isolated topology in Fig. 3.7 for the study. Considering the necessity of ensuring the power balance between the primary power source and the microgrid, the DC-link voltage should be regulated to achieve bidirectional power flows. In addition, the current from the primary source which determines the charging/discharging process of the energy storage is also expected to be controlled properly. Therefore, the control structure for such Buck/Boost bidirectional converter is made up of a cascaded structure with an inner current loop and an outer voltage loop [177], which is shown in Fig. 3.8. A PI controller is often adopted in the current regulator to achieve a error-free tracking of the desired current reference. In the voltage loop, however, the regulator is designed according to the requirement of the DC-link voltage behavior, which is explained in Section 3.3.

3.2.2 Control of the unidirectional DC/DC converter

The unidirectional DC/DC converter integrates the PV to the inverter as well as detecting the maximum power point of the PV cells. A simple conventional Boost converter is applied in the PV integration by assuming that the PV output voltage is lower than the DC-link voltage. The MPPT algorithm is implemented in controlling the duty cycle for the Boost converter.

Fig. 3.9 shows the characteristics of PV modules including the current-voltage curve and the power-voltage curve. The PV will produce the maximum power (P_{mpp}) at the maximum power point with the corresponding voltage V_{mpp} and the current I_{mpp}. The PV current is relatively constant as the PV voltage increases from the origin to V_{mpp}, acting as a current source. During this period, the PV output power keeps increasing to the maximum power point. After the voltage exceeds V_{mpp}, the PV current starts to drop significantly and so does the output power until the voltage reaches the open-circuit voltage V_{OC}. The PV characteristics depends on the external conditions including the

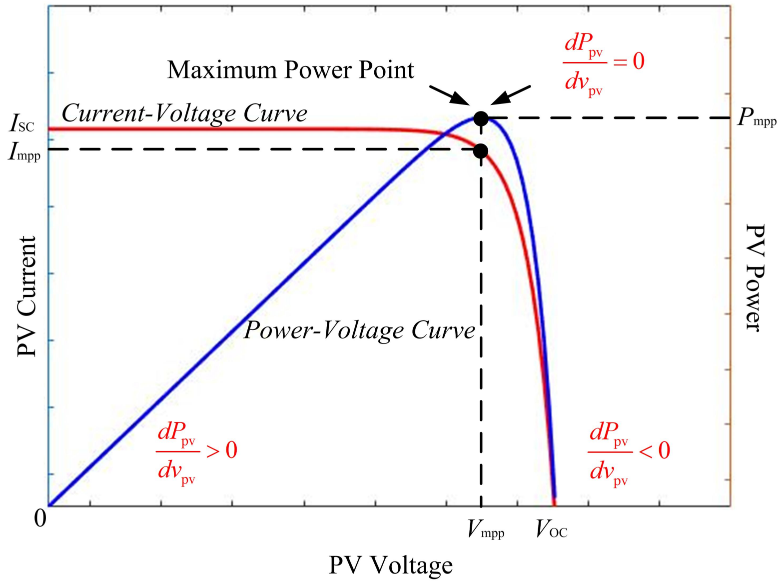

Figure 3.9: The characteristics of PV modules.

temperature and the solar irradiance. Thus, MPPT is applied for maximum power production.

A large number of MPPT algorithms have been reported in the literature [178–182]. Among those, the Perturb and Observe (P&O) method is the most commonly-used MPPT algorithm due to its simplicity and accuracy. According to Fig. 3.9, the operating point of the PV cell can be determined by the derivative of P_{pv} with respect to v_{pv} which can be expressed in the discrete form as

$$\frac{dP_{\mathrm{pv}}}{dv_{\mathrm{pv}}} = \frac{P_{\mathrm{pv}}\left(k\right) - P_{\mathrm{pv}}\left(k-1\right)}{v_{\mathrm{pv}}\left(k\right) - v_{\mathrm{pv}}\left(k-1\right)}. \tag{3.12}$$

A simple P&O MPPT controller can be developed, which enables the operating point to continuously and repeatedly climb up to the peak. This is realized by adjusting the duty cycle to control the Boost converter. The duty cycle is changed incrementally from an initial value in one direction first (increasing or decreasing). Then, the power of the PV modules is calculated based on the measured value of the PV voltage and current. The power is then compared with the previously-sampled value based on (3.12). The voltage at high-voltage side of the Boost converter is considered as a constant. Therefore, when the value of (3.12) is negative, the PV voltage needs to be increased to capture the maximum point, and this is realized by decreasing the duty cycle and vice versa. The duty cycle would be adjusted until the maximum point is captured. A flowchart of the P&O MPPT algorithm is shown in Fig. 3.10.

3.3 Power sharing in an islanded residential microgrid based on matching and droop control

In previous sections, the control of the grid-forming prosumers have been explained in details. To verify the feasibility of integrating multiple grid-forming prosumers into a common feeder, the islanded operation of a residential microgrid with only PV-battery systems is tested in this section. A grid-forming method based on matching control is proposed, augmented by a DC-link power compensation method. After the matching approach is implemented, the link between the DC-link

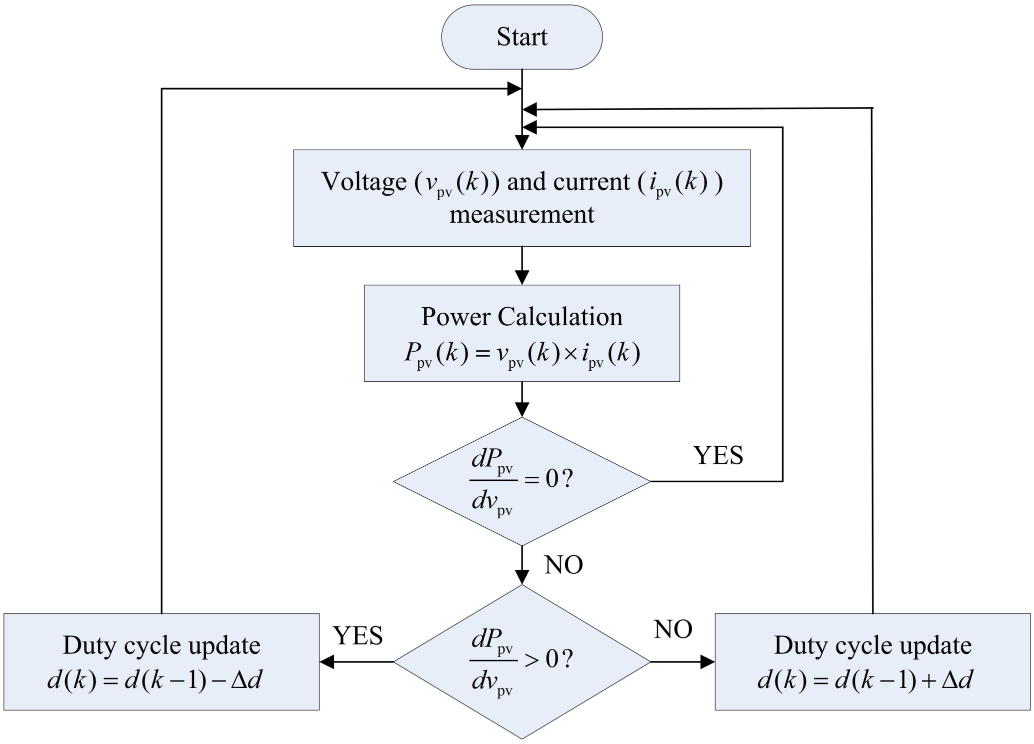

Figure 3.10: Flowchart of the P&O MPPT algorithm.

voltage and the rotor angular frequency is revealed. Frequency regulation can therefore be realized by controlling the DC-link voltage. Authors in [1] concluded that taking the DC-side dynamics into account while regulating the AC dynamics results in enhanced robustness with respect to large disturbances. Additionally, due to the fact that grid-forming inverters respond instantly to the load change and thus the power in the DC-link capacitor is released immediately after the load change, a power compensation can be conducted onto the capacitor relying on the change of DC-link voltage, which helps hold the frequency during the first instants after a contingency.

3.3.1 Power sharing method in the battery controller

The matching approach can be applied based on (2.9). In this way, the frequency shift in the grid is translated into the DC-link voltage change. This can be explained by observing the power balance immediately after a disturbance. A power change in the grid is initially compensated by the energy stored in the DC-link capacitor, similar to the inertial response coming from the kinetic energy stored in the rotating mass of a synchronous machine. Hence the voltage regulation basically applies an $i_{\mathrm{s}}/v_{\mathrm{dc}}$ droop control, which mimics the conventional P/f droop characteristic, and the DC current reference is determined by the sum of the droop controller output and the power injection feed-forward to adjust the power output [1]. This also interprets the trade-off between matching control and MPPT where the current output is nearly constant. In this case, the active power droop method should be applied in controlling the BDC.

Comparing Figs. 2.4 and 3.7, the matching control approach for a battery-sourced converter can be determined as shown in Fig. 3.11, where the “matching part” that mimics the synchronous generator is implemented in the AC side for the inverter control, which generates modulation signals. v_{nom}, v^*_{mag}

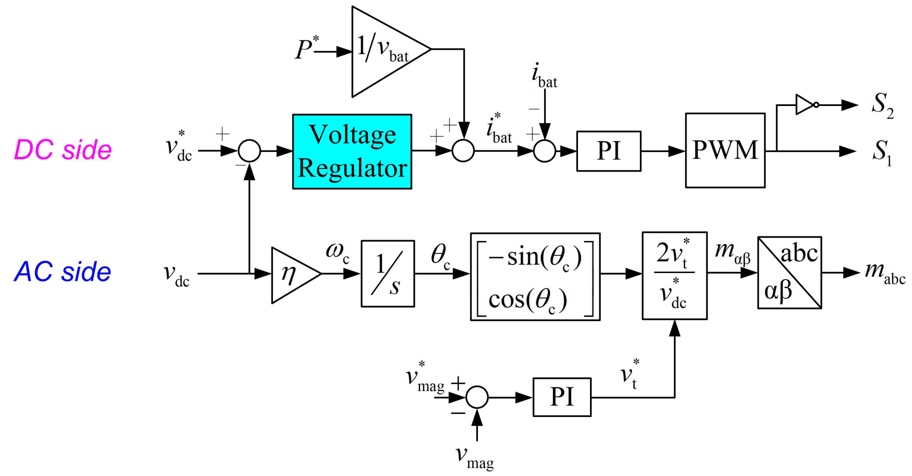

Figure 3.11: Matching control diagram for battery-sourced converter.

and v_t^* represent the nominal AC output voltage magnitude, the actual AC output voltage magnitude reference, and the inverter terminal voltage magnitude, respectively. DC voltage regulation and power injection part is implemented in the BDC to adjust the DC source output. P^*, v_{bat} and i_{bat} represent the initial power injection, the battery output voltage, and the battery output current, respectively. S_1 and S_2 are switching signals for the BDC. Based on the matching approach in (2.10), the active power droop will be applied in the form of $i_{\text{bat}}/v_{\text{dc}}$ droop which is implemented into the DC voltage regulator, as expressed in

$$i_{\text{bat}}^* = m_{\text{v}}\left(v_{\text{dc}}^* - v_{\text{dc}}\right). \tag{3.13}$$

The reactive power droop is applied as

$$v_{\text{mag}}^* = v_{\text{nom}} - n_{\text{Q}}Q, \tag{3.14}$$

where Q is the filtered reactive power obtained by

$$Q = \frac{\omega_{\text{f}}}{s+\omega_{\text{f}}}Q_{\text{meas}}. \tag{3.15}$$

Q_{meas} is the measured power calculated by v_{abc} and i_{abc}, and ω_{f} is the cut-off frequency of the low-pass filter.

3.3.2 Capacitor power compensation

In the matching control approach, converters behave like synchronous generators, which respond naturally to the load change. This equivalent behavior mainly depends on the DC-link capacitor, which serves as the immediate energy storage. The issue, however, is that this energy is limited and uncontrollable. Therefore, batteries will also serve as an additional energy source augmenting the capacitor. The power from the battery can be determined by controlling the battery current output. In this case, when the load change causes the capacitor releasing or absorbing power, we can observe the power change in the capacitor and thus feed it forward to the current reference to compensate for the change.

The energy stored in the capacitor is

$$E_{\mathrm{C}} = \frac{1}{2} C_{\mathrm{dc}} v_{\mathrm{dc}}^2. \tag{3.16}$$

So the power can be expressed as

$$P_{\mathrm{C}} = \frac{dE_{\mathrm{C}}}{dt} = C_{\mathrm{dc}} v_{\mathrm{dc}} \frac{dv_{\mathrm{dc}}}{dt}. \tag{3.17}$$

This power essentially represents the power absorbed by the capacitor as a result of the voltage change. Such change predominately takes place at the first instants after a system disturbance, acting as the inertial response. As C_{dc} is constant, it is obvious that the capacitor power depends on the voltage change. Rewrite (3.17) as

$$\begin{aligned} P_{\mathrm{C}} &\approx C_{\mathrm{dc}} v_{\mathrm{dc}}^* \frac{(v_{\mathrm{dc}}(k+1) - v_{\mathrm{dc}}(k))}{dt} \\ &= C_{\mathrm{dc}} v_{\mathrm{dc}}^* \frac{(v_{\mathrm{dc}}^* - v_{\mathrm{dc}}(k) - (v_{\mathrm{dc}}^* - v_{\mathrm{dc}}\,(k+1)))}{dt}. \\ &= -C_{\mathrm{dc}} v_{\mathrm{dc}}^* \frac{d\,(v_{\mathrm{dc}}^* - v_{\mathrm{dc}})}{dt} \end{aligned} \tag{3.18}$$

This power change will be compensated as a negative feed-forward term, which is interpreted as a derivative element for the voltage regulator. So the voltage regulator in Fig. 3.11 is essentially a proportional-derivative (PD) controller.

3.3.3 PV interface

As analyzed previously, PV can not be interfaced by MPPT and grid-forming control simultaneously because the MPPT does not leave any room for a potential power increase. However, when connected with a battery in parallel, the power adjusting feature is realized by the BDC and the inverter. In this case, the PV interface thereby serves as an additional power source with no need to perform grid forming. MPPT can be applied to get the maximum power output, extending the DC side power capacity on the other hand. Note that MPPT should be disabled when the battery is fully charged or the power generation is significantly larger than the consumption. Now, the complete control strategy for a PV-battery hybrid system (as given in Fig. 3.12) can be obtained by using (2.10), (3.13), (3.14), and (3.18).

3.4 Simulation results

In this section, we outline the results of a system-level simulation case of a residential LV distribution network fully supplied by prosumer-owned PV-battery systems, illustrated in Fig. 3.13. As the response on the converter side is much faster than the network, we do not pay much attention to the converter switching dynamics. Therefore, an average state-space converter model is used for a standard practice of this study, which also speeds up the simulation [183].

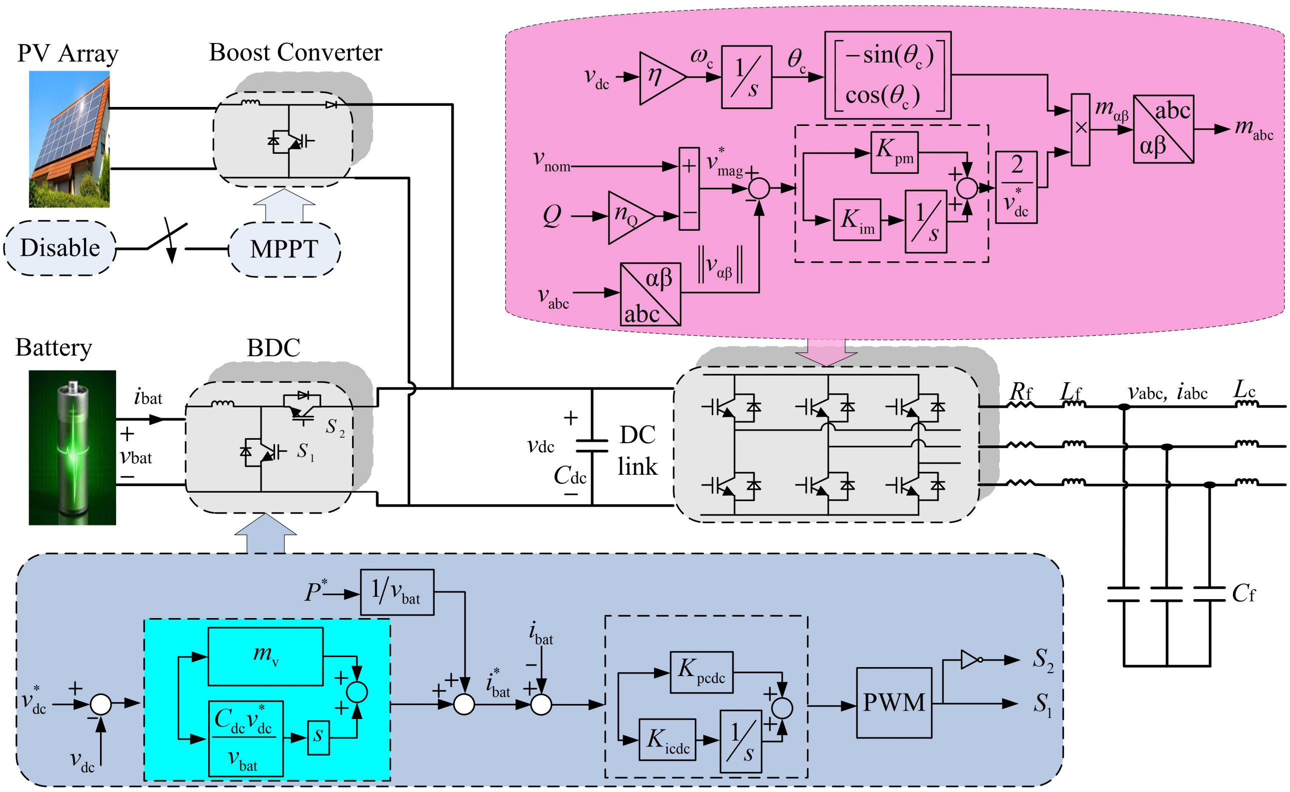

Figure 3.12: Proposed control strategy for PV-Battery hybrid system.

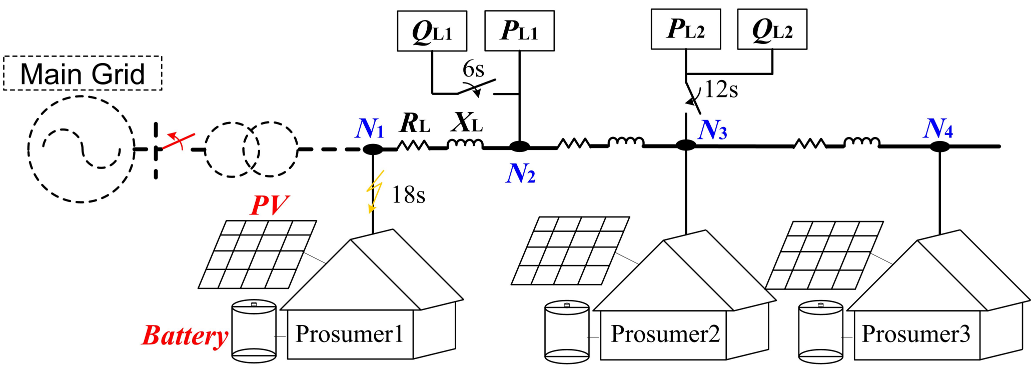

Figure 3.13: Residential LV network simulation case in Section 3.4.

3.4.1 Case study

The Matlab/Simulink LV network model consists of three identical PV-battery systems with hybrid inverters. All PV-battery systems are controlled by the strategy shown in Fig. 3.12. Adjustable loads are distributed at different buses of the system. This simulation will test how the system responds to load changes and system faults. As the case in which the amount of generated power exceeds that of the consumption is relatively simple, this simulation will mainly test the situation when batteries provide more power to the system as a result of increasing loads. Load change is realized by connecting new loads during the simulation and the loads are modelled as a constant impedance.

Model parameters are provided in Table 3.1: the LV network is a 400 V, 50 Hz system. The simulation operation is described as follows:

1. During 0-6 s, the system is in the initial steady state.

2. At $6\,\mathrm{s}$, the inductive load at N_2 increases by $0.5\,\mathrm{kVAr}$. This power change is to be shared by the three PV-battery systems. Then the network gradually reaches the new steady state until $12\,\mathrm{s}$.

3. At $12\,\mathrm{s}$, a new load is connected at N_3, with the active power at $0.8\,\mathrm{kW}$ and the reactive power at $0.5\,\mathrm{kVAr}$. The network reacted to this change until $18\,\mathrm{s}$.

4. At $18\,\mathrm{s}$, the PV-battery system at N_1 is disconnected, emulating a generation loss. The network would be supplied only by Prosumer 2 and 3 until $24\,\mathrm{s}$.

Table 3.1: Parameters in the residential LV network simulation case in 3.4

	Network	
P_1^*, P_2^*, P_3^*	Initial Power from batteries	$0\,\mathrm{kW}$
P_{L1}	Load1 active power	$4.5\,\mathrm{kW}$
Q_{L1}	Load1 reactive power	$0.5\,\mathrm{kVAr}$
P_{L2}	Load2 active power	$0.8\,\mathrm{kW}$
Q_{L2}	Load2 reactive power	$0.5\,\mathrm{kVAr}$
$P_{\mathrm{pv1}}^{\mathrm{m}}$, $P_{\mathrm{pv2}}^{\mathrm{m}}$, $P_{\mathrm{pv3}}^{\mathrm{m}}$	PVs maximum output power	$0.8\,\mathrm{kW}$
V_{base}	Grid nominal line-line voltage	$400\,\mathrm{V}$
f^*	Nominal grid frequency	$50\,\mathrm{Hz}$
R_{L}	Line resistance	$0.3\,\Omega$
X_{L}	Line inductance	$0.06\,\Omega$
	Converter	
v_{bat}^*	Nominal battery output voltage	$400\,\mathrm{V}$
v_{nom}	Phase voltage reference	$326.6\,\mathrm{V}$
C_{bat}^*	Nominal battery capacity	$400\,\mathrm{A\,h}$
R_{bat}	BDC Series inductance	$1\,\mathrm{m\Omega}$
L_{conv}	BDC Series inductance	$1.25\,\mathrm{mH}$
v_{dc}^*	DC-link voltage reference	$800\,\mathrm{V}$
C_{dc}	DC-link capacitor	$4000\,\mu\mathrm{F}$
R_{f}	AC series resistance	$10\,\mathrm{m\Omega}$
L_{f}	AC filtering inductance	$1.3\,\mathrm{mH}$
C_{f}	AC filtering capacitor	$50\,\mu\mathrm{F}$
	Control	
m_{v}	DC voltage droop gain	9.08
K_{pcdc}, K_{icdc}	Current PI gains	$0.005, 0.5$
n_{Q}	Reactive power droop gain	1.3×10^{-4}
K_{pm}, K_{im}	AC voltage magnitude PI gains	$0.15, 40$
ω_{f}	Low-pass filter cut-off frequency	$31.41\,\mathrm{rad/s}$

Fig. 3.14 shows the simulation results, which are analyzed by the operation sequence as follows.
0-6s: During this period, the system was operating in steady state.

- Only the resistive load was connected. From Figs. 3.14 (a1-4), it is clear that the active load was approximately $4.5\,\mathrm{kW}$, and the load was equally shared by Prosumer 1, 2 and 3 with the amount of approximately $1.5\,\mathrm{kW}$ each. This is because the active power droop gains for all prosumers

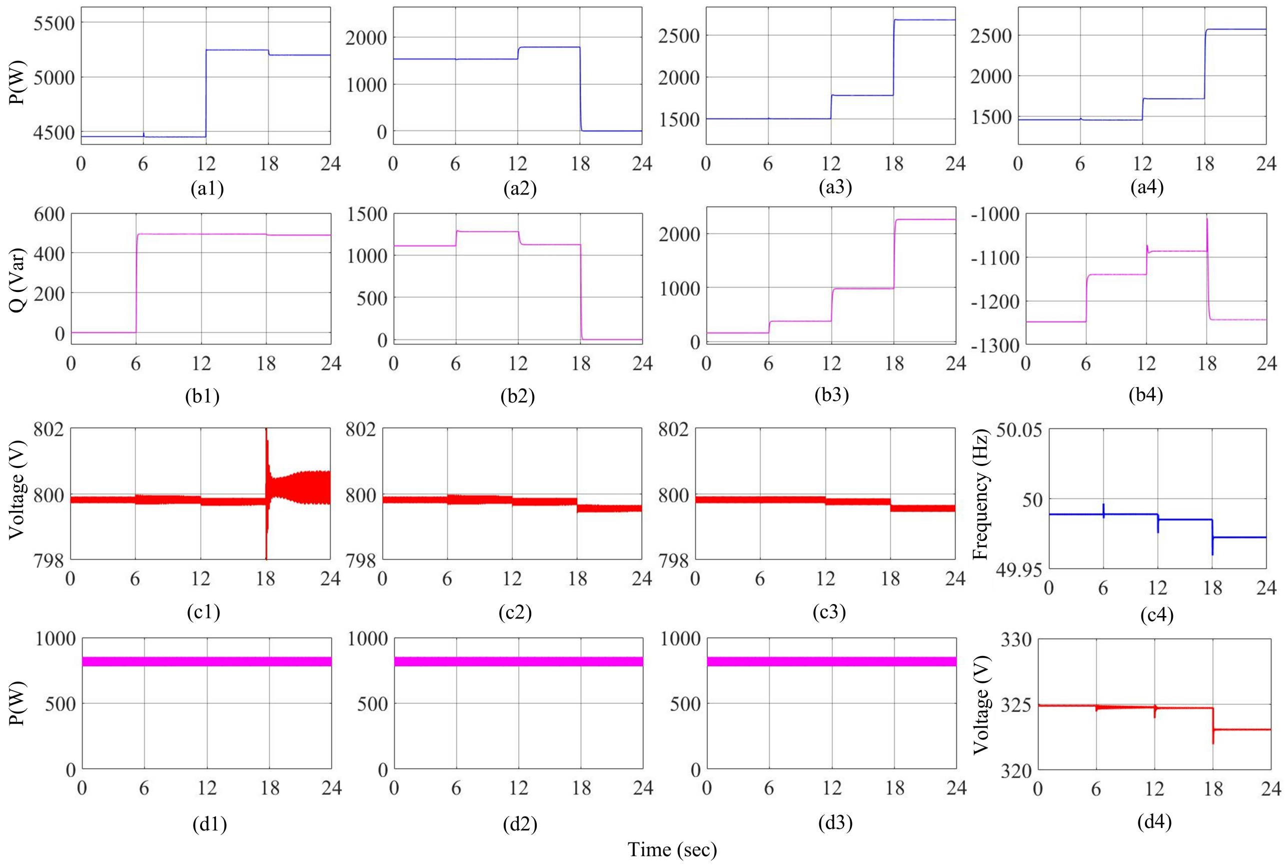

Figure 3.14: Simulation Results. (a1, 2, 3, 4) active power of load 1 and Prosumer 1, 2, 3; (b1, 2, 3, 4) reactive power of load 1 and Prosumer 1, 2, 3; (c1, 2, 3, 4) DC-link voltage of Prosumer 1, 2, 3 and grid frequency; (d1, 2, 3, 4) power from PV panels in Prosumer 1, 2, 3 and grid voltage peak value.

are equal. According to (3.4) which illustrates that the frequency is a global variable, total active power in the system is shared equally among all the prosumers.

- Figs. 3.14 (b1-4) shows the reactive power flow. The sum of the reactive power was kept at 0. However, the reactive powers at each prosumer are not all zero. This is because of the coupling between the frequency and the reactive power in the LV distribution network which is predominantly resistive. The amount of reactive powers are determined by the balanced power flow in the system.

- The system frequency was $49.985\,\mathrm{Hz}$ because of the $v_{\mathrm{dc}}/i_{\mathrm{bat}}$ droop, while the voltage peak value was lower than $326.6\,\mathrm{V}$ as a result of the Q/V droop, which can be seen in Figs. 3.14 (c4), (d4).

- PV output power from all prosumers were kept at $0.8\,\mathrm{kW}$ by the MPPT (see Figs. 3.14 (d1-3)).

6-12s: During this period, the inductive load at N_2 was connected with the amount of $0.5\,\mathrm{kVAr}$.

- It can be seen from Figs. 3.14 (b1-4) that this reactive power is shared by Prosumers 1, 2 and 3, while Prosumers 1 and 2 contributed more than Prosumer 3. This is mainly because the added inductive load is in between N_1 and N_3. The system experienced a fast and smooth transition after the load change. The voltage magnitude showed an decrease because of the Q/V droop, which can be seen in Fig. 3.14 (c4).

- By comparison, Figs. 3.14 (a1-4) shows that the active power experienced a slight oscillation but recovered quickly back to the original value. A similar variation was observed in the system frequency in Fig. 3.14 (d4).

12-18s: During this period, the load 2 was connected by an RL load whose consumed active and reactive powers are $0.8\,\mathrm{kW}$ and $0.5\,\mathrm{kVAr}$, respectively.

- It can be seen from Fig. 3.14 (a2-4) that all prosumers experienced an increase in active power immediately after the load change. After that, the power increase was mainly equally shared by Prosumer 1, 2 and 3.

- In comparison, the reactive powers of Prosumer 2 and 3 both increased, while the reactive power of Prosumer 1 decreased, as shown in Figs. 3.14 (b2-4). The reason why the reactive load was not shared equally by the three prosumers is that the system frequency is also coupled with the reactive power flow due to the resistive network characteristic. When the active power change resulted in the frequency deviation, reactive power flow was also reallocated to keep the global power balance. As the new-added load was located at N_3, the reactive power was mostly supplied by Prosumer 2 due to the proximity.

- The system frequency and the voltage peak, on the other hand, both experienced a sudden decrease immediately after the load change, followed by slight recovering back until reaching the new steady state. As both the active and reactive load power increased, the steady-state frequency and voltage magnitude both deviated as a result of the $v_{\mathrm{dc}}/i_{\mathrm{bat}}$ and Q/V droop.

18-24s: During the final period, Prosumer 1 was disconnected, resulting in a loss of generation. The lost power supply had to be compensated by Prosumer 2 and 3. Both active and reactive power output were increased in these two prosumers (see Figs. 3.14 (a3, 4), (b3, 4)). Essentially, this generation loss can be regarded as a sudden load increase in active and reactive power for these two prosumers. As a result, the system frequency and the voltage magnitude both dropped significantly.

Additionally, it can be seen from Figs. 3.14 (c1-4) that the variation in the DC-link voltage and the frequency are highly correlated. This is because of the equivalence between the two variables as a result of the matching control. In addition, from Figs. 3.14 (d1-3), the power from PV panels are kept as $0.8\,\mathrm{kW}$ each without notable changes during the transient state. Hence, PVs connected in parallel with the DC-link capacitors can be considered as constant power sources (in short term) without influencing the system behavior. Also, note that in Fig. 3.14, some high frequency oscillations can be observed in the DC voltages and PV powers. This is caused by the "P&O" MPPT algorithm which is applied in this simulation. A relatively larger oscillation can be seen in Prosumer 1 after $18\,\mathrm{s}$ when Prosumer 1 is disconnected. Its PV power goes to charge the battery. In this case, the voltage droop no longer serves as the power sharing method. Instead, it only serves as a proportional gain of the DC voltage error. Such oscillation can be reduced by choosing a smaller gain. According to the partitioned matrix results, it is clear that the network exhibits a reasonable power sharing, fast frequency and voltage regulation.

3.5 Summary

This chapter first discusses the grid-forming strategies which are applied in this thesis: the P/Q droop control and the matching control. Then the low-level voltage-current cascaded control loops are explained, which can be widely used to track the desired voltage reference provided by the grid-forming approaches. When matching control is applied, the voltage reference can also be tracked with a simple PI controller for the voltage magnitude instead of applying the cascaded voltage-current loop.

In terms of single-phase prosumers, the voltage reference can be tracked by the voltage-current cascaded control loops either by PR controllers when the reference is sinusoidal or the conventional PI controllers when AC variables are transformed into dq0 frame. To apply the dq0 frame in single-phase prosumer control, a fictitious quadrature signal is created based on the single-phase voltage/current, so the control structure of the cascaded loops are the same with that of three-phase prosumers.

With regards to the DC side of the prosumer, the chapter considers a hybrid configuration where a solar PV is connected in parallel with a battery storage, each connected via their individual DC-stage converters. Control of the two DC-stage converters are discussed then, with the BDC regulating the DC-link voltage and the unidirectional DC/DC converter conducting MPPT for PVs.

Finally, the chapter proposed a control strategy for hybrid PV-battery systems to support islanded operation of a residential LV distribution network based on matching and droop control. A PV-battery system is interfaced to the grid by a single hybrid inverter, which enables both MPPT and grid-forming functionality. P/f ($v_{\mathrm{dc}}/i_{\mathrm{bat}}$) and Q/V droop control are adopted to mimic the behavior of synchronous generators. A power compensation feed-forward term is additionally applied to the DC-link capacitor to ensure a fast response from the DC side. Simulations were carried out to test the performance of such control strategy using a residential LV network as a simulation test bed. Simulation results reveal that: 1) the system features fast response to the load change; 2) active loads are equally shared by all the generation units in the system; 3) reactive loads are predominantly supplied locally by the generation units located close to the loads; 4) the system frequency and the voltage magnitude respond to the change of load as a result of droop control; 5) the reactive power is coupled with the frequency deviation as a result of the non-negligible resistance on the transmission lines; 6) the frequency response is correlated with the DC-link voltage regulation due to the matching approach.

According to this chapter, it is feasible to run residential prosumers as grid-forming generation sources to form a residential microgrid. In particular, on the DC side, the PV can be considered as a constant power source injecting power to the system, while the battery storage performs frequency regulation. Therefore, when considering the dynamic response of such residential microgrids, the influence of PVs can be neglected. As discussed in Chapter 1, the residential microgrid is formed to improve the resiliency of the LV feeder network. In this case, it should be ensured that the microgrid maintains a stable operation when the feeder is abruptly separated from the main grid. This requires a stability study of the microgrid focusing on the dynamics immediately after the network separation, which is to be discussed in the next chapter.

Chapter 4

Stability Analysis of Low-voltage Distribution Feeders operated as Islanded Residential Microgrids

Residential microgrids, LV distribution feeders supplied by grid-forming prosumers, can smoothly transition from a grid-connected to an islanded mode, by which the resiliency is improved because network separation will not cause power outage. To ensure reliable operation of such a residential microgrid, it is necessary to study the transient stability during the mode transition and its small-signal stability after the network separation. Against this backdrop, this chapter discusses the stability analysis of the residential microgrid by explicitly modeling the grid-forming prosumers. As explained in Chapter 3, a grid-forming inverter is controlled by a cascaded structure, including the power droop controller, the outer-loop voltage controller and the inner-loop current controller. Linearised state-space modelling of AC microgrids with grid-forming inverters has been widely reported in [27, 81, 84, 95]. Stability information is acquired by the eigenvalues of the state matrix. Special attention should be paid to the dominant eigenvalues (defined as several eigenvalues located closest to the imaginary axis). Among these dominant eigenvalues, there is one critical eigenvalue which has the largest real part (for example, in a system where all eigenvalues are located on the left side of the imaginary axis, the critical eigenvalue is the one whose real part has the smallest absolute value). This critical eigenvalue contributes most to the system stability. Hence, stability analysis often studies the trajectory of the critical eigenvalue with regards to some specific parameters such as controller gains [7, 81, 160].

This chapter focuses on the stability analysis of residential microgrids. It has been reported that droop gains of the power controller are usually the main source of instability [7, 27, 75, 81, 95–97], showing that a large droop gain can cause instability by several certain pairs of complex-conjugate dominant eigenvalues. Published work has described how these dominant eigenvalues move to the unstable region with increase in the droop gains [75, 81, 97, 161]. Cases in these works are often small-size networks whose critical eigenvalue is mostly a pair of complex-conjugate eigenvalues. However, in a residential microgrid which contains a large number of prosumer-owned inverters, the system critical eigenvalue gradually turns into a real eigenvalue with the increasing number of the grid-forming inverters (called *microgrid expansion* henceforth), which will be shown in this chapter. This real eigenvalue is predominantly sensitive to the microgrid expansion. Droop gains would also have impact on this real eigenvalue but in the opposite way, pushing it away from the imaginary axis as they increase.

Additionally, the DC-side source of a grid-forming inverter is often considered as a constant voltage source [81, 97, 161, 162]. Based on that, the DC-side dynamics is neglected. However, in the aforementioned residential microgrid, DC-side primary sources are the residential ESS with various voltage levels and different dynamic responses. As a result, the DC-side dynamics should be considered in the following aspects: 1) DC converters used to interface primary sources with inverters. The dynamics of the DC converter and its controller should be explicitly modelled for the stability analysis. Authors in [82] included the DC dynamics in the small-signal model. However, only the dynamics of the DC-link capacitor is taken into consideration. [83] improved the microgrid model by including the model of the DC converter between the DC source and the inverter. The double-looped DC voltage controller is also included in the linearised model. However, the influence of the control parameters on the system stability were not studied; 2) the dynamic response of the primary sources. Compensated power is expected to be supplied from the grid-forming inverters quickly and sufficiently. However, some primary sources such as micro-turbines and fuel cells cannot provide instantaneous power due to their limited dynamic performance for load tracking [184]. Dynamic response of fast ESS such as batteries also varies between different technologies [185]. Generally, the dynamic response from primary sources can be modelled as a first-order lag transfer function [84], [186]. As slow primary response results in the discharge of the DC-link capacitor and consequently the output voltage, the time constant from the primary source should also be considered in the small-signal stability analysis.

To fill this gap, this chapter extends the work [160] by using a detailed model of grid-forming inverters to analyze the impact of the number of inverters in a string topology on microgrid small-signal stability. After that, the configuration of the DC side circuit is explicitly modelled, while it was typically represented by an ideal voltage source in the existing literature [81, 97, 161, 162]. As shown later, the DC dynamics, especially the dynamic response from primary DC energy sources has a significant impact on stability, so it needs to be included. In fact, some distributed generation technologies, such as micro-turbines and fuel cells, have namely a limited dynamic response, preventing them from providing instantaneous power [184]. Some battery chemistries, e.g. flow batteries, have the same problem [185].

The rest of the chapter is organized as follows: Section 4.1 gives the microgrid modelling. Stability analysis of the models is carried out in Section 4.2. Then in Section 4.3, simulation results of different cases are provided along with the results from the small-signal state-space models, showing the feasibility of the network operation and the accuracy of the derived small-signal models. Finally in Section 4.4, the modelling of single-phase prosumers is discussed for the sake of considering a more realistic residential microgrid case, along with time-domain simulations for model validations.

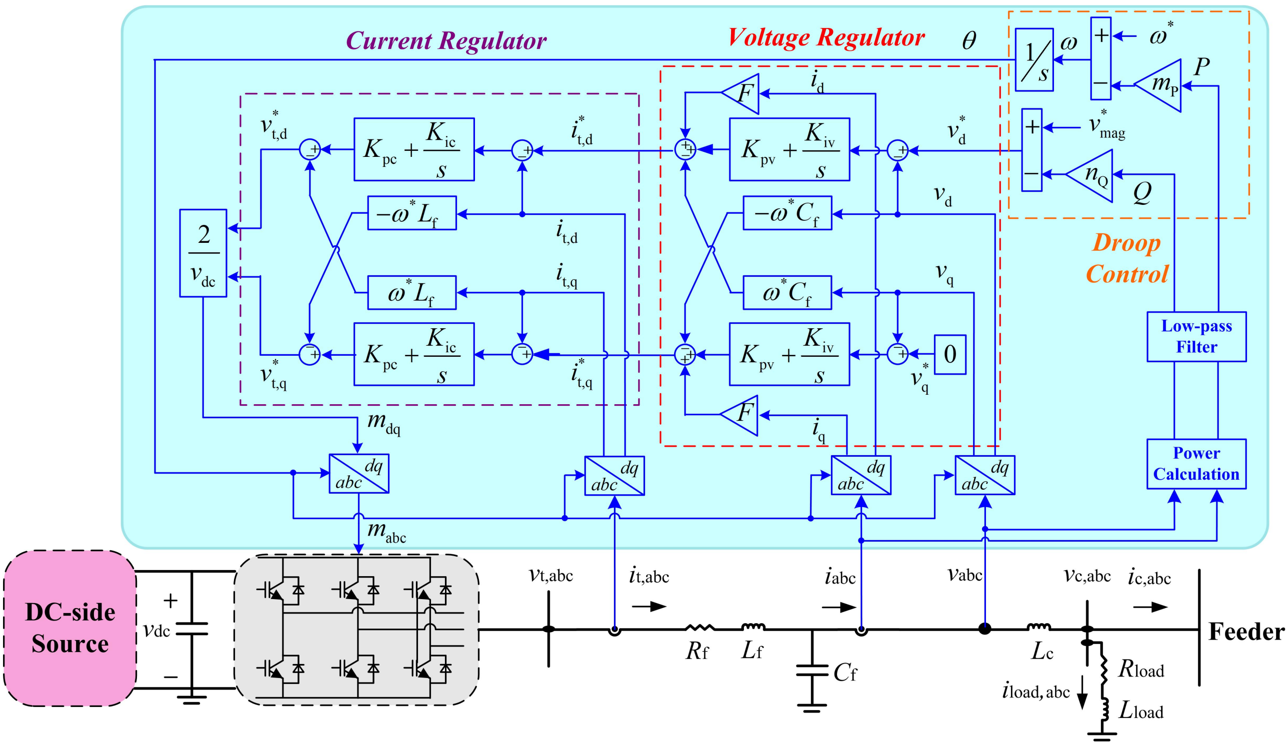

Figure 4.1: Block diagram of an individual prosumer.

4.1 Microgrid modelling

The microgrid model used in this chapter, illustrated in Fig. 4.1, is based on [81]. It includes detailed models of the inverter controller, the output filter, residential loads, the LV feeder and the DC side energy source with associated controls. The droop controller is used to ensure load sharing, and the cascaded voltage-current controller ensures that the output voltage of the inverter tracks the desired reference. The *LCL* filter is used to reject the high-frequency harmonics and smooth out the current injected into the system. We assume a constant impedance load to represent the load dynamics. When studying the impact of the microgrid expansion on stability, we model the DC side source in Fig. 4.1 as a constant DC voltage source; when we focus on the impact of the DC side dynamics, we model it by considering the DC converter and primary energy sources' response time. State variables of an individual prosumer are modelled on its own reference frame whose rotation frequency is set by its local droop controller. When combining the models of all prosumers, all variables are translated to a common reference frame as follows:

$$\boldsymbol{f}_{\mathrm{DQ},i} = \begin{bmatrix} \cos\delta_i & -\sin\delta_i \\ \sin\delta_i & \cos\delta_i \end{bmatrix} \boldsymbol{f}_{\mathrm{dq},i}, \tag{4.1}$$

where $\boldsymbol{f}_{\mathrm{DQ},i}$ and $\boldsymbol{f}_{\mathrm{dq},i}$ are the state variables of the ith prosumer in the common frame and individual frame, respectively. δ_i is the angle shift between the ith prosumer's reference frame and the common reference frame, whose state equation is given as

$$\dot{\delta}_i = \omega_i - \omega_{\mathrm{com}}, \tag{4.2}$$

where ω_i and ω_{com} are rotating frequencies of the ith reference frame and common reference frame, respectively.

4.1.1 Individual inverter AC dynamics

Modelling of the AC dynamics of an individual prosumer considers the modelling of the inverter controller, the output filter and the residential load. The meaning of parameters can be found in Fig. 4.1 not explicitly explained in the text. Subscript t and c denote, respectively, the inverter terminal and the point of connection to the feeder (see Fig. 4.1).

Droop control

Load sharing is exhibited by adjusting the output frequency and voltage magnitude. The frequency and voltage droop characteristics can be expressed as follows

$$\omega = \omega^* - m_{\mathrm{P}} P, \tag{4.3a}$$

$$v_{\mathrm{d}}^* = v_{\mathrm{mag}}^* - n_{\mathrm{Q}} Q, \qquad v_{\mathrm{q}}^* = 0, \tag{4.3b}$$

$$P = \frac{\omega_{\mathrm{f}}}{s+\omega_{\mathrm{f}}} \cdot \frac{3}{2}(v_{\mathrm{d}} i_{\mathrm{d}} + v_{\mathrm{q}} i_{\mathrm{q}}), \tag{4.3c}$$

$$Q = \frac{\omega_{\mathrm{f}}}{s+\omega_{\mathrm{f}}} \cdot \frac{3}{2}(v_{\mathrm{q}} i_{\mathrm{d}} - v_{\mathrm{d}} i_{\mathrm{q}}), \tag{4.3d}$$

where P and Q are the filtered active and reactive powers. ω_{f} is the cut-off frequency of the low-pass filter. The linearised differential equations of power sharing controller are as follows:

$$\dot{\begin{bmatrix} \Delta\delta \\ \Delta P \\ \Delta Q \end{bmatrix}} = A_{\mathrm{P}} \begin{bmatrix} \Delta\delta \\ \Delta P \\ \Delta Q \end{bmatrix} + B_{\mathrm{P}} \begin{bmatrix} \Delta \boldsymbol{i}_{\mathrm{t,dq}} \\ \Delta \boldsymbol{v}_{\mathrm{dq}} \\ \Delta \boldsymbol{i}_{\mathrm{dq}} \\ \Delta \boldsymbol{i}_{\mathrm{load,dq}} \end{bmatrix} + B_{\mathrm{P\omega com}} \Delta\omega_{\mathrm{com}}, \tag{4.4a}$$

$$\begin{bmatrix} \Delta\omega \\ \Delta v_{\mathrm{dq}}^* \end{bmatrix} = \begin{bmatrix} C_{\mathrm{P\omega}} \\ C_{\mathrm{Pv}} \end{bmatrix} \begin{bmatrix} \Delta\delta \\ \Delta P \\ \Delta Q \end{bmatrix}, \tag{4.4b}$$

where

$$A_{\mathrm{P}} = \begin{bmatrix} 0 & -m_{\mathrm{P}} & 0 \\ 0 & -\omega_{\mathrm{f}} & 0 \\ 0 & 0 & -\omega_{\mathrm{f}} \end{bmatrix}, B_{\mathrm{P}} = \frac{3}{2}\omega_{\mathrm{f}} \cdot \begin{bmatrix} 0 & 0 & 0 & 0 & 0 & 0 & 0 & 0 \\ 0 & 0 & I_{\mathrm{d}} & I_{\mathrm{q}} & V_{\mathrm{d}} & V_{\mathrm{q}} & 0 & 0 \\ 0 & 0 & -I_{\mathrm{q}} & I_{\mathrm{d}} & V_{\mathrm{q}} & -V_{\mathrm{d}} & 0 & 0 \end{bmatrix}, B_{\mathrm{P\omega com}} = \begin{bmatrix} -1 \\ 0 \\ 0 \end{bmatrix},$$

$$C_{\mathrm{P\omega}} = \begin{bmatrix} 0, -m_{\mathrm{P}}, 0 \end{bmatrix}, C_{\mathrm{Pv}} = \begin{bmatrix} 0 & 0 & -n_{\mathrm{Q}} \\ 0 & 0 & 0 \end{bmatrix}.$$

$\Delta\omega$ and $\Delta\omega_{\mathrm{com}}$ are small-signal variations of the rotating frequency of the individual reference frame and common reference frame, respectively. $\Delta\delta$ is the small-signal variation of the angle shift between the individual reference frame and the common reference frame. V_{d}, V_{q}, I_{d}, and I_{q} are steady-state operating values.

Voltage regulator

Define the integral of voltage errors in d and q directions as $\boldsymbol{\psi}_{\mathrm{dq}}$. The state equations in the voltage loop are

$$\frac{d\psi_{\mathrm{d}}}{dt} = v_{\mathrm{d}}^{*} - v_{\mathrm{d}}, \qquad \frac{d\psi_{\mathrm{q}}}{dt} = v_{\mathrm{q}}^{*} - v_{\mathrm{q}}, \tag{4.5}$$

along with the algebraic equations

$$i_{\mathrm{t,d}}^{*} = K_{\mathrm{pv}}(v_{\mathrm{d}}^{*} - v_{\mathrm{d}}) + K_{\mathrm{iv}}\psi_{\mathrm{d}} - \omega^{*}C_{\mathrm{f}}v_{\mathrm{q}} + Fi_{\mathrm{d}}, \tag{4.6a}$$

$$i_{\mathrm{t,q}}^{*} = K_{\mathrm{pv}}(v_{\mathrm{q}}^{*} - v_{\mathrm{q}}) + K_{\mathrm{iv}}\psi_{\mathrm{q}} + \omega^{*}C_{\mathrm{f}}v_{\mathrm{d}} + Fi_{\mathrm{q}}. \tag{4.6b}$$

Hence, the linearised state-space small-signal model of the voltage regulator is

$$\left[\Delta\dot{\boldsymbol{\psi}}_{\mathrm{dq}}\right] = B_{\mathrm{v1}}\left[\Delta\boldsymbol{v}_{\mathrm{dq}}^{*}\right] + B_{\mathrm{v2}}\begin{bmatrix}\Delta\boldsymbol{i}_{\mathrm{t,dq}}\\ \Delta\boldsymbol{v}_{\mathrm{dq}}\\ \Delta\boldsymbol{i}_{\mathrm{dq}}\\ \Delta\boldsymbol{i}_{\mathrm{load,dq}}\end{bmatrix}, \tag{4.7a}$$

$$\left[\Delta\boldsymbol{i}_{\mathrm{t,dq}}^{*}\right] = C_{\mathrm{v}}\left[\Delta\boldsymbol{\psi}_{\mathrm{dq}}\right] + D_{\mathrm{v1}}\left[\Delta\boldsymbol{v}_{\mathrm{dq}}^{*}\right] + D_{\mathrm{v2}}\begin{bmatrix}\Delta\boldsymbol{i}_{\mathrm{t,dq}}\\ \Delta\boldsymbol{v}_{\mathrm{dq}}\\ \Delta\boldsymbol{i}_{\mathrm{dq}}\\ \Delta\boldsymbol{i}_{\mathrm{load,dq}}\end{bmatrix}, \tag{4.7b}$$

where
$B_{\mathrm{v1}} = \begin{bmatrix}1 & 0\\ 0 & 1\end{bmatrix}$, $B_{\mathrm{v2}} = \begin{bmatrix}0 & 0 & -1 & 0 & 0 & 0 & 0 & 0\\ 0 & 0 & 0 & -1 & 0 & 0 & 0 & 0\end{bmatrix}$, $C_{\mathrm{v}} = \begin{bmatrix}K_{\mathrm{iv}} & 0\\ 0 & K_{\mathrm{iv}}\end{bmatrix}$, $D_{\mathrm{v1}} = \begin{bmatrix}K_{\mathrm{pv}} & 0\\ 0 & K_{\mathrm{pv}}\end{bmatrix}$,
$D_{\mathrm{v2}} = \begin{bmatrix}0 & 0 & -K_{\mathrm{pv}} & -\omega^{*}C_{\mathrm{f}} & F & 0 & 0 & 0\\ 0 & 0 & \omega^{*}C_{\mathrm{f}} & -K_{\mathrm{pv}} & 0 & F & 0 & 0\end{bmatrix}$.

Current regulator

Define the integral of current errors in d and q directions as $\boldsymbol{\gamma}_{\mathrm{dq}}$. The corresponding state equations are

$$\frac{d\gamma_{\mathrm{d}}}{dt} = i_{\mathrm{t,d}}^{*} - i_{\mathrm{t,d}}, \qquad \frac{d\gamma_{\mathrm{q}}}{dt} = i_{\mathrm{t,q}}^{*} - i_{\mathrm{t,q}}, \tag{4.8}$$

along with the algebraic equations

$$v_{\mathrm{t,d}}^{*} = K_{\mathrm{pc}}(i_{\mathrm{t,d}}^{*} - i_{\mathrm{t,d}}) + K_{\mathrm{ic}}\gamma_{\mathrm{d}} - \omega^{*}L_{\mathrm{f}}i_{\mathrm{t,q}} + v_{\mathrm{d}}, \tag{4.9a}$$

$$v_{\mathrm{t,q}}^{*} = K_{\mathrm{pc}}(i_{\mathrm{t,q}}^{*} - i_{\mathrm{t,q}}) + K_{\mathrm{ic}}\gamma_{\mathrm{q}} + \omega^{*}L_{\mathrm{f}}i_{\mathrm{t,d}} + v_{\mathrm{q}}. \tag{4.9b}$$

Hence, the linearised state-space small-signal model of the current regulator is

$$\left[\Delta\dot{\boldsymbol{\gamma}}_{\mathrm{dq}}\right] = B_{\mathrm{c1}}\left[\Delta\boldsymbol{i}^*_{\mathrm{t,dq}}\right] + B_{\mathrm{c2}}\begin{bmatrix}\Delta\boldsymbol{i}_{\mathrm{t,dq}}\\ \Delta\boldsymbol{v}_{\mathrm{dq}}\\ \Delta\boldsymbol{i}_{\mathrm{dq}}\\ \Delta\boldsymbol{i}_{\mathrm{load,dq}}\end{bmatrix}, \tag{4.10a}$$

$$\left[\Delta\boldsymbol{v}^*_{\mathrm{t,dq}}\right] = C_{\mathrm{c}}\left[\Delta\boldsymbol{\gamma}_{\mathrm{dq}}\right] + D_{\mathrm{c1}}\left[\Delta\boldsymbol{i}^*_{\mathrm{t,dq}}\right] + D_{\mathrm{c2}}\begin{bmatrix}\Delta\boldsymbol{i}_{\mathrm{t,dq}}\\ \Delta\boldsymbol{v}_{\mathrm{dq}}\\ \Delta\boldsymbol{i}_{\mathrm{dq}}\\ \Delta\boldsymbol{i}_{\mathrm{load,dq}}\end{bmatrix}, \tag{4.10b}$$

where
$B_{\mathrm{c1}} = \begin{bmatrix}1 & 0\\ 0 & 1\end{bmatrix}$, $B_{\mathrm{c2}} = \begin{bmatrix}-1 & 0 & 0 & 0 & 0 & 0 & 0 & 0\\ 0 & -1 & 0 & 0 & 0 & 0 & 0 & 0\end{bmatrix}$, $C_{\mathrm{c}} = \begin{bmatrix}K_{\mathrm{ic}} & 0\\ 0 & K_{\mathrm{ic}}\end{bmatrix}$, $D_{\mathrm{c1}} = \begin{bmatrix}K_{\mathrm{pc}} & 0\\ 0 & K_{\mathrm{pc}}\end{bmatrix}$,
$D_{\mathrm{c2}} = \begin{bmatrix}-K_{\mathrm{pc}} & -\omega^* L_{\mathrm{f}} & 0 & 0 & 0 & 0 & 0 & 0\\ \omega^* L_{\mathrm{f}} & -K_{\mathrm{pc}} & 0 & 0 & 0 & 0 & 0 & 0\end{bmatrix}$.

Output filter and individual load

Output filter and the local load small-signal model can be represented by assuming that the inverter produces the desired voltages ($v^*_{\mathrm{t,dq}} = v_{\mathrm{t,dq}}$):

$$\frac{di_{\mathrm{t,d}}}{dt} = \frac{1}{L_{\mathrm{f}}}v_{\mathrm{t,d}} - \frac{1}{L_{\mathrm{f}}}v_{\mathrm{d}} - \frac{R_{\mathrm{f}}}{L_{\mathrm{f}}}i_{\mathrm{t,d}} + \omega i_{\mathrm{t,q}}, \tag{4.11a}$$
$$\frac{di_{\mathrm{t,q}}}{dt} = \frac{1}{L_{\mathrm{f}}}v_{\mathrm{t,q}} - \frac{1}{L_{\mathrm{f}}}v_{\mathrm{q}} - \frac{R_{\mathrm{f}}}{L_{\mathrm{f}}}i_{\mathrm{t,q}} - \omega i_{\mathrm{t,d}}, \tag{4.11b}$$
$$\frac{dv_{\mathrm{d}}}{dt} = \frac{1}{C_{\mathrm{f}}}i_{\mathrm{t,d}} - \frac{1}{C_{\mathrm{f}}}i_{\mathrm{d}} + \omega v_{\mathrm{q}}, \tag{4.11c}$$
$$\frac{dv_{\mathrm{q}}}{dt} = \frac{1}{C_{\mathrm{f}}}i_{\mathrm{t,q}} - \frac{1}{C_{\mathrm{f}}}i_{\mathrm{q}} - \omega v_{\mathrm{d}}, \tag{4.11d}$$
$$\frac{di_{\mathrm{d}}}{dt} = \frac{1}{L_{\mathrm{c}}}v_{\mathrm{d}} - \frac{1}{L_{\mathrm{c}}}v_{\mathrm{c,d}} + \omega i_{\mathrm{q}}, \tag{4.11e}$$
$$\frac{di_{\mathrm{q}}}{dt} = \frac{1}{L_{\mathrm{c}}}v_{\mathrm{q}} - \frac{1}{L_{\mathrm{c}}}v_{\mathrm{c,q}} - \omega i_{\mathrm{d}}, \tag{4.11f}$$
$$\frac{di_{\mathrm{load,d}}}{dt} = \frac{1}{L_{\mathrm{load}}}v_{\mathrm{c,d}} - \frac{R_{\mathrm{load}}}{L_{\mathrm{load}}}i_{\mathrm{load,d}} + \omega i_{\mathrm{load,q}}, \tag{4.11g}$$
$$\frac{di_{\mathrm{load,q}}}{dt} = \frac{1}{L_{\mathrm{load}}}v_{\mathrm{c,q}} - \frac{R_{\mathrm{load}}}{L_{\mathrm{load}}}i_{\mathrm{load,q}} - \omega i_{\mathrm{load,d}}. \tag{4.11h}$$

Hence, the the linearised state-space small-signal model of the output interfaced part is

$$\begin{bmatrix}\Delta\dot{\boldsymbol{i}}_{\mathrm{t,dq}}\\ \Delta\boldsymbol{v}_{\mathrm{dq}}\\ \Delta\boldsymbol{i}_{\mathrm{dq}}\\ \Delta\boldsymbol{i}_{\mathrm{load,dq}}\end{bmatrix} = A_{\mathrm{LCLL}}\begin{bmatrix}\Delta\boldsymbol{i}_{\mathrm{t,dq}}\\ \Delta\boldsymbol{v}_{\mathrm{dq}}\\ \Delta\boldsymbol{i}_{\mathrm{dq}}\\ \Delta\boldsymbol{i}_{\mathrm{load,dq}}\end{bmatrix} + B_{\mathrm{1LCLL}}\Delta\boldsymbol{v}_{\mathrm{t,dq}} + B_{\mathrm{2LCLL}}\Delta\boldsymbol{v}_{\mathrm{c,dq}} + B_{\mathrm{3LCLL}}\Delta\omega, \tag{4.12}$$

where

$$A_{\mathrm{LCLL}} = \begin{bmatrix} -\frac{R_\mathrm{f}}{L_\mathrm{f}} & \omega_0 & -\frac{1}{L_\mathrm{f}} & 0 & 0_{1\times2} & & 0_{1\times2} \\ -\omega_0 & -\frac{R_\mathrm{f}}{L_\mathrm{f}} & 0 & -\frac{1}{L_\mathrm{f}} & 0_{1\times2} & & 0_{1\times2} \\ \frac{1}{C_\mathrm{f}} & 0 & 0 & \omega_0 & -\frac{1}{C_\mathrm{f}} & 0 & 0_{1\times2} \\ 0 & \frac{1}{C_\mathrm{f}} & -\omega_0 & 0 & 0 & -\frac{1}{C_\mathrm{f}} & 0_{1\times2} \\ 0_{1\times2} & & \frac{1}{L_\mathrm{c}} & 0 & 0 & \omega_0 & 0_{1\times2} \\ 0_{1\times2} & & 0 & \frac{1}{L_\mathrm{c}} & -\omega_0 & 0 & 0_{1\times2} \\ 0_{1\times2} & & 0_{1\times2} & & 0_{1\times2} & -\frac{R_\mathrm{load}}{L_\mathrm{load}} & \omega_0 \\ 0_{1\times2} & & 0_{1\times2} & & 0_{1\times2} & -\omega_0 & -\frac{R_\mathrm{load}}{L_\mathrm{load}} \end{bmatrix}, B_{\mathrm{1LCLL}} = \begin{bmatrix} \frac{1}{L_\mathrm{f}} & 0 \\ 0 & \frac{1}{L_\mathrm{f}} \\ 0_{6\times2} & \end{bmatrix},$$

$$B_{\mathrm{2LCLL}} = \begin{bmatrix} 0_{4\times2} & \\ -\frac{1}{L_\mathrm{c}} & 0 \\ 0 & -\frac{1}{L_\mathrm{c}} \\ \frac{1}{L_\mathrm{load}} & 0 \\ 0 & \frac{1}{L_\mathrm{load}} \end{bmatrix}, B_{\mathrm{3LCLL}} = \begin{bmatrix} I_{\mathrm{t,q}} & -I_{\mathrm{t,d}} & V_\mathrm{q} & -V_\mathrm{d} & I_\mathrm{q} & -I_\mathrm{d} & I_{\mathrm{load,q}} & -I_{\mathrm{load,d}} \end{bmatrix}^\top.$$

$I_{\mathrm{t,dq}}$, V_{dq}, I_{dq}, and $I_{\mathrm{load,dq}}$ are steady-state operating values.

Frame transformation

According to (4.12), the output and input variables of an inverter are the output currents $\Delta \boldsymbol{i}_{\mathrm{c,dq}}$ in individual reference frame and the node voltage $\Delta \boldsymbol{v}_{\mathrm{c,DQ}}$ in common reference frame, respectively. Using the transformation technique (4.1), the small-signal output current $\Delta \boldsymbol{i}_{\mathrm{c,DQ}}$ on the common reference frame and the node voltage $\Delta \boldsymbol{v}_{\mathrm{c,dq}}$ in the individual reference frame can be obtained, as in (4.13).

$$\Delta \boldsymbol{i}_{\mathrm{c,DQ}} = T_\mathrm{s} \Delta \boldsymbol{i}_{\mathrm{c,dq}} + T_\mathrm{c} \Delta \delta, \tag{4.13a}$$

$$\Delta \boldsymbol{v}_{\mathrm{c,dq}} = T_\mathrm{s}^{-1} \Delta \boldsymbol{v}_{\mathrm{c,DQ}} + T_\mathrm{v}^{-1} \Delta \delta, \tag{4.13b}$$

where

$$T_\mathrm{s} = \begin{bmatrix} \cos\delta_0 & -\sin\delta_0 \\ \sin\delta_0 & \cos\delta_0 \end{bmatrix}, T_\mathrm{c} = \begin{bmatrix} -I_{\mathrm{c,d}}\sin\delta_0 - I_{\mathrm{c,q}}\cos\delta_0 \\ I_{\mathrm{c,d}}\cos\delta_0 - I_{\mathrm{c,q}}\sin\delta_0 \end{bmatrix}, \text{and } T_\mathrm{v}^{-1} = \begin{bmatrix} -V_{\mathrm{c,D}}\sin\delta_0 + V_{\mathrm{c,Q}}\cos\delta_0 \\ -V_{\mathrm{c,D}}\cos\delta_0 - V_{\mathrm{c,Q}}\sin\delta_0 \end{bmatrix}.$$

$I_{\mathrm{c,dq}}$, $V_{\mathrm{c,DQ}}$ are steady-state operating values.

Individual inverter

Denote $\Delta \boldsymbol{x}_\mathrm{P} = \begin{bmatrix} \Delta\delta \\ \Delta P \\ \Delta Q \end{bmatrix}$, $\Delta \boldsymbol{x}_{\mathrm{LCLL}} = \begin{bmatrix} \Delta \boldsymbol{i}_{\mathrm{t,dq}} \\ \Delta \boldsymbol{v}_{\mathrm{dq}} \\ \Delta \boldsymbol{i}_{\mathrm{dq}} \\ \Delta \boldsymbol{i}_{\mathrm{load,dq}} \end{bmatrix}$. The linearised state-space small-signal model of an individual inverter is expressed as

$$\begin{bmatrix} \Delta \boldsymbol{x}_{\mathrm{P}} \\ \Delta \boldsymbol{\psi}_{\mathrm{dq}} \\ \Delta \boldsymbol{\gamma}_{\mathrm{dq}} \\ \Delta \boldsymbol{x}_{\mathrm{LCLL}} \end{bmatrix}^{\cdot} = A_{\mathrm{inv}} \begin{bmatrix} \Delta \boldsymbol{x}_{\mathrm{P}} \\ \Delta \boldsymbol{\psi}_{\mathrm{dq}} \\ \Delta \boldsymbol{\gamma}_{\mathrm{dq}} \\ \Delta \boldsymbol{x}_{\mathrm{LCLL}} \end{bmatrix} + B_{\mathrm{inv}} \Delta \boldsymbol{v}_{\mathrm{c,DQ}} + B_{\omega \mathrm{com}} \Delta \omega_{\mathrm{com}}, \tag{4.14}$$

where

$$A_{\mathrm{inv}} = \begin{bmatrix} A_{\mathrm{P}} & 0_{3\times 2} & 0_{3\times 2} & B_{\mathrm{P}} \\ B_{\mathrm{v1}} C_{\mathrm{Pv}} & 0_{2\times 2} & 0_{2\times 2} & B_{\mathrm{v2}} \\ B_{\mathrm{c1}} D_{\mathrm{v1}} C_{\mathrm{Pv}} & B_{\mathrm{c1}} C_{\mathrm{v}} & 0_{2\times 2} & B_{\mathrm{c1}} D_{\mathrm{v2}} + B_{\mathrm{c2}} \\ B_{\mathrm{1LCLL}} D_{\mathrm{c1}} D_{\mathrm{v1}} C_{\mathrm{Pv}} & & & A_{\mathrm{LCLL}} \\ +B_{\mathrm{2LCLL}} \begin{bmatrix} T_{\mathrm{v}}^{-1} & 0_{2\times 1} & 0_{2\times 1} \end{bmatrix} & B_{\mathrm{1LCLL}} D_{\mathrm{c1}} C_{\mathrm{v}} & B_{\mathrm{1LCLL}} C_{\mathrm{c}} & +B_{\mathrm{1LCLL}} D_{\mathrm{c1}} D_{\mathrm{v2}} \\ +B_{\mathrm{3LCLL}} C_{\mathrm{P}\omega} & & & +B_{\mathrm{1LCLL}} D_{\mathrm{c2}} \end{bmatrix},$$

$$B_{\mathrm{inv}} = \begin{bmatrix} 0_{7\times 2} \\ B_{\mathrm{2LCLL}} T_{\mathrm{s}}^{-1} \end{bmatrix}, B_{\omega \mathrm{com}} = \begin{bmatrix} B_{\mathrm{P}\omega \mathrm{com}} \\ 0_{12\times 1} \end{bmatrix}.$$

So the state variables of an individual prosumer is expressed as
$\Delta \boldsymbol{x}_{\mathrm{inv}} = \begin{bmatrix} \Delta \boldsymbol{x}_{\mathrm{P}}^{\top} & \Delta \boldsymbol{\psi}_{\mathrm{dq}}^{\top} & \Delta \boldsymbol{\gamma}_{\mathrm{dq}}^{\top} & \Delta \boldsymbol{x}_{\mathrm{LCLL}}^{\top} \end{bmatrix}^{\top}$.

Common reference frame

To combine all inverters together, a common frame of the whole system should be selected. Assume the system contains n inverters. These inverters are labelled as Inverter i where $i = 1, 2, 3, ...n$. Select the frame of Inverter 1 as the common frame, which means $\Delta\omega_{\mathrm{com}}$ is selected as $\Delta\omega_1$.

$$\Delta\omega_{\mathrm{com}} = \Delta\omega_1 = C_{\omega \mathrm{com}} \Delta \boldsymbol{x}_{\mathrm{inv},1}, \tag{4.15}$$

where $C_{\omega \mathrm{com}} = \begin{bmatrix} C_{\mathrm{P}\omega,1} & 0_{1\times 12} \end{bmatrix}$.

Based on this selection, the state-space model of each individual inverter is expressed as

$$\Delta \dot{\boldsymbol{x}}_{\mathrm{inv},i} = A_{\mathrm{inv},i} \Delta \boldsymbol{x}_{\mathrm{inv},i} + B_{\mathrm{inv},i} \Delta \boldsymbol{v}_{\mathrm{c,DQ},i} + B_{\omega \mathrm{com}} C_{\omega \mathrm{com}} \Delta \boldsymbol{x}_{\mathrm{inv},1}, \tag{4.16a}$$

$$\Delta \dot{\boldsymbol{i}}_{\mathrm{c,DQ},i} = C_{\mathrm{invc},i} \Delta \boldsymbol{x}_{\mathrm{inv},i}, \tag{4.16b}$$

where $C_{\mathrm{invc},i} = \begin{bmatrix} T_{\mathrm{c},i} & 0_{2\times 10} & T_{\mathrm{s},i} & -T_{\mathrm{s},i} \end{bmatrix}$.

After combining all inverters together, a combined small-signal model of all the inverter units together is obtained, as shown in

$$\Delta \dot{\boldsymbol{x}}_{\mathrm{INV}} = A_{\mathrm{INV}} \Delta \boldsymbol{x}_{\mathrm{INV}} + B_{\mathrm{INV}} \Delta \boldsymbol{v}_{\mathrm{C,DQ}}, \tag{4.17a}$$

$$\Delta \boldsymbol{i}_{\mathrm{C,DQ}} = C_{\mathrm{INVC}} \Delta \boldsymbol{x}_{\mathrm{INV}}, \tag{4.17b}$$

where
$\Delta \boldsymbol{x}_{\mathrm{INV}} = \begin{bmatrix} \Delta \boldsymbol{x}_{\mathrm{inv},1}^{\top} & \Delta \boldsymbol{x}_{\mathrm{inv},2}^{\top} & \Delta \boldsymbol{x}_{\mathrm{inv},3}^{\top} & \ldots & \Delta \boldsymbol{x}_{\mathrm{inv},n}^{\top} \end{bmatrix}^{\top}$,

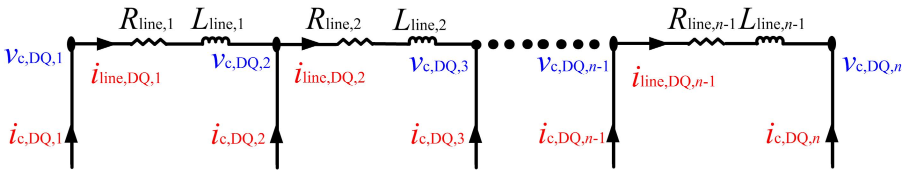

Figure 4.2: Single-line diagram of the LV feeder.

$$\Delta \boldsymbol{v}_{\text{C,DQ}} = \begin{bmatrix} \Delta \boldsymbol{v}_{\text{c,DQ,1}}^{\top} & \Delta \boldsymbol{v}_{\text{c,DQ,2}}^{\top} & \Delta \boldsymbol{v}_{\text{c,DQ,3}}^{\top} & \dots & \Delta \boldsymbol{v}_{\text{c,DQ},n}^{\top} \end{bmatrix}^{\top},$$

$$\Delta \boldsymbol{i}_{\text{C,DQ}} = \begin{bmatrix} \Delta \boldsymbol{i}_{\text{c,DQ,1}}^{\top} & \Delta \boldsymbol{i}_{\text{c,DQ,2}}^{\top} & \Delta \boldsymbol{i}_{\text{c,DQ,3}}^{\top} & \dots & \Delta \boldsymbol{i}_{\text{c,DQ},n}^{\top} \end{bmatrix}^{\top},$$

$$A_{\text{INV}} = \begin{bmatrix} A_{\text{inv,1}} + B_{\omega\text{com}} C_{\omega\text{com}} & 0 & 0 & .. & 0 \\ B_{\omega\text{com}} C_{\omega\text{com}} & A_{\text{inv,2}} & 0 & .. & 0 \\ B_{\omega\text{com}} C_{\omega\text{com}} & 0 & A_{\text{inv,3}} & .. & 0 \\ \dots & \dots & \dots & .. & \dots \\ B_{\omega\text{com}} C_{\omega\text{com}} & 0 & 0 & .. & A_{\text{inv},n} \end{bmatrix}_{15n \times 15n},$$

$$B_{\text{INV}} = \begin{bmatrix} B_{\text{inv,1}} & 0 & 0 & \dots & 0 \\ 0 & B_{\text{inv,2}} & 0 & \dots & 0 \\ 0 & 0 & B_{\text{inv,3}} & \dots & 0 \\ \dots & \dots & \dots & \dots & \dots \\ 0 & 0 & 0 & \dots & B_{\text{inv},n} \end{bmatrix}_{15n \times 2n}, C_{\text{INVC}} = \begin{bmatrix} C_{\text{inv,1}} & 0 & 0 & \dots & 0 \\ 0 & C_{\text{inv,2}} & 0 & \dots & 0 \\ 0 & 0 & C_{\text{inv,3}} & \dots & 0 \\ \dots & \dots & \dots & \dots & \dots \\ 0 & 0 & 0 & \dots & C_{\text{inv},n} \end{bmatrix}_{2n \times 15n}.$$

4.1.2 State-space model of the LV feeder

Residential customers typically use a single-phase connection. However, because loads in LV feeders are distributed evenly across phases, it is reasonable to assume a balanced operation. Under this assumption, we can model the loads as three-phase, leading to the single-line diagram shown in Fig. 4.2. In a radial system with n prosumers, there are $n-1$ transmission lines, labelled as $j = 1, 2, 3, ..., n-1$. Transmission line dynamics is represented in the common reference frame by the state equations of the line currents as

$$\frac{di_{\text{line,D},j}}{dt} = \frac{1}{L_{\text{line},j}} v_{\text{c,D},j} - \frac{1}{L_{\text{line},j}} v_{\text{c,D},j+1} - \frac{R_{\text{line},j}}{L_{\text{line},j}} i_{\text{line,D},j} + \omega_{\text{com}} i_{\text{line,Q},j}, \tag{4.18a}$$

$$\frac{di_{\text{line,Q},j}}{dt} = \frac{1}{L_{\text{line},j}} v_{\text{c,Q},j} - \frac{1}{L_{\text{line},j}} v_{\text{c,Q},j+1} - \frac{R_{\text{line},j}}{L_{\text{line},j}} i_{\text{line,Q},j} - \omega_{\text{com}} i_{\text{line,D},j}. \tag{4.18b}$$

Hence, the linearised small-signal state-space model of the network is

$$\Delta \dot{\boldsymbol{i}}_{\text{line,DQ},j} = A_{\text{NET},j} \Delta \boldsymbol{i}_{\text{line,DQ},j} + B_{\text{2NET},j} \Delta \omega_{\text{com}} + \begin{bmatrix} B_{\text{1NET},j} & -B_{\text{1NET},j} \end{bmatrix} \begin{bmatrix} \Delta \boldsymbol{v}_{\text{c,DQ},j} \\ \Delta \boldsymbol{v}_{\text{c,DQ},j+1} \end{bmatrix}, \tag{4.19}$$

where $A_{\text{NET},j} = \begin{bmatrix} -\frac{R_{\text{line},j}}{L_{\text{line},j}} & \omega_{\text{com0}} \\ -\omega_{\text{com0}} & -\frac{R_{\text{line},j}}{L_{\text{line},j}} \end{bmatrix}$, $B_{\text{1NET},j} = \begin{bmatrix} \frac{1}{L_{\text{line},j}} & 0 \\ 0 & \frac{1}{L_{\text{line},j}} \end{bmatrix}$, $B_{\text{2NET},j} = \begin{bmatrix} I_{\text{line,Q},j} \\ -I_{\text{line,D},j} \end{bmatrix}$.

$I_{\text{line,DQ}}$ and ω_{com0} are steady-state operating values. Combine all transmission lines together in one state equation, as shown in

$$\Delta\dot{\boldsymbol{i}}_{\text{LINE,DQ}} = A_{\text{NET}}\Delta\boldsymbol{i}_{\text{LINE,DQ}} + B_{1\text{NET}}\Delta\boldsymbol{v}_{\text{C,DQ}} + B_{2\text{NET}}C_{\text{INV}\omega\text{com}}\Delta\boldsymbol{x}_{\text{INV}}, \tag{4.20}$$

where $\Delta\boldsymbol{i}_{\text{LINE,DQ}} = \begin{bmatrix}\Delta\boldsymbol{i}^{\top}_{\text{line,DQ,1}} & \Delta\boldsymbol{i}^{\top}_{\text{line,DQ,2}} & \dots & \Delta\boldsymbol{i}^{\top}_{\text{line,DQ},n-1}\end{bmatrix}^{\top}$,

$$A_{\text{NET}} = \begin{bmatrix} A_{\text{NET,1}} & 0 & 0 & \dots & 0 \\ 0 & A_{\text{NET,2}} & 0 & \dots & 0 \\ 0 & 0 & A_{\text{NET,3}} & \dots & 0 \\ \dots & \dots & \dots & \dots & \dots \\ 0 & 0 & 0 & \dots & A_{\text{NET},n-1} \end{bmatrix}_{2(n-1)\times 2(n-1)},$$

$$B_{1\text{NET}} = \begin{bmatrix} B_{1\text{NET,1}} & -B_{1\text{NET,1}} & 0 & \dots & 0 & 0 \\ 0 & B_{1\text{NET,2}} & -B_{1\text{NET,2}} & \dots & 0 & 0 \\ 0 & 0 & B_{1\text{NET,3}} & -B_{1\text{NET,3}} & 0 & 0 \\ \dots & \dots & \dots & \dots & \dots & \dots \\ 0 & 0 & 0 & \dots & B_{1\text{NET},n-1} & -B_{1\text{NET},n-1} \end{bmatrix}_{2(n-1)\times 2n},$$

$B_{2\text{NET}} = \begin{bmatrix} B^{\top}_{2\text{NET,1}} & B^{\top}_{2\text{NET,2}} & B^{\top}_{1\text{NET,3}} & \dots & B^{\top}_{2\text{NET},n-1}\end{bmatrix}^{\top}_{2(n-1)\times 1}$, and $C_{\text{INV}\omega\text{com}} = \begin{bmatrix} C_{\omega\text{com}} & 0_{1\times 15(n-1)}\end{bmatrix}$.

Node voltages

Based on the concept of the virtual resistor [81], the node voltages across the feeder are given by

$$\boldsymbol{v}_{\text{c,DQ},i} = r_{\text{N}}\boldsymbol{i}_{\text{c,DQ},i} + r_{\text{N}}\left(\boldsymbol{i}_{\text{line,DQ},i-1} - \boldsymbol{i}_{\text{line,DQ},i}\right), \tag{4.21}$$

where r_{N} is the virtual resistance, sufficiently large so as not to influence the stability. So the small-signal state-space model is given as

$$\Delta\boldsymbol{v}_{\text{C,DQ}} = R_{\text{N}}\Delta\boldsymbol{i}_{\text{C,DQ}} + R_{\text{N}}R_{\text{NET}}\Delta\boldsymbol{i}_{\text{LINE,DQ}}, \tag{4.22}$$

where $R_{\text{N}} = \text{diag}\{r_{\text{N}}\}_{2n\times 2n}$,

$$R_{\text{NET}} = \begin{bmatrix} -I & 0 & 0 & \dots & 0 & 0 \\ I & -I & 0 & \dots & 0 & 0 \\ 0 & I & -I & \dots & 0 & 0 \\ \dots & \dots & \dots & \dots & \dots & \dots \\ 0 & 0 & 0 & \dots & I & -I \\ 0 & 0 & 0 & \dots & 0 & I \end{bmatrix}_{2n\times 2(n-1)}, \text{ and } I = \begin{bmatrix} 1 & 0 \\ 0 & 1 \end{bmatrix}.$$

4.1.3 DC side dynamics

As explained before, the DC-side energy source in Fig. 4.1 can be modelled either as a constant DC voltage source or with a detailed converter model. When focusing on the impact of microgrid expansion on stability, we can model the DC side as a constant DC voltage source. However, when we consider the DC-side dynamics, an explicit model of the DC side is required, including the DC/DC converter and the dynamic response of the energy source.

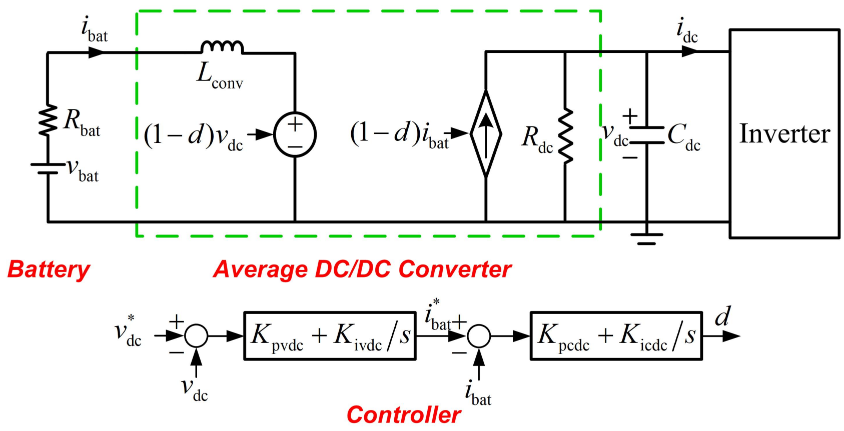

Figure 4.3: Detailed DC-side configuration.

Detailed DC-side model

In islanded operation, the energy source on the DC side has to be dispatchable, i.e. it has to be able to change the output on request. The most common technology is battery storage coupled with a rooftop solar PV, which we will assume in this chapter. However, our modelling framework is general and can also accommodate other technologies, e.g. microturbines or fuel cells. The DC side energy source is typically integrated with a bidirectional DC/DC converter (BDC) to keep the DC-link voltage at the desired value and to allow bidirectional power exchange between the energy source and the system, which we model as a constant voltage source behind a resistance [187].

The BDC used in connecting battery storage systems has been shown in Fig. 3.7. The controller for such a converter regulates the DC-link voltage and the battery's output current. Because we assume that the battery generates power, the converter operates in a discharging (boost) mode. The detailed DC side configuration with the battery converter and a double-loop controller is shown in Fig. 4.3, where d is the duty cycle of the switching signal.

Following [188], the state equations of the converter are

$$\dot{\alpha} = v_{\mathrm{dc}}^* - v_{\mathrm{dc}}, \tag{4.23a}$$

$$R_{\mathrm{dc}} C_{\mathrm{dc}} \dot{v}_{\mathrm{dc}} = R_{\mathrm{dc}} \left(1 - d\right) i_{\mathrm{bat}} - v_{\mathrm{dc}} - R_{\mathrm{dc}} i_{\mathrm{dc}}, \tag{4.23b}$$

$$\dot{\beta} = i_{\mathrm{bat}}^* - i_{\mathrm{bat}}, \tag{4.23c}$$

$$L_{\mathrm{conv}} \dot{i}_{\mathrm{bat}} = v_{\mathrm{bat}} - \left(1 - d\right) v_{\mathrm{dc}} - R_{\mathrm{bat}} i_{\mathrm{bat}}, \tag{4.23d}$$

along with algebraic equations

$$i_{\mathrm{bat}}^* = K_{\mathrm{pvdc}} \left(v_{\mathrm{dc}}^* - v_{\mathrm{dc}}\right) + K_{\mathrm{ivdc}} \alpha, \tag{4.24a}$$

$$d = K_{\mathrm{pcdc}} \left(i_{\mathrm{bat}}^* - i_{\mathrm{bat}}\right) + K_{\mathrm{icdc}} \beta. \tag{4.24b}$$

The link between the DC side and AC side is established by the active power balance ($P_{\mathrm{dc}} = P_{\mathrm{ac}}$), as follows:

$$v_{\mathrm{dc}} i_{\mathrm{dc}} = \frac{3}{2} \left(v_{\mathrm{d}} i_{\mathrm{d}} + v_{\mathrm{q}} i_{\mathrm{q}}\right). \tag{4.25}$$

Assume the battery voltage v_{bat} is stable enough to make Δv_{bat} negligible in the small-signal stability analysis. Hence the corresponding linearised small-signal state-space equations are

$$\dot{\begin{bmatrix} \Delta\alpha \\ \Delta v_{\text{dc}} \\ \Delta\beta \\ \Delta i_{\text{bat}} \end{bmatrix}} = A_{\text{s}} \begin{bmatrix} \Delta\alpha \\ \Delta v_{\text{dc}} \\ \Delta\beta \\ \Delta i_{\text{bat}} \end{bmatrix} + B_{\text{s}} \begin{bmatrix} \Delta i_{\text{bat}}^{*} \\ \Delta d \\ \Delta i_{\text{dc}} \end{bmatrix}, \tag{4.26a}$$

$$\begin{bmatrix} \Delta i_{\text{bat}}^{*} \\ \Delta d \\ \Delta i_{\text{dc}} \end{bmatrix} = C_{\text{s}} \begin{bmatrix} \Delta\alpha \\ \Delta v_{\text{dc}} \\ \Delta\beta \\ \Delta i_{\text{bat}} \end{bmatrix} + D_{\text{s}} \Delta \boldsymbol{x}_{\text{LCLL}}, \tag{4.26b}$$

where $A_{\text{s}} = \begin{bmatrix} 0 & -1 & 0 & 0 \\ 0 & -\frac{1}{R_{\text{dc}}C_{\text{dc}}} & 0 & \frac{1-D}{C_{\text{dc}}} \\ 0 & 0 & 0 & -1 \\ 0 & -\frac{(1-D)}{L_{\text{conv}}} & 0 & \frac{-R_{\text{bat}}}{L_{\text{conv}}} \end{bmatrix}$, $B_{\text{s}} = \begin{bmatrix} 0 & 0 & 0 \\ 0 & -\frac{I_{\text{bat}}}{C_{\text{dc}}} & -\frac{1}{C_{\text{dc}}} \\ 1 & 0 & 0 \\ 0 & \frac{V_{\text{dc}}}{L_{\text{conv}}} & 0 \end{bmatrix}$,

$C_{\text{s}} = \begin{bmatrix} K_{\text{ivdc}} & -K_{\text{pvdc}} & 0 & 0 \\ K_{\text{pcdc}}K_{\text{ivdc}} & -K_{\text{pcdc}}K_{\text{pvdc}} & K_{\text{icdc}} & -K_{\text{pcdc}} \\ 0 & -\frac{I_{\text{dc}}}{V_{\text{dc}}} & 0 & 0 \end{bmatrix}$, $D_{\text{s}} = \frac{3}{2} \begin{bmatrix} 0 & 0 & 0 & 0 & 0 & 0 & 0 & 0 \\ 0 & 0 & 0 & 0 & 0 & 0 & 0 & 0 \\ 0 & 0 & \frac{I_{\text{d}}}{V_{\text{dc}}} & \frac{I_{\text{q}}}{V_{\text{dc}}} & \frac{V_{\text{d}}}{V_{\text{dc}}} & \frac{V_{\text{q}}}{V_{\text{dc}}} & 0 & 0 \end{bmatrix}$.

I_{dc}, V_{dc}, I_{bat}, and D are steady-state operating values. Assume $\Delta \boldsymbol{x}_{\text{dc}} = \begin{bmatrix} \Delta\alpha & \Delta v_{\text{dc}} & \Delta\beta & \Delta i_{\text{bat}} \end{bmatrix}^{\top}$ and rearrange (4.26)

$$\Delta \dot{\boldsymbol{x}}_{\text{dc}} = A_{\text{dc}} \Delta \boldsymbol{x}_{\text{dc}} + B_{\text{dc}} \Delta \boldsymbol{x}_{\text{inv}}, \tag{4.27}$$

where $A_{\text{dc}} = A_{\text{s}} + B_{\text{s}}C_{\text{s}}$, $B_{\text{dc}} = \begin{bmatrix} 0_{4\times 7} & B_{\text{s}}D_{\text{s}} \end{bmatrix}$.
Combine the DC dynamics of all inverters,

$$\Delta \dot{\boldsymbol{x}}_{\text{DC}} = A_{\text{DC}} \Delta \boldsymbol{x}_{\text{DC}} + B_{\text{DC}} \Delta \boldsymbol{x}_{\text{INV}}, \tag{4.28}$$

where $\Delta \boldsymbol{x}_{\text{DC}} = \begin{bmatrix} \Delta \boldsymbol{x}_{\text{dc},1} & \Delta \boldsymbol{x}_{\text{dc},2} & \ldots & \Delta \boldsymbol{x}_{\text{dc},n} \end{bmatrix}^{\top}$,
$A_{\text{DC}} = \text{diag}\{A_{\text{dc},i}\}_{2n\times 2n}$, $B_{\text{DC}} = \text{diag}\{B_{\text{dc},i}\}_{2n\times 2n}$, $i = 1, 2, \ldots, n$.

Simplified DC-side model

The dynamic response of the primary energy source can negatively affect stability, so it needs to be considered. We model it by a first-order transfer function [84, 186, 189], emulating the primary source's response delay. This can be translated into the response delay of the current output if the primary side's voltage is assumed constant. On the other hand, the detailed DC side model in Fig. 4.3 can be simplified, considering that the current loop is significantly faster than the voltage loop. Therefore, the primary source can be simplified as a single-voltage-loop controlled current source, as shown in Fig. 4.4. Based on this configuration, the first-order transfer function can be introduced between the controller output and the current input, where τ is the time constant of the primary source, emulating

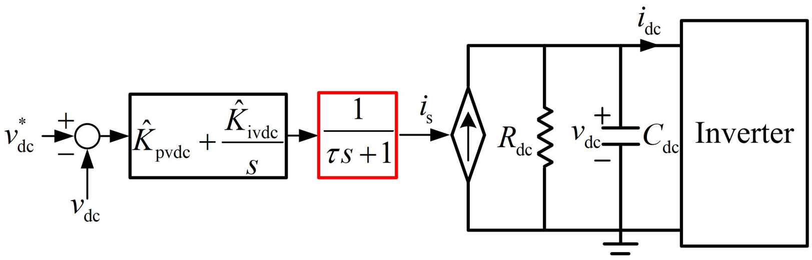

Figure 4.4: Simplified DC-side structure with battery response delay.

the primary source's limited dynamic response. The relation between the controller gains (when $\tau = 0$) in Figs. 4.3 and 4.4 is

$$\widehat{K}_{\text{pvdc}} = (1 - D)\, K_{\text{pvdc}}, \qquad \widehat{K}_{\text{ivdc}} = (1 - D)\, K_{\text{ivdc}}. \tag{4.29}$$

Hence the new dynamic equations of the DC dynamics are modified to

$$R_{\text{dc}} C_{\text{dc}} \dot{v}_{\text{dc}} = R_{\text{dc}} i_{\text{s}} - v_{\text{dc}} - R_{\text{dc}} i_{\text{dc}}, \tag{4.30a}$$
$$\tau \dot{i}_{\text{s}} = -i_{\text{s}} + \widehat{K}_{\text{pvdc}} \left(v_{\text{dc}}^* - v_{\text{dc}}\right) + \widehat{K}_{\text{ivdc}} \alpha. \tag{4.30b}$$

Hence the new state-space equations of the DC dynamics are changed as

$$\Delta \dot{\hat{\boldsymbol{x}}}_{\text{dc}} = \hat{A}_{\text{dc}} \Delta \hat{\boldsymbol{x}}_{\text{dc}} + \hat{B}_{\text{dc}} \Delta \boldsymbol{x}_{\text{inv}}, \tag{4.31}$$

where $\Delta \hat{\boldsymbol{x}}_{\text{dc}} = \begin{bmatrix} \Delta\alpha & \Delta v_{\text{dc}} & \Delta i_{\text{s}} \end{bmatrix}^\top$,

$$\hat{A}_{\text{dc}} = \begin{bmatrix} 0 & -1 & 0 \\ 0 & \frac{I_{\text{s}}}{C_{\text{dc}} V_{\text{dc}}} - \frac{2}{C_{\text{dc}} R_{\text{dc}}} & \frac{1}{C_{\text{dc}}} \\ \frac{\hat{K}_{\text{ivdc}}}{\tau} & -\frac{\hat{K}_{\text{pvdc}}}{\tau} & -\frac{1}{\tau} \end{bmatrix},\ \hat{B}_{\text{dc}} = \frac{3}{2} \frac{1}{C_{\text{dc}} V_{\text{dc}}} \begin{bmatrix} & & & & 0_{1\times 15} & & & & \\ 0_{1\times 7} & 0 & 0 & I_{\text{d}} & I_{\text{q}} & V_{\text{d}} & V_{\text{q}} & 0 & 0 \\ & & & & 0_{1\times 15} & & & & \end{bmatrix}.$$

4.2 Stability analysis

Small-signal stability is dictated by the eigenvalues of the state matrix [76]. This section analyzes how microgrid expansion and the DC dynamics affect the stability, respectively.

4.2.1 Eigenvalue analysis with respect to microgrid expansion

Microgrid expansion can be conducted by simply adding more grid-forming inverters along the feeder as shown in Fig. 4.2. Eigenvalue analysis with respect to microgrid expansion is studied by neglecting the influence of the DC dynamics. Hence in this subsection, DC-side sources are considered as constant voltage sources. Therefore, the complete linearised model of the residential microgrid can be obtained based on Section 4.1.2, as follows:

$$\begin{bmatrix} \Delta \dot{\boldsymbol{x}}_{\text{INV}} \\ \Delta \boldsymbol{i}_{\text{LINE,DQ}} \end{bmatrix} = \boldsymbol{A}_{\text{SYS}} \begin{bmatrix} \Delta \boldsymbol{x}_{\text{INV}} \\ \Delta \boldsymbol{i}_{\text{LINE,DQ}} \end{bmatrix}. \tag{4.32}$$

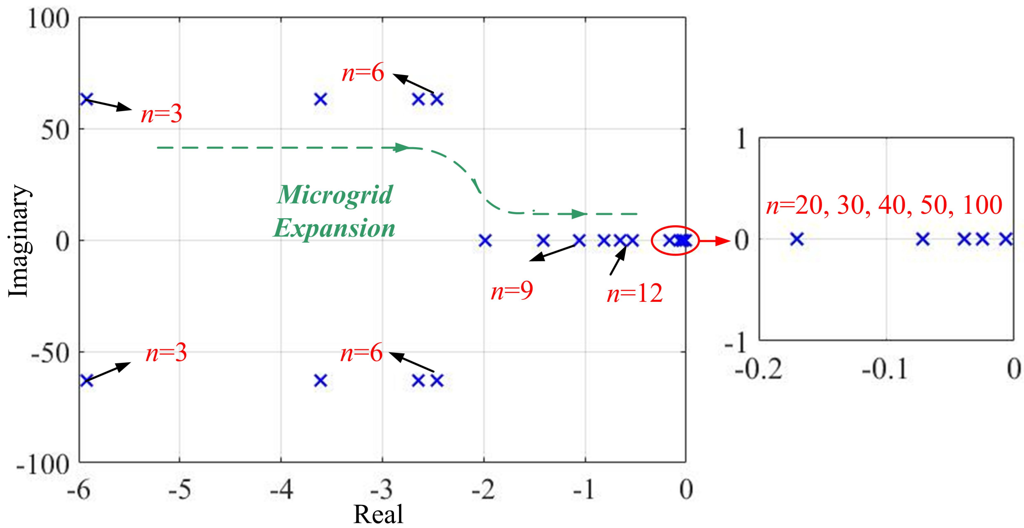

Figure 4.5: Critical eigenvalue trajectory with microgrid expansion.

The state matrix is

$$\boldsymbol{A}_{\text{SYS}} = \begin{bmatrix} A_{\text{INV}} + B_{\text{INV}} R_{\text{N}} C_{\text{INVC}} & B_{\text{INV}} R_{\text{N}} R_{\text{NET}} \\ B_{\text{1NET}} R_{\text{N}} C_{\text{INVC}} + B_{\text{2NET}} C_{\text{INV}\omega\text{com}} & A_{\text{NET}} + B_{\text{1NET}} R_{\text{N}} R_{\text{NET}} \end{bmatrix}. \tag{4.33}$$

The stability information can be obtained from the eigenvalues of matrix $\boldsymbol{A}_{\text{SYS}}$. Attention is paid to the critical eigenvalue. It should be pointed out that matrix $\boldsymbol{A}_{\text{SYS}}$ always has a zero eigenvalue (not linked to instability) associated with one of the inverters serving as the reference. Hence we exclude this eigenvalue in the stability analysis. In this paper, we consider systems with three to one hundred prosumers. These systems are linearised around steady-state operating points, and the resulting system matrices are used to derive the eigenvalues.

Fig. 4.5 shows the trajectory of the critical eigenvalue (the eigenvalue with the largest real part) of $\boldsymbol{A}_{\text{SYS}}$ with the increasing number of prosumers. Observe that the critical eigenvalue starts as a pair of complex-conjugate eigenvalues with less than six prosumers. With the increasing number of prosumers, the critical eigenvalue changes its type to a real eigenvalue (when $n \geq 7$). Here, we define these two different types of eigenvalues as λ_{c} (complex eigenvalue pair with the largest real part) and λ_{r} (real eigenvalue with the largest real part). During the microgrid expansion, the critical eigenvalue moves towards the imaginary axis (it equals to -0.00625 in the case of the 100-prosumer microgrid), which means that the system becomes "practically unstable" when more prosumers are integrated. To get a better insight into the nature of the two dominant eigenvalues λ_{c} and λ_{r}, we analyze state participation and parameter sensitivity next.

Here, dominant eigenvalues are defined to be eigenvalues located closest to the imaginary axis. While there can be several dominant eigenvalues, the critical eigenvalue is the eigenvalue with the largest real part (a real eigenvalue or a pair of conjugate eigenvalues).

Table 4.1: Participation factors of dominant states

	Number of prosumers (eigenvalue value)	Dominant states	Participation factors
λ_{r}	$n = 3\ (-15.64)$	$\Delta\delta_2, \Delta\delta_3$	$0.81, 1.52$
	$n = 6\quad(-2.975)$	$\Delta\delta_5, \Delta\delta_6$	$0.4, 0.69$
	$n = 9\quad(-1.052)$	$\Delta\delta_8, \Delta\delta_9$	$0.36, 0.45$
	$n = 12\quad(-0.5351)$	$\Delta\delta_{11}, \Delta\delta_{12}$	$0.29, 0.33$
	$n = 50\quad(-0.02446)$	$\Delta\delta_{49}, \Delta\delta_{50}$	$0.0784, 0.0849$
	$n = 100\quad(-0.006225)$	$\Delta\delta_{99}, \Delta\delta_{100}$	$0.0401, 0.0432$
λ_{c}	$n = 3$ $(-5.924 \pm \mathrm{i}63.31)$	$\Delta\psi_{\mathrm{dq1}}$, $\Delta\psi_{\mathrm{dq2}}$ ΔP_2, ΔQ_2	$0.11, 0.27$ $0.062, 0.051$
	$n = 6$ $(-2.467 \pm \mathrm{i}62.97)$	$\Delta\psi_{\mathrm{dq3}}$, $\Delta\psi_{\mathrm{dq4}}$ ΔP_3, ΔQ_3	$0.148, 0.124$ $0.034, 0.028$
	$n = 9$ $(-2.436 \pm \mathrm{i}62.97)$	$\Delta\psi_{\mathrm{dq3}}$, $\Delta\psi_{\mathrm{dq4}}$ ΔP_3, ΔQ_3	$0.148, 0.124$ $0.034, 0.028$
	$n = 12$ $(-2.444 \pm \mathrm{i}62.97)$	$\Delta\psi_{\mathrm{dq3}}$, $\Delta\psi_{\mathrm{dq4}}$ ΔP_3, ΔQ_3	$0.148, 0.124$ $0.034, 0.028$
	$n = 50$ $(-2.444 \pm \mathrm{i}63.02)$	$\Delta\psi_{\mathrm{dq3}}$, $\Delta\psi_{\mathrm{dq4}}$ ΔP_3, ΔQ_3	$0.146, 0.126$ $0.0328, 0.0274$
	$n = 100$ $(-2.444 \pm \mathrm{i}63.02)$	$\Delta\psi_{\mathrm{dq3}}$, $\Delta\psi_{\mathrm{dq4}}$ ΔP_3, ΔQ_3	$0.146, 0.126$ $0.0328, 0.0274$

Participation factors

Participation factor analysis is used to measure the association between states and modes [76,77] by identifying how the states participate in the specific modes associated with λ_{r} and λ_{c}. Table 4.1 lists the participation factors of several dominant states with respect to λ_{r} and λ_{c} during the microgrid expansion. Other states with smaller participation factors may also influence certain modes but not predominantly. Observe in Table 4.1 that with the increasing number of prosumers, λ_{r} is predominantly participated by the angle shift of the last prosumer $\Delta\delta_n$, which means that λ_{r} is predominantly determined by the maximum number of prosumers. This can also be seen from the value of λ_{r} that increases from -15.64 to -0.00625 during the expansion; that is, with each newly added prosumer, the critical eigenvalue moves closer to the origin. Therefore, it is clear that λ_{r} is predominantly sensitive to the microgrid expansion.

By comparison, λ_{c} is mostly participated by the powers ΔP and ΔQ and the voltage error integral terms ($\Delta\psi_{\mathrm{dq}}$). When the number of prosumers increases from three to five, λ_{c} is predominantly participated by different prosumers. However, since $n = 6$, it is clear to see that λ_{c} keeps being predominantly participated by the 3rd and 4th prosumers. Also, the value of λ_{c} almost does not change with the increasing number of prosumers, which indicates its insensitivity to the microgrid expansion.

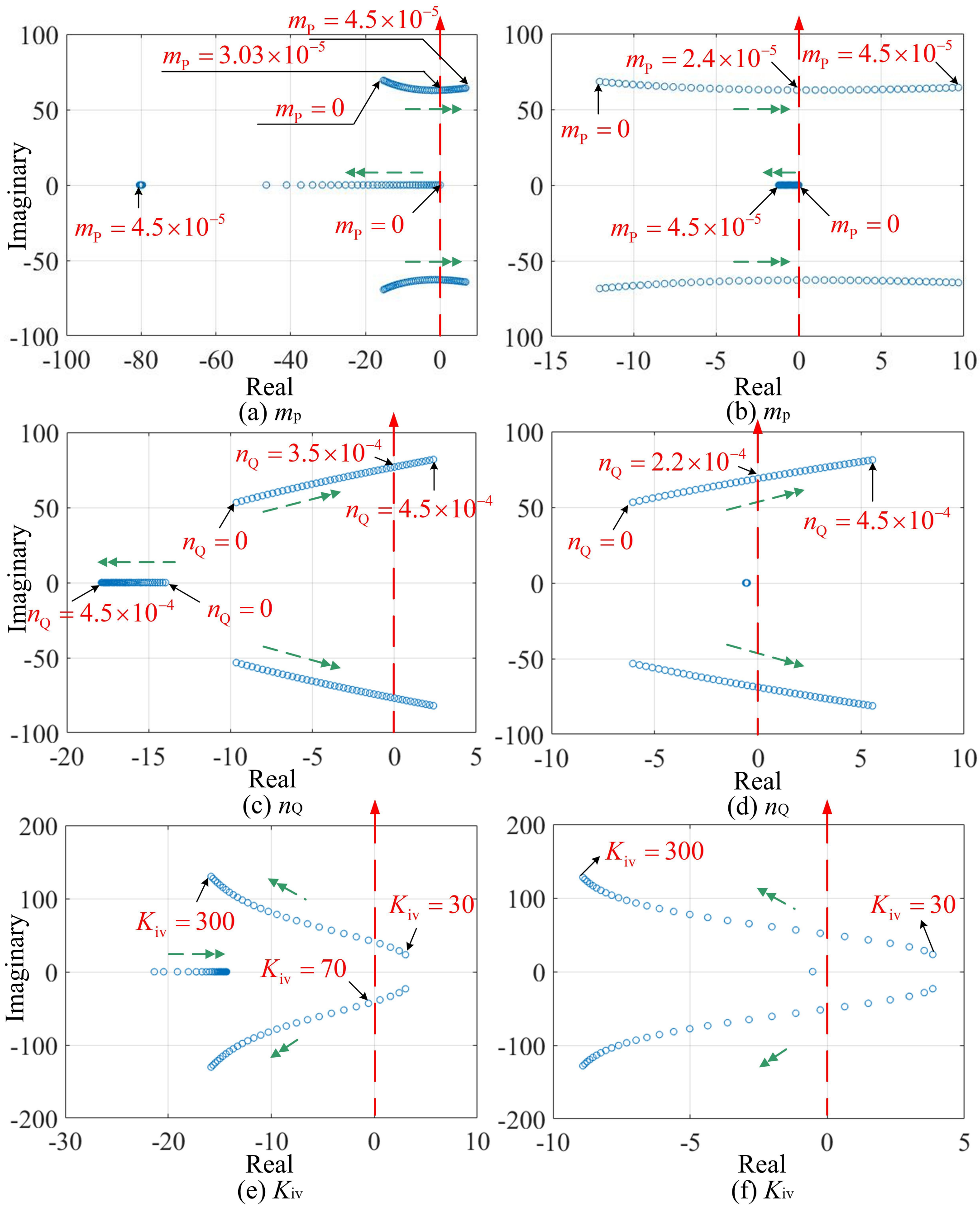

Figure 4.6: Eigenvalue trajectories for a 3-prosumer (left column) and 12-prosumer microgrid (right column). (a,b) $0 \leq m_P \leq 4.5 \times 10^{-5}$; (c,d) $0 \leq n_Q \leq 4.5 \times 10^{-4}$; (e,f) $30 \leq K_{iv} \leq 300$.

This explains the trend shown in Fig. 4.5, where the critical eigenvalue changes it type from λ_c to λ_r as the number of prosumers grows larger.

Sensitivity analysis

As λ_c is mostly participated by ΔP, ΔQ and $\Delta\psi_{dq}$, the sensitivity analysis will therefore focus on droop gains m_P and n_Q, and voltage integral gain K_{iv}. Fig. 4.6 shows the trajectory of λ_r and λ_c as a function of m_P for microgrids with, respectively, 3 and 12-prosumers. n_Q is fixed as 1.3×10^{-4} while m_P varies from 0 to 4.5×10^{-5}.

Observe in Fig. 4.6 (a) that with the increasing m_P, λ_c moves to the right from $\lambda_c = -15.62 \pm j69.76$

(at $m_\mathrm{P} = 0$), passing through the imaginary axis at $m_\mathrm{P} = 3.03 \times 10^{-5}$ and shifting to the right half of the s plane, at which point the system becomes unstable. This illustrates how large droop gains cause instability. Comparatively, as m_P increases, λ_r moves to the left starting at 0 when $m_\mathrm{P} = 0$. This is mainly because m_P determines the output frequency and thus the angle of each prosumer. As analyzed before, λ_r is predominantly participated by $\Delta\delta_n$. λ_r is therefore sensitive to the change of m_P. However, this sensitivity exhibits the opposite trend to that of λ_c, indicating that a larger active droop gain pushes λ_r further away from the unstable region. On the other hand, observe in Fig. 4.6 (b) that within the same variation range of m_P, the range of λ_r gets narrower with the microgrid expansion, while the range of λ_c experiences no noticeable change. This behaviour further demonstrates that λ_r is predominantly sensitive to the microgrid expansion. A qualitatively similar behaviour is observed also for n_Q (Fig. 4.6, second row), which is explained by the coupling between real and reactive powers due to the high R/X ratio of the transmission lines.

The sensitivity analysis of the integral term of the current regulator K_iv (Fig. 4.6, third row) shows that λ_c moves to the left with the increase of K_iv, while λ_r is almost unaffected by K_iv in a large system. A small value of K_iv will therefore cause the instability. Hence K_iv should be tuned with a relatively large value to push λ_c far away from the unstable region, which might result in an overshoot. On the other side, K_iv, which is relevant to the controller bandwidth, is constrained by the switching frequency of the PWM generation module. These issues should be taken into consideration when tuning the controller gains.

Stability enhancement

Observe in Fig. 4.6 that λ_r and λ_c move in opposite directions as m_P increases, which indicates that droop gains should be tuned so that the real parts of λ_r and λ_c are equal. In general, in small microgrids where λ_c is the critical eigenvalue, stability can be enhanced by decreasing the droop gains. With the increasing number of prosumers, on the other hand, when λ_r becomes the critical eigenvalue, stability enhancement can be achieved by increasing the droop gains.

We use a seven-prosumer microgrid to illustrate the tuning of the droop gain to enhance stability. The dominant eigenvalues in the base case ($m_\mathrm{P} = 2 \times 10^{-5}$ and $K_\mathrm{iv} = 115$) are shown in Fig. 4.7 (a). The dominant real eigenvalue is $\lambda_\mathrm{r} = -1.982$, while the dominant complex eigenvalue is $\lambda_\mathrm{c} = -2.436 \pm \mathrm{i}62.97$. It is clear that λ_r serves as the critical eigenvalue in this case. Hence the aim is to move λ_r further away from the origin. First, to move λ_c further to the left without changing the position of λ_r, we increase K_iv to 240. The corresponding movement of the dominant eigenvalues is shown in Fig. 4.7 (b), where the blue and red dots represent the eigenvalues before and after the parameter change, respectively. Moving λ_c to the left provides a wider acceptable variation range for m_P; this is because m_P should be increased to move λ_r to the left, which at the same time pushes λ_c to the right. We now increase m_P, which makes the real parts of λ_r and λ_c equal. Fig. 4.7 (c) shows the motion of λ_r and λ_c when m_P is increased to 3.2×10^{-5}, which results in the eigenvalues being $\lambda_\mathrm{r} = -3.212$ and $\lambda_\mathrm{c} = -3.312 \pm \mathrm{i}105.7$, respectively.

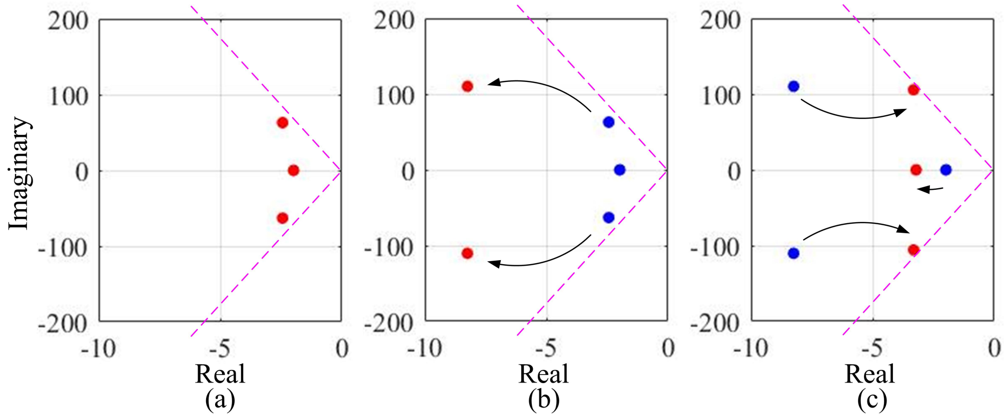

Figure 4.7: Stability enhancement example (blue dots: before the change; red dots: after the change; dotted lines: 3% damping margin). (a) dominant eigenvalues in the base case; (b) K_{iv} increasing from 115 to 240; (c) m_{P} increasing from 2×10^{-5} to 3.2×10^{-5}.

4.2.2 Eigenvalue analysis with a detailed model of the DC side

This subsection analyzes the stability by explicitly modelling the DC side converter and its controls as illustrated in Fig. 4.3. Therefore, the complete linearised model of a residential microgrid consists of models described in Sections 4.1.2 and 4.1.3, as follows:

$$\dot{\begin{bmatrix} \Delta \boldsymbol{x}_{\text{INV}} \\ \Delta \boldsymbol{i}_{\text{LINE,DQ}} \\ \Delta \boldsymbol{x}_{\text{DC}} \end{bmatrix}} = \boldsymbol{A}_{\text{SYSnew}} \begin{bmatrix} \Delta \boldsymbol{x}_{\text{INV}} \\ \Delta \boldsymbol{i}_{\text{LINE,DQ}} \\ \Delta \boldsymbol{x}_{\text{DC}} \end{bmatrix}, \tag{4.34}$$

where $\Delta \boldsymbol{x}_{\text{DC}} = \begin{bmatrix} \Delta \boldsymbol{x}_{\text{dc},1}^{\top} & \Delta \boldsymbol{x}_{\text{dc},2}^{\top} & \Delta \boldsymbol{x}_{\text{dc},3}^{\top} & \dots & \Delta \boldsymbol{x}_{\text{dc},n}^{\top} \end{bmatrix}^{\top}$. The state matrix is changed into

$$\boldsymbol{A}_{\text{SYSnew}} = \begin{bmatrix} A_{\text{INV}} + B_{\text{INV}} R_{\text{N}} C_{\text{INVC}} & B_{\text{INV}} R_{\text{N}} R_{\text{NET}} & 0_{15n \times 4n} \\ B_{1\text{NET}} R_{\text{N}} C_{\text{INVC}} + B_{2\text{NET}} C_{\text{INV}\omega\text{com}} & A_{\text{NET}} + B_{1\text{NET}} R_{\text{N}} R_{\text{NET}} & 0_{2(n-1) \times 4n} \\ B_{\text{DC}} & 0_{4n \times 2(n-1)} & A_{\text{DC}} \end{bmatrix}. \tag{4.35}$$

The stability of the microgrid with the detailed model of the DC side can now be assessed through the eigenvalue analysis of $\boldsymbol{A}_{\text{SYSnew}}$. We start with the case of a 3-prosumer microgrid.

Dominant eigenvalues

Fig. 4.8 (a) shows several dominant eigenvalues located closest to the imaginary axis. Comparing the eigenvalues in Fig. 4.8 (a) and Table 4.1, it can be seen that λ_{r} and λ_{c} are not affected by the DC side dynamics, staying at $\lambda_{\text{r}} = -15.64$ and $\lambda_{\text{c}} = -5.924 \pm j63.31$, respectively. However, a new dominant eigenvalue λ_{rdc}, much larger than λ_{r} appears and becomes the critical eigenvalue in the system, which reduces the stability margin significantly.

Participation factors

Participation factor analysis of A_{SYSnew} reveals that λ_{rdc} is predominantly participated by $\Delta\alpha_3$ with the participation factor of 1.035, meaning that λ_{rdc} is mainly affected by the DC side voltage controller.

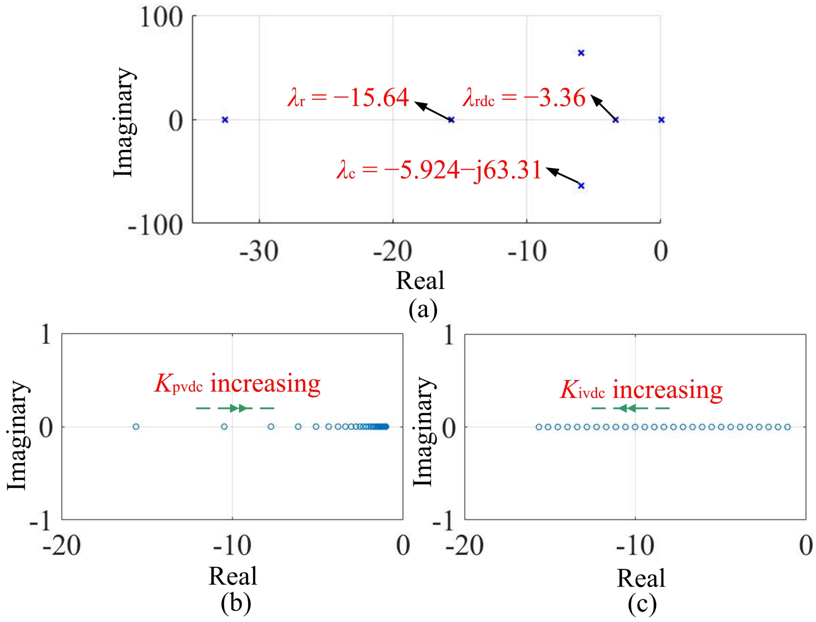

Figure 4.8: (a) Dominant eigenvalues of A_{SYSnew} for a 3-prosumer microgrid; (b) Trajectory of λ_{rdc} when $1 \leq K_{\mathrm{pvdc}} \leq 30$; (c) Trajectory of λ_{rdc} when $10 \leq K_{\mathrm{ivdc}} \leq 300$.

Sensitivity analysis of λ_{rdc} in 3-prosumer microgrid

Sensitivity analysis can be carried out with respect to the gains of the DC side voltage controller K_{pvdc} and K_{ivdc} (see Fig. 4.3). Fig. 4.8 (b) and (c) show trajectories of λ_{rdc} as a function of K_{pvdc} and K_{ivdc}, respectively. It can be seen that λ_{rdc} exhibits opposite movement with regards to K_{pvdc} and K_{ivdc}, moving to the right with increasing K_{pvdc} while moving to the left as K_{ivdc} increases. The study of the trajectories of λ_{r} and λ_{c} shows that varying K_{pvdc} and K_{ivdc} has no influence on these two eigenvalues. Hence, stability can be enhanced by adjusting the DC side voltage controller gains without affecting λ_{r} and λ_{c}. After λ_{rdc} moves away from the imaginary axis, no longer serving as the critical eigenvalue, λ_{r} and λ_{c} dominate the system stability as analyzed in Section 4.2.1.

Sensitivity of λ_{rdc} to microgrid expansion

Eigenvalue λ_{rdc} is associated with the DC-voltage controller, whose dynamics is not coupled with the network. Therefore, there exists n identical λ_{rdc} in an n-prosumer microgrid. The sensitivity analysis reveals that the value of λ_{rdc} remains at -3.36 as the number of prosumers increases, which indicates that λ_{rdc} is insensitive to microgrid expansion.

4.2.3 Eigenvalue analysis with a simplified DC side model

Now we analyze the microgrid stability by considering the dynamic response of the DC side primary energy source using a simplified model shown in Fig. 4.4. Therefore, the complete model of the

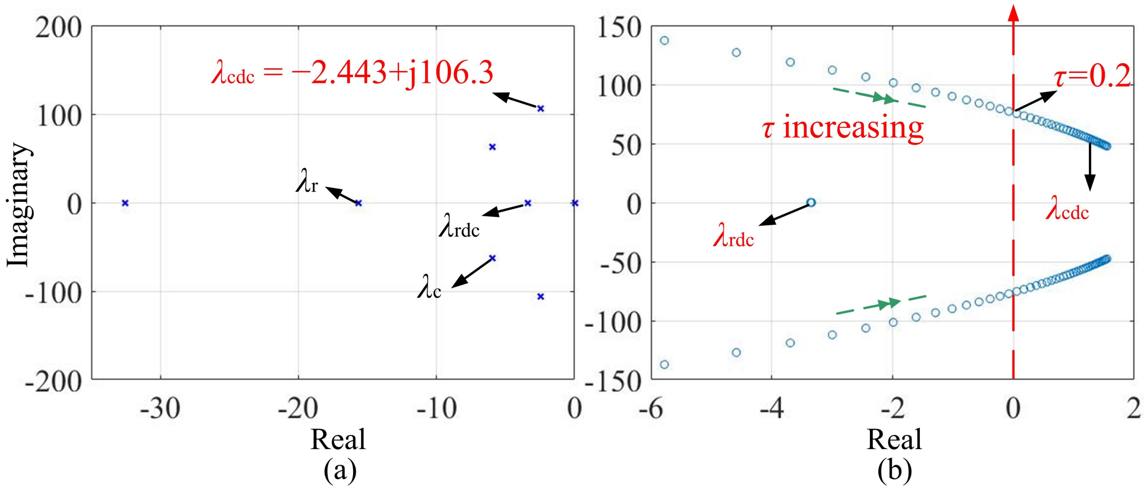

Figure 4.9: (a) Dominant eigenvalues of $\widehat{A}_{\text{SYSnew}}$ for a 3-prosumer microgrid ($\tau = 0.1\,\text{s}$); (b) Trajectory of λ_{cdc} as a function of $0.06\,\text{s} \leq \tau \leq 0.5\,\text{s}$.

residential microgrid consists of models described in Sections 4.1.2 and 4.1.3, as follows:

$$\begin{bmatrix} \Delta \dot{\boldsymbol{x}}_{\text{INV}} \\ \Delta \boldsymbol{i}_{\text{LINE,DQ}} \\ \Delta \widehat{\boldsymbol{x}}_{\text{DC}} \end{bmatrix} = \widehat{\boldsymbol{A}}_{\text{SYSnew}} \begin{bmatrix} \Delta \boldsymbol{x}_{\text{INV}} \\ \Delta \boldsymbol{i}_{\text{LINE,DQ}} \\ \Delta \widehat{\boldsymbol{x}}_{\text{DC}} \end{bmatrix}, \tag{4.36}$$

where $\Delta\widehat{\boldsymbol{x}}_{\text{DC}} = \begin{bmatrix} \Delta\widehat{\boldsymbol{x}}_{\text{dc},1}^{\top} & \Delta\widehat{\boldsymbol{x}}_{\text{dc},2}^{\top} & \Delta\widehat{\boldsymbol{x}}_{\text{dc},3}^{\top} & \dots & \Delta\widehat{\boldsymbol{x}}_{\text{dc},n}^{\top} \end{bmatrix}^{\top}$.

The influence of the dynamic response of the DC side primary energy source on stability can be studied by analyzing the simplified DC side model and the corresponding state matrix $\widehat{\boldsymbol{A}}_{\text{SYSnew}}$. Similarly, $\widehat{\boldsymbol{A}}_{\text{SYSnew}}$ is formed based on the 3-prosumer microgrid.

Dominant eigenvalues and participation factors

The dominant eigenvalues of the 3-prosumer microgrid (for $\tau = 0.1\,\text{s}$) are plotted in Fig. 4.9 (a). Observe that the addition of the first-order transfer function representing the dynamic response of the DC side energy source introduces a new complex eigenvalue $\lambda_{\text{cdc}} = -2.443 \pm j106.3$, with λ_{c}, λ_{r} and λ_{rdc} remaining unchanged. The dominant states in this eigenvalue are $\Delta v_{\text{dc},3}$ and $\Delta i_{\text{s},3}$ with the participation factors of 0.5 and 0.499, respectively. As $\Delta i_{\text{s},3}$ is the output of the first order transfer function (see Fig. 4.4), this indicates that τ affects stability through λ_{cdc}.

Sensitivity to the response time from primary sources τ

Fig. 4.9 (b) shows the trajectory of λ_{rdc} and λ_{cdc} as a function of τ. With the increase of τ, λ_{rdc} remains unchanged, indicating its insensitivity to the response speed of the DC side energy source. By contrast, as τ increases, λ_{cdc} moves to the right, passing across the imaginary axis into the right half-plane. This means that too high a value of τ can cause instability, which indicates that care must be taken when grid-forming inverters are supplied by a primary energy source with an insufficiently fast dynamic response.

Table 4.2: System parameters of the residential microgrid case in Section 4.3

Parameter	Value	Parameter	Value
ω^*	$314.15\,\mathrm{rad/s}$	v^*_{mag}	$326.6\,\mathrm{V}$
m_{P}	2×10^{-5}	K_{pc}	3.5
n_{Q}	1.3×10^{-4}	K_{ic}	260
ω_{f}	$120\,\mathrm{rad/s}$	R_{f}	$0.01\,\Omega$
K_{pv}	0.05	L_{f}	$1.3\,\mathrm{mH}$
K_{iv}	115	C_{f}	$100\,\mu\mathrm{F}$
F	0.8	L_{c}	$0.35\,\mathrm{mH}$

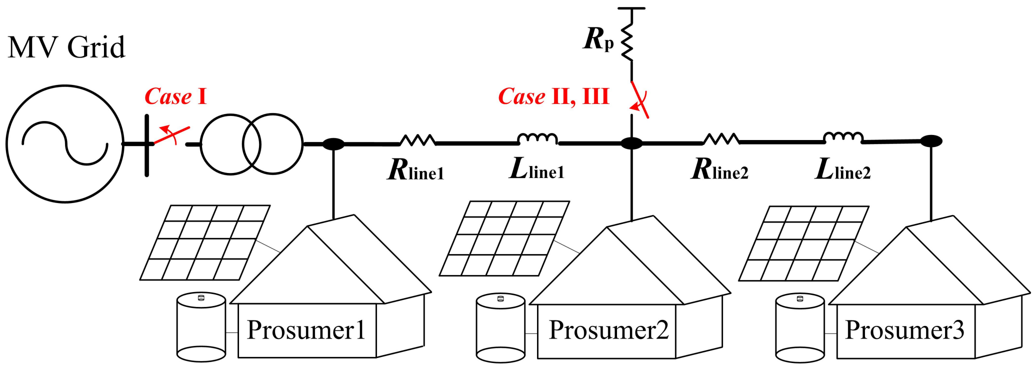

Figure 4.10: Three-prosumer residential microgrid.

4.3 Time-domain simulation results

Time-domain simulations are carried out for three purposes. The first is to confirm that a LV distribution feeder supplied by grid-forming inverters can seamlessly switch from grid-connected to islanded operation. The second is to validate the accuracy of linearised state-space models (4.32)-(4.36). The last is to verify the equivalence between the detailed model shown in Fig. 4.3 and the simplified model, with the dynamic response from the DC side energy source represented as a first-order transfer function (Fig. 4.4). The simulations were carried out on an RTDS/RSCAD™platform.

We used a test system with three prosumers, shown in Fig. 4.10. The test system is based on a European $400\,\mathrm{V}$, $50\,\mathrm{Hz}$ LV residential benchmark system [190]. System parameters are shown in Table 4.2. The loads for each prosumers are, respectively, $P_{\mathrm{load,1}} = 5\,\mathrm{kW}$, $Q_{\mathrm{load,1}} = 2\,\mathrm{kVAr}$, $P_{\mathrm{load,2}} = 3\,\mathrm{kW}$, $Q_{\mathrm{load,2}} = 1\,\mathrm{kVAr}$, $P_{\mathrm{load,3}} = 5\,\mathrm{kW}$, $Q_{\mathrm{load,3}} = 1\,\mathrm{kVAr}$. Because the converter's switching dynamics is much faster than the dynamics of the network, we use an average state-space converter model, which is a standard practice in this kind of analysis.

4.3.1 Case I: network separation

Case I studies the system response during a separation from the medium-voltage (MV) grid to confirm the feasibility of a residential LV feeder operated as a microgrid. Fig. 4.11 shows active and reactive power flows during a network separation (at $0.2\,\mathrm{s}$). In the grid-connected mode, all active power is

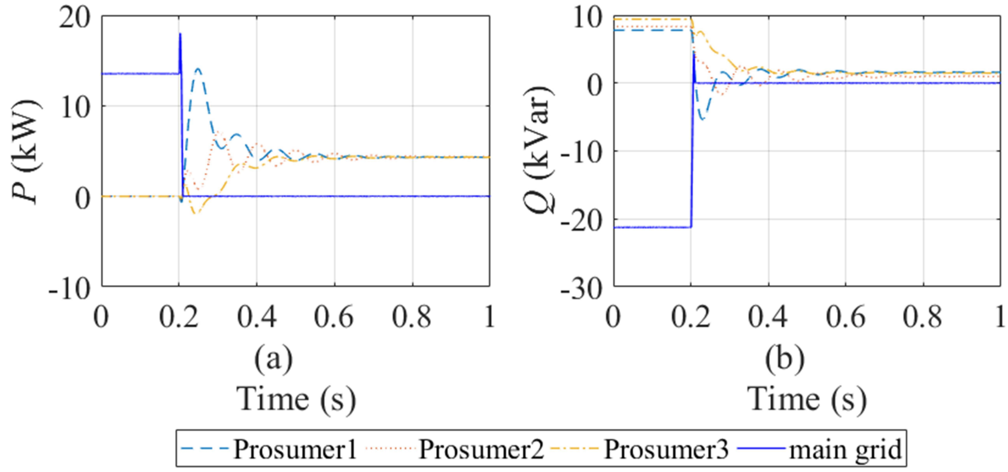

Figure 4.11: Active and reactive powers for a network separation of a 3-prosumer microgrid: (a) active powers; (b) reactive powers.

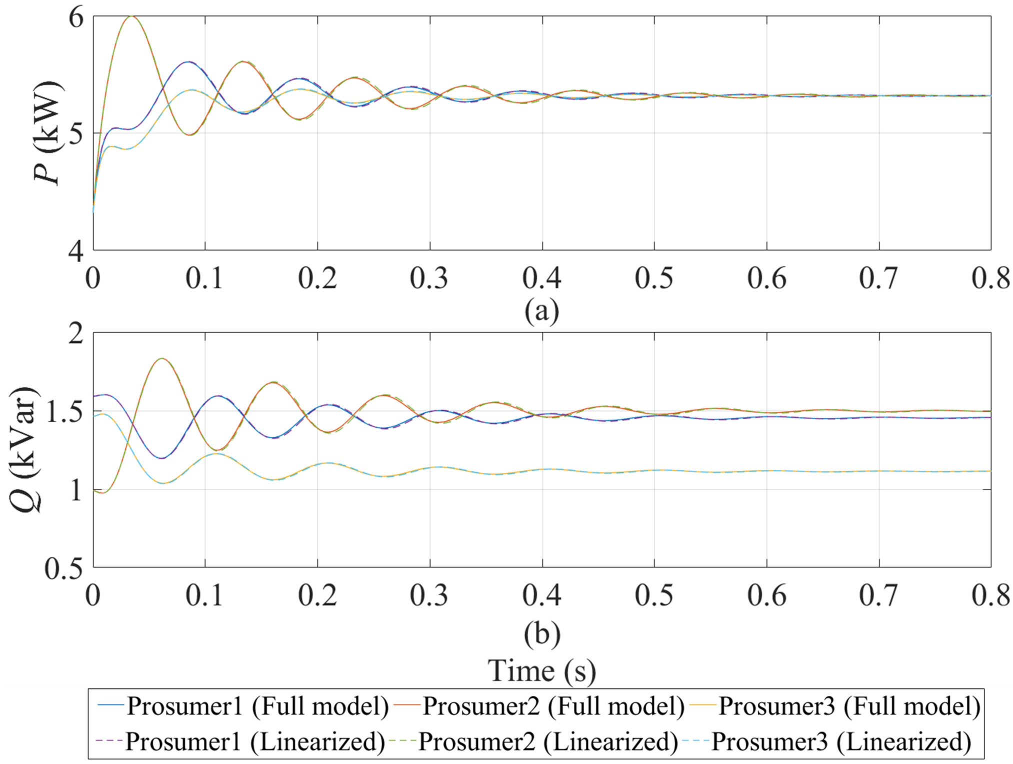

Figure 4.12: Islanded operation of a 3-prosumer microgrid with constant DC-voltage source on the DC side: (a) active powers of Prosumers 1, 2, and 3; (b) reactive powers of Prosumers 1, 2, and 3.

supplied by the main grid, while some amount of reactive power is supplied by the prosumers. When the network switch is opened at $0.2\,\mathrm{s}$, the system seamlessly transitions to a new steady-state in islanded mode. Active power loads are shared equally by all prosumers, while the reactive power loads are mainly supplied locally.

4.3.2 Case II: islanded operation with DC side dynamics neglected

Case II validates the accuracy of the linearised microgrid model (4.32) by comparing the small-signal stability results and the corresponding time-domain simulation results for a step load change of $3\,\mathrm{kW}$

on Prosumer 2. In the linearised model, this is done by injecting the equivalent current in Node 2. In the full model, the load change is simulated by connecting resistance $R_\mathrm{p} = 53.33\Omega$ to Prosumer 2, as illustrated in Fig. 4.10. The simulation results are shown in Fig. 4.12, including the active power and reactive power response of the three prosumers. Observe that the results of the linearised model match the time-domain simulations almost perfectly.

The main reason for relatively poorly damped oscillations is the low impedance of the transmission lines. Because this is a residential LV feeder, prosumers are electrically close together. Hence the short lines segments between prosumers have relatively low impedance. The other reason is the choice of the cut-off frequency w_f of the low-pass filter in the droop controller, set to $120\,\mathrm{rad/s}$. The damping could be improved by reducing the value of w_f.

4.3.3 Case III: Islanded operation with DC side dynamics

Case III consists of two parts. First, we validate the model with a detailed representation of the DC side shown in Fig. 4.3 by comparing the linearised model (4.34) against the full model. Next, we compare microgrid models with a full DC side representation (Fig. 4.3) and a simplified one (Fig. 4.4). We use the same step load change as in Case II. Parameters of DC-side components are shown in Table 4.3. Fig. 4.13 shows the DC-link voltage of Prosumer 2 resulting from the linearised model (4.34), detailed

Table 4.3: DC-side parameters in Section 4.3

Parameters	Values	Parameters	Values
R_bat	$0.01\,\Omega$	v_dc^*	$800\,\mathrm{V}$
L_conv	$1.25\,\mathrm{mH}$	K_pvdc	9.08
R_dc	$10\,\mathrm{k}\Omega$	K_ivdc	30.4
C_dc	$4000\,\mu\mathrm{F}$	K_pcdc	0.005
v_bat	$400\,\mathrm{V}$	K_icdc	0.5

model (Fig. 4.3), and simplified model (Fig. 4.4). Observe that the results from the three models agree well. The models differ slightly at the very first instant after the perturbation. The system with the detailed source-converter model experiences a relatively larger voltage drop than the other two models. This is mainly because the converter is driven by the duty cycle, which is saturated within $0 \sim 1$. Active and reactive powers results are qualitatively similar to the ones shown in Fig. 4.12 so we do not show them. In summary, the results of Case III confirm the accuracy of the linearised model (4.34) and the equivalence between the detailed source-converter model (Fig. 4.3) and the simplified controlled-current source model (Fig. 4.4).

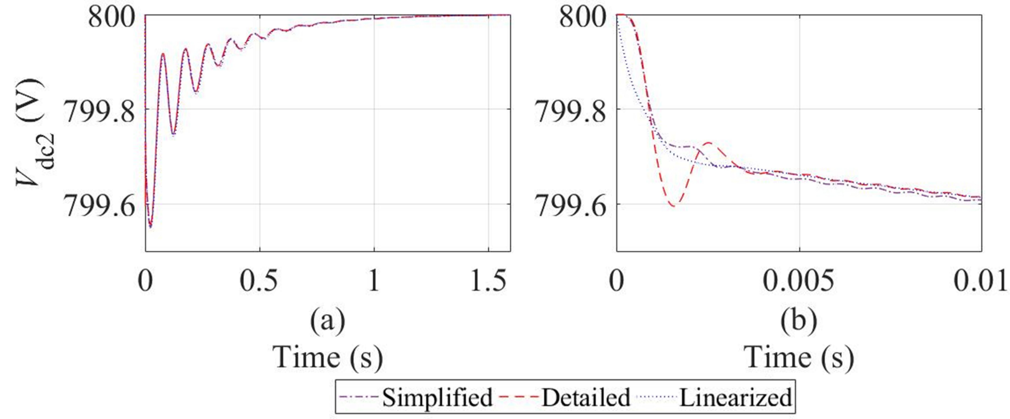

Figure 4.13: DC side dynamics for a network separation of a 3-prosumer microgrid: (a) DC-link voltage of Prosumer 2; (b) Zoomed-in results.

4.4 Single-phase prosumer case

In the previous study cases, the microgrid model assumes a single-phase equivalent model of a balanced three-phase system. However, prosumers in residential microgrids are mainly single phase. To consider a more realistic residential microgrid case, the control and linearised model of single-phase grid-forming prosumers are discussed in this section.

According to Section 3.1.3, single-phase inverters can also be controlled in the dq0 frame by creating a fictitious quadrature signal. Thus, the control structure of single-phase inverters can be the same as for three-phase inverters, with droop control and cascaded voltage/current controllers. In this case, the modelling process of individual inverters is the same as in Section 4.1.2, with the power-related equations changed into

$$P = \frac{\omega_\mathrm{f}}{s+\omega_\mathrm{f}} \cdot \frac{1}{2}(v_\mathrm{d} i_\mathrm{d} + v_\mathrm{q} i_\mathrm{q}), \tag{4.37a}$$

$$Q = \frac{\omega_\mathrm{f}}{s+\omega_\mathrm{f}} \cdot \frac{1}{2}(v_\mathrm{q} i_\mathrm{d} - v_\mathrm{d} i_\mathrm{q}). \tag{4.37b}$$

Consequently, the only difference between microgrid models with single-phase prosumers and three-phase prosumers is the change of the gain, which means that eigenvalues in such systems will have the same characteristic to what has been shown in Section 4.3. Such conclusion supports the stability analysis of the residential microgrid even when considering more realistic single-phase connections.

4.4.1 Time-domain simulation

To verify the validation of the new microgrid model, time-domain simulations are provided. Fig. 4.14 shows the diagram of the studied microgrid case. Individual inverters and their controllers are designed with same parameters, while residential loads of each prosumer at each phase are set with different values. System parameters are listed in Table. 4.4.

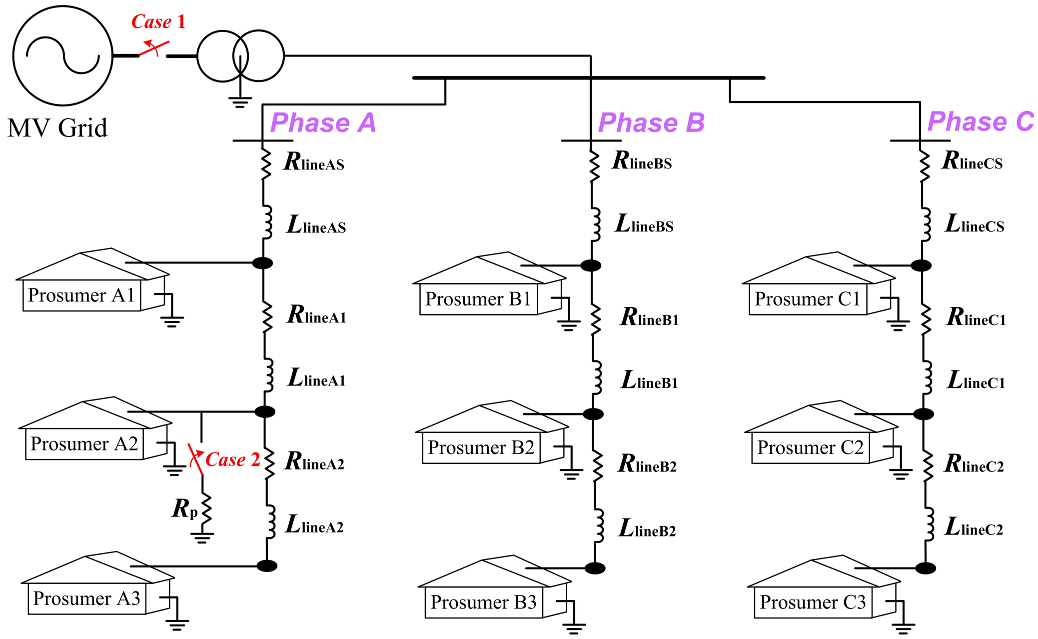

Figure 4.14: Single-phase residential microgrid test case.

Table 4.4: System parameter of the single-phase microgrid test case in Section 4.4

			Individual Inverter				
ω^*	$314.15\,\mathrm{rad/s}$	v^*_{mag}	$326.6\,\mathrm{V}$	m_{P}	2×10^{-5}	n_{Q}	1.3×10^{-4}
K_{pv}	1	K_{iv}	16.5	K_{pc}	5.024	K_{ic}	62.8
R_{f}	$0.01\,\Omega$	L_{f}	$1\,\mathrm{mH}$	C_{f}	$100\,\mu\mathrm{F}$	L_{c}	$0.6\,\mathrm{mH}$
			Phase A				
R_{loadA1}	$9.12\,\Omega$	L_{loadA1}	$0.0116\,\mathrm{H}$	R_{loadA2}	$15.87\,\Omega$	L_{loadA2}	$0.0168\,\mathrm{H}$
R_{loadA3}	$10.17\,\Omega$	L_{loadA3}	$0.006\,48\,\mathrm{H}$	R_{lineAS}	$0.089\,\Omega$	L_{lineAS}	$16.58\,\mathrm{mH}$
R_{lineA1}	$0.18\,\Omega$	L_{lineA1}	$27\,\mathrm{mH}$	R_{lineA2}	$0.12\,\Omega$	L_{lineA2}	$18\,\mathrm{mH}$
			Phase B				
R_{loadB1}	$11.4\,\Omega$	L_{loadB1}	$0.0145\,\mathrm{H}$	R_{loadB2}	$19.84\,\Omega$	L_{loadB2}	$0.021\,\mathrm{H}$
R_{loadB3}	$12.71\,\Omega$	L_{loadB3}	$0.0081\,\mathrm{H}$	R_{lineBS}	$0.089\,\Omega$	L_{lineBS}	$16.58\,\mathrm{mH}$
R_{lineB1}	$0.18\,\Omega$	L_{lineB1}	$27\,\mathrm{mH}$	R_{lineB2}	$0.12\,\Omega$	L_{lineB2}	$18\,\mathrm{mH}$
			Phase C				
R_{loadC1}	$6.84\,\Omega$	L_{loadC1}	$0.0087\,\mathrm{H}$	R_{loadC2}	$11.9\,\Omega$	L_{loadC2}	$0.0126\,\mathrm{H}$
R_{loadC3}	$7.63\,\Omega$	L_{loadC3}	$0.004\,86\,\mathrm{H}$	R_{lineCS}	$0.089\,\Omega$	L_{lineCS}	$16.58\,\mathrm{mH}$
R_{lineC1}	$0.18\,\Omega$	L_{lineC1}	$27\,\mathrm{mH}$	R_{lineC2}	$0.12\,\Omega$	L_{lineC2}	$18\,\mathrm{mH}$

Case I: Network separation

Similar as for the residential microgrid with three-phase prosumers in Section 4.4.1, Case I in this section studies the system response during a separation from the MV grid for the microgrid with single-phase prosumers. Fig. 4.15 shows active and reactive power flows during a network separation (at $1\,\mathrm{s}$). Similar as the cases in Section 4.3, in the grid-connected mode, all active power is supplied by the main grid, while some amount of reactive power is supplied by the prosumers. When the network switch is opened at $1\,\mathrm{s}$, the system seamlessly transitions to a new steady-state in islanded mode. Active power loads are shared equally by all prosumers, while the reactive power loads are mainly supplied

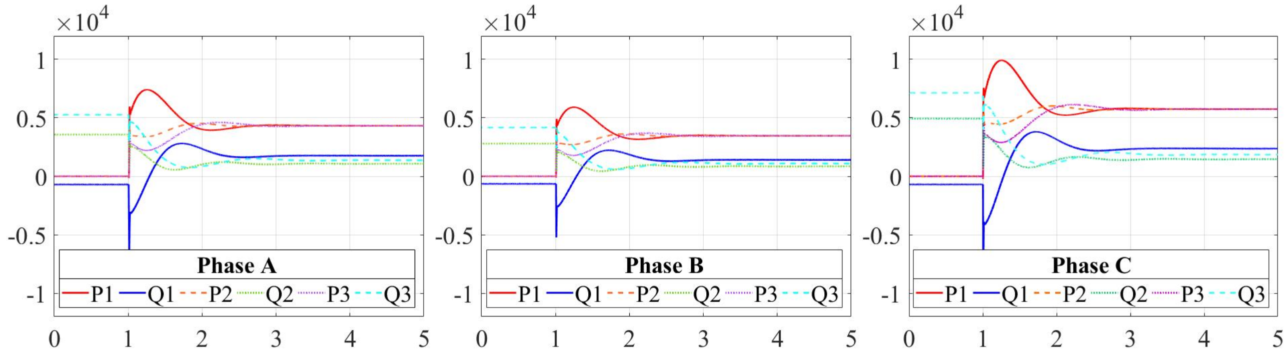

Figure 4.15: Active and reactive powers for a network separation of a 9-single-phase-prosumer microgrid.

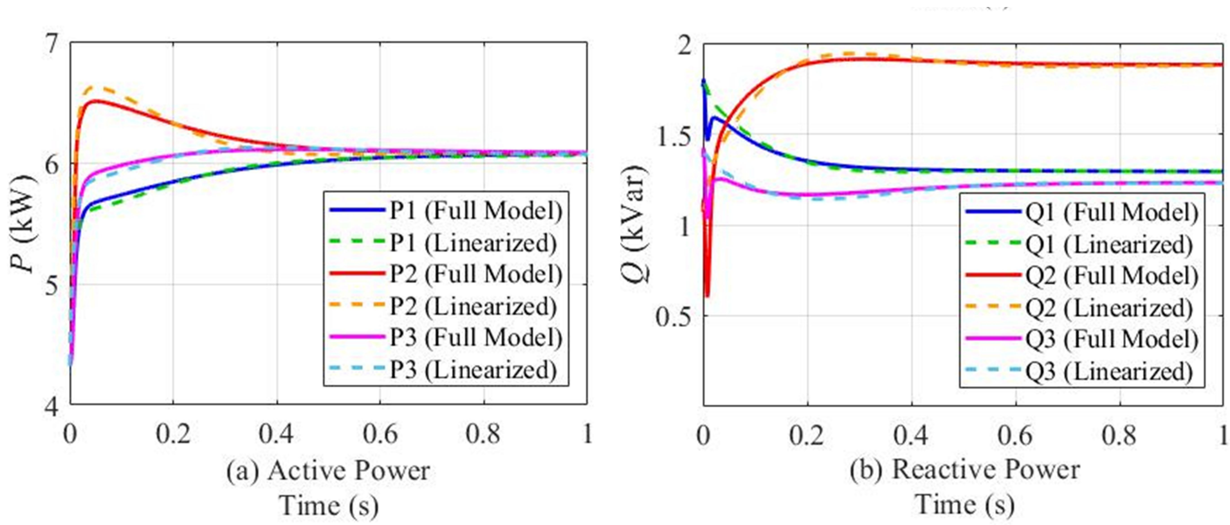

Figure 4.16: Islanded operation of a 9-single-phase-prosumer microgrid.

locally.

Case II: Islanded microgrid

Case II validates the accuracy of the linearised microgrid model with single-phase prosumers. The simulation focuses on one phase as we do not pay much attention to the inter-phase power exchange. Take Phase A in Fig. 4.14 as the test case. A disturbance is applied at Prosumer 2 with a load change of 3 kW. Time-domain simulation results as well as corresponding linearised model results are shown in Fig. 4.3. Observe that the results of the linearised model match the time-domain simulations almost perfectly. A slight difference can be seen during the beginning of the perturbation, where time-domain simulations show a slight oscillation. This is because of the delay caused by the 'transfer delay unit' which generates the fictitious quadrature signal. Better quadrature generation methods can be adopted to avoid this [171].

4.5 Summary

This chapter has studied the stability of LV distribution feeders operated as islanded residential microgrids supplied by prosumer-owned grid-forming inverters. The analysis is performed on a linearised microgrid model focusing on two key aspects: (i) number of grid-forming inverters in a radial feeder, (ii) dynamic response of the energy source on the DC side. The small-signal stability results have been confirmed against time-domain simulation results.

The eigenvalue analysis for various cases has revealed that: 1) an LV feeder operated as an islanded microgrid becomes "practically unstable" with the increasing number of grid-forming inverters; 2) during the microgrid expansion, the critical eigenvalue switches from a pair of complex eigenvalues associated with the droop controller to a real eigenvalue predominantly sensitive to the system size (number of grid-forming inverters); 3) stability can be enhanced by adjusting the gains of the droop controller and the voltage controller; 4) the DC side voltage controller affect system stability by introducing new dominant eigenvalues; 5) insufficiently fast dynamic response of the primary energy source can negatively affect stability.

Moreover, to consider a more realistic residential microgrid, modelling is extended to the microgrid with prosumers whose interfaced inverters are single phase. With the generation of fictitious quadrature signals, the control of single-phase grid-forming inverters are the same with the three-phase ones. Time-domain simulation results have been compared with the small-signal model results to verify the validity of the model. It is concluded that with single-phase prosumer integration, the stability results are the same with the results in microgrids with three-phase inverters.

This chapter studies the short-term small-signal stability of residential microgrids. As illustrated in Chapter 2, the frequency stability is also an important issue in such microgrid due to the low inertia resulted from the integration of inverter-interfaced generation sources. Prosumers in the residential level, on the other hand, can serve as potential inertia provider with proper control strategies. Hence, making use of prosumers to provide inertia will be discussed in the following chapters.

Chapter 5

Improved Controller for Battery Converter based on Active Disturbance Rejection Control

It is now widely accepted that renewable generations are the cheapest long-term supply option due to their lower size, continuously reduced price and eco-friendly feature. As a result, many fossil-fuel-dependent power plants have been replaced by large scale of renewable generations such as solar farms and wind farms. This trend, however, challenges the existing generation-following-load operation paradigm based on *dispatchable synchronous* generation. Most renewable energy sources (RES) are connected to the grid through power electronic converters, which fundamentally changes the power system behavior. An important concern is the system inertia.

In a conventional power system dominated by large synchronous machines, inertia comes from the kinetic energy stored in the rotating masses of synchronous generators. Such energy serves as an immediate source of energy that reduces frequency excursions following a loss of either generation or load. In a system with a high penetration of non-synchronous sources, on the other hand, a power imbalance can result in a high rate of change of frequency (RoCoF) immediately after the disturbance, as explained in Chapter 2.

To improve the inertial response in low-inertia power systems, a possible solution is to replace genuine "mechanical" inertia with fast frequency response (FFR) provided by energy storage with fast response (e.g. battery or super-capacitor). If the activation time is sufficiently short, FFR can be used as a substitute for genuine inertia. On the other side, as the number of prosumers equipped by various energy storage grows rapidly in recently years, using prosumers as the providers of FFR creates unique opportunities to address the challenges associated with the lack of inertia. Against this backdrop, prosumers can be designed to provide FFR to the system using their installed residential PV-battery systems, to augment the limited energy storage provided by the DC-link capacitor.

To use a PV-battery system as a provider of FFR, we need to pay special attention to the speed of the battery's response. Bidirectional DC/DC converters (BDCs) which connect the battery bank to the

DC bus are widely used to allow the power flow between the battery and other power conversion units. Hence the control of BDC is crucial for PV-battery systems to provide FFR to the grid. There exist many different BDC topologies. A classic BDC is shown in Fig. 3.7. The conventional double-loop PI controller discussed in Chapter 3 is widely adopted in controlling the BDC based on the linearised model. As a typical BDC can operate in either *buck mode* (charging) or *boost mode* (discharging), many proposed control strategies design controllers for each mode individually. For instance, a possible approach was proposed in [191] which determined modes by the DC bus voltage error and generated the duty cycle of the switches. However, a discontinuous duty cycle can result in power fluctuations. Uncertain power fluctuations would be caused, leading to a reduced battery lifetime. In [192, 193], control strategies were designed for microgrids, in which individual control loops for each mode in the BDC were implemented, and the operating modes were selected by an external control signal. In [192], the power delivery was determined by the command from a central controller, which connected all units with a communication link. However, central controllers have issues with limited bandwidth due to the long distance of communication. Unpredictable conditions of the microgrid tend to be caused if communication failure happens. Such communication limitation was resolved by the emergence of distributed control systems [194, 195]. Charging/discharging modes were selected by a fault detector. Hence the strategy alleviated the reliance on the communication. Nevertheless, the interchange of control loops caused by the mode selection might cause instability. To improve the reliability of the controller, [195] and [196] designed combined charging and discharging control loops for autonomous mode switching. In [197], the proposed scheme combined different modes by setting the amplitude limiting part, which avoids the step change of the control input. During the mode transition, the duty cycle of the converter changed continuously, providing a faster and smoother transient response.

However, these methods are basically based on the linearised small-signal model and the conventional PI controller, which only ensures small-signal stability near the operating point. When large disturbances apply, however, these linear control methods may become ineffective and the system may be unstable [177]. Many advanced control technologies are therefore proposed to deal with the inaccuracy of the model and large load variations. Controllers based on model predictive control (MPC) have been proposed in [198–200], aiming to mitigate the influence of constant power loads. MPC methods predict the future response of the system based on the mathematical model. The predicted variables are used to generate control inputs in the coming several periods. As basic MPC methods depend on the accurate model of the system which is not accessible in real applications, error estimation techniques such as Luenburger observers, Kalman filters and higher-order sliding-mode observers are applied to modify the MPC algorithm. In [201, 202], DC/DC converters with constant power loads are stabilized by composite back-stepping controllers. The basic idea is to design a back-stepping controller for large-signal stabilization through a recursive Lyapunov design procedure [177]. Sliding mode control (SMC) is also an option of DC/DC converters to stabilize constant power loads. Different sliding-mode surface were selected in [203–205] to cater for the design requirements of the converter. An SMC-based duty ratio controllers with fixed switching frequency was proposed in [206].

Despite various advanced control methods for DC/DC converters, most relevant literature focused

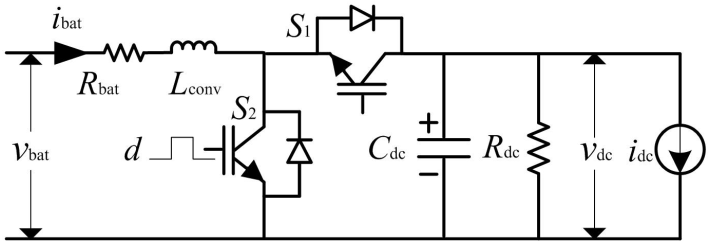

Figure 5.1: Equivalent model of a bidirectional DC/DC converter.

on one-direction power flow, in which the DC converters work in only Boost or Buck mode. Hence, this chapter will discuss the bidirectional power flow by adopting a novel control scheme. On the basis of the voltage-current double-loop control structure, the *active disturbance rejection control* (ADRC) scheme is adopted to replace the PI controllers. As a control theory featuring independence on the accurate mathematical model of the controlled system, ADRC helps to simplify the process of the calculation and measurement of the internal model parameters [207–209]. As long as the order and the input variable of the system are obtained, the controller can be designed. ADRC defines all factors that may influence the system performance as a *total disturbance*. Based on the theory of the state observer, this total disturbance is observed and then rejected by adding a feed-forward compensation to the input variable. Based on this, ADRC is adopted to regulate not only the DC-link voltage but also the power delivery between the battery and other power conversion units in the system. Importantly, no external signal for mode switching is needed as the ADRC scheme is suitable for both modes like the conventional PI controllers, which avoids the step change during the mode transition process.

5.1 Modelling of the bidirectional DC/DC converter

In the configuration of an individual prosumer, a BDC is adopted between the energy storage and the inverter for a flexible power exchange. The expected output current of the BDC can be determined by the initial inductor current setpoint and the power flow in the grid. When powers from generation units (PVs, wind farms) are more than the load, the battery is charged by the power difference and vice versa. According to the BDC diagram in Fig. 5.1, the equivalent BDC model can be represented as shown in Fig. 5.1, where i_{dc} represents the equivalent active load of the battery. It is determined by the difference between power generations (e.g. PV, grid) and load consumption, which also determines the direction of the battery current.

The state-space averaged model for this converter is expressed as

$$R_{\text{dc}}C_{\text{dc}}\dot{v}_{\text{dc}} = R_{\text{dc}}\left(1-d\right)i_{\text{bat}} - v_{\text{dc}} - R_{\text{dc}}i_{\text{dc}}, \tag{5.1a}$$

$$L_{\text{conv}}\dot{i}_{\text{bat}} = v_{\text{bat}} - \left(1-d\right)v_{\text{dc}} - R_{\text{bat}}i_{\text{bat}}. \tag{5.1b}$$

Based on the linearisation method, the corresponding small-signal state-space equations are

$$\Delta\dot{i}_{\text{bat}} = \frac{1}{L_{\text{conv}}}\Delta v_{\text{bat}} - \frac{R_{\text{bat}}}{L_{\text{conv}}}\Delta i_{\text{bat}} - \frac{1-D}{L_{\text{conv}}}\Delta v_{\text{dc}} + \frac{V_{\text{dc}}}{L_{\text{conv}}}\Delta d, \tag{5.2a}$$

$$\Delta\dot{v}_{\text{dc}} = \frac{1-D}{C_{\text{dc}}}\Delta i_{\text{bat}} - \frac{I_{\text{bat}}}{C_{\text{dc}}}\Delta d - \frac{1}{R_{\text{dc}}C_{\text{dc}}}\Delta v_{\text{dc}} - \frac{1}{C_{\text{dc}}}\Delta i_{\text{dc}}. \tag{5.2b}$$

The duty-ratio-to-inductor-current and inductor-current-to-DC-voltage transfer functions can be derived as

$$G_{\mathrm{di}}(s) = \frac{\Delta i_{\mathrm{bat}}(s)}{\Delta d(s)}\bigg|_{\Delta v_{\mathrm{bat}}=\Delta i_{\mathrm{dc}}=0} = \frac{K_{\mathrm{di}}(s+a)}{s^2+b_1 s+b_2}, \tag{5.3a}$$

$$G_{\mathrm{iv}}(s) = \frac{\Delta v_{\mathrm{dc}}(s)}{\Delta i_{\mathrm{bat}}(s)}\bigg|_{\Delta i_{\mathrm{dc}}=\Delta d=0} = \frac{K_{\mathrm{iv}}}{s+b_3}, \tag{5.3b}$$

where $K_{\mathrm{di}} = \frac{V_{\mathrm{dc}}}{L_{\mathrm{conv}}}$, $K_{\mathrm{iv}} = \frac{1-D}{C_{\mathrm{dc}}}$, $a = \frac{V_{\mathrm{dc}}+(1-D)I_{\mathrm{bat}}R_{\mathrm{dc}}}{R_{\mathrm{dc}}C_{\mathrm{dc}}V_{\mathrm{dc}}}$, $b_1 = \frac{R_{\mathrm{bat}}R_{\mathrm{dc}}C_{\mathrm{dc}}+L_{\mathrm{conv}}}{L_{\mathrm{conv}}R_{\mathrm{dc}}C_{\mathrm{dc}}}$, $b_2 = \frac{R_{\mathrm{bat}}+R_{\mathrm{dc}}(1-D)^2}{L_{\mathrm{conv}}R_{\mathrm{dc}}C_{\mathrm{dc}}}$, $b_3 = \frac{1}{R_{\mathrm{dc}}C_{\mathrm{dc}}}$.

In the conventional double-loop control structure, G_{di} and G_{iv} are applied to determine the PI gains of the controllers K_{pvdc}, K_{ivdc}, K_{pcdc} and K_{icdc}. Commonly, the control bandwidth of the current loop ω_{cl} is designed much larger than the control bandwidth of the voltage loop ω_{vl}. According to [177], the PI gains can be selected as

$$K_{\mathrm{pvdc}} = \frac{\omega_{\mathrm{vl}}C_{\mathrm{dc}}}{1-D}, K_{\mathrm{ivdc}} = K_{\mathrm{pvdc}}\zeta\omega_{\mathrm{vl}}, \tag{5.4a}$$

$$K_{\mathrm{pcdc}} = \frac{\omega_{\mathrm{cl}}L_{\mathrm{conv}}}{v_{\mathrm{dc}}^*}, K_{\mathrm{icdc}} = K_{\mathrm{pcdc}}\zeta\omega_{\mathrm{cl}}, \tag{5.4b}$$

where ζ is a small value between $0.1 \sim 0.2$. Such double-loop controller structure based on PI regulators is often used as a benchmark method to be compared with advanced control methods.

5.2 Improved converter controller based on active disturbance rejection control

ADRC was first proposed by Han [207], and it has been successfully applied in various kinds of uncertain industrial processes including the flight systems, robotic systems, motor systems, and power systems [209]. In ADRC, controller coefficients do not depend on the accurate internal parameters of the controlled system. As can be seen in (5.3), multiple coefficients exist in the converter model while vary with the operation points. Hence, conventional PI controllers can only stabilize the system around a specific operating point, and the integral term may introduce stability issues due to the phase lag [207]. As a result, ADRC is considered as a replacement of the PI controller. By the rejection of the "total disturbance", the controlled system can be regulated into a simple integral system, which features small overshoot and fast response under a specified reference signal $R(t)$.

5.2.1 ADRC theory

The *extended state observer* (ESO) is the core part of ADRC. Consider the following state-space model of a continuous dynamical system uncertainty:

$$\dot{\boldsymbol{x}}(t) = A\boldsymbol{x}(t) + BF(\boldsymbol{x}(t), t) + bBu(t), \tag{5.5a}$$

$$y(t) = x_1(t), \tag{5.5b}$$

where $\boldsymbol{x} \in \mathbf{R}^n$ is the vector of continuous state variables. $y(t)$ is the output to be controlled. $u(t)$ is the input variable, and b is its gain.

$$A = \begin{bmatrix} 0 & 1 & 0 & ... & 0 \\ 0 & 0 & 1 & ... & 0 \\ ... & ... & ... & ... & ... \\ 0 & 0 & 0 & ... & 1 \\ 0 & 0 & 0 & ... & 0 \end{bmatrix}_{n\times n} \quad \text{and} \quad B = \begin{bmatrix} 0 \\ 0 \\ \vdots \\ 0 \\ 1 \end{bmatrix}_{n\times 1}.$$

Note that $F(\boldsymbol{x}(t), t)$ is the "total disturbance" of the system, including both uncertain internal dynamics and external disturbances of the system. The objective here is to make $y(t)$ as desired by using $u(t)$ as the controlled variable.

Many approaches require the knowledge of $F(\boldsymbol{x}(t), t)$ to design the controller. Using the ESO, on the other hand, the exact knowledge of $F(\boldsymbol{x}(t), t)$ is not necessary. Instead, $F(\boldsymbol{x}(t), t)$ can be observed from the output.

Take $F(\boldsymbol{x}(t), t)$ as the extended state variable. So the linear ESO is introduced as

$$\begin{bmatrix} \dot{\boldsymbol{z}}(t) \\ \dot{z}_{n+1}(t) \end{bmatrix} = \begin{bmatrix} A & B \\ 0 & 0 \end{bmatrix} \begin{bmatrix} \boldsymbol{z}(t) \\ z_{n+1}(t) \end{bmatrix} + L_i(x_1(t) - z_1(t)) + b \begin{bmatrix} B \\ 0 \end{bmatrix} u(t), \tag{5.6}$$

where $L_i \in \mathbf{R}^{n+1}$ is the gain of the ESO in which $i = 1 \dots n+1$. By tuning L_i, $\boldsymbol{z} = [z_1, z_2, \dots, z_n]^\top$ and $z_{n+1}(t)$ can serve as the estimation of $\boldsymbol{x}$ and $F(\boldsymbol{x}(t), t)$.

Then taking $u(t)$ as:

$$u(t) = K(R(t) - \boldsymbol{x}(t)) - \frac{z_{n+1}(t)}{b}, \tag{5.7}$$

where $K = [K_1, \dots, K_n]$, $R = [R_1, \dots, R_n]^\top$, $R_i = R_1^{(i-1)}$, system (5.5) is transformed to a cascade n-order integral system with a superior tracking characteristic.

5.2.2 ADRC-based converter controller design

Based on the double-loop control structure, the voltage loop is designed with a much smaller bandwidth than the current loop. Conventional PI regulators are capable of tuning the current loop with a significantly fast response. Hence, the ADRC-based converter controller can be applied only in the voltage loop, aiming at producing the inductance reference i^*_{bat} and regulate the DC voltage v_{dc}.

Rewrite the voltage-relevant equation (5.1a) in the state-space form as

$$\dot{v}_{\text{dc}} = F(t) + b_{\text{v}} i^*_{\text{bat}}. \tag{5.8}$$

It can be seen from (5.8) that the v_{dc}-i^*_{bat} system is a first-order system. Therefore, taking $F(t) = \frac{1-d}{C_{\text{dc}}} i_{\text{bat}} - \frac{1}{R_{\text{dc}} C_{\text{dc}}} v_{\text{dc}} - \frac{1}{C_{\text{dc}}} i_{\text{dc}} - b_{\text{v}} i^*_{\text{bat}}$ as the "total disturbance", a second-order ESO for the external voltage loop can be designed as

$$\begin{cases} \dot{z}_{\text{v}1} = z_{\text{v}2} + l_{\text{v}1}(v_{\text{dc}} - z_{\text{v}1}) + b_{\text{v}} i^*_{\text{bat}} \\ \dot{z}_{v2} = l_{\text{v}2}(v_{\text{dc}} - z_{\text{v}1}) \end{cases}, \tag{5.9}$$

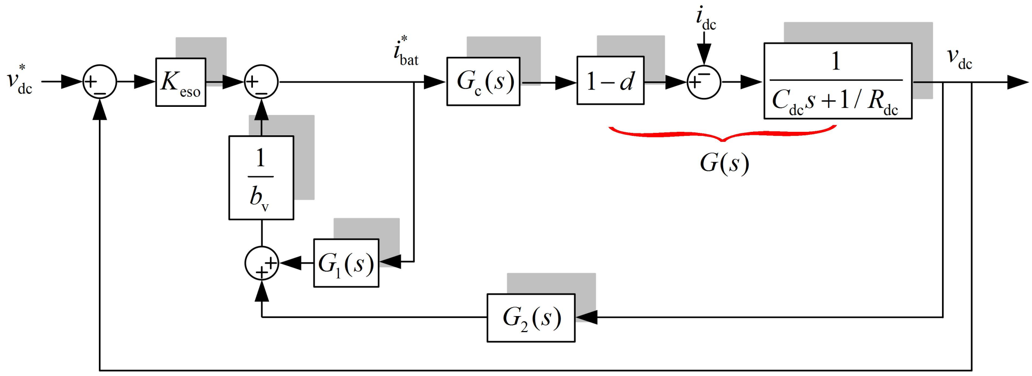

Figure 5.2: Simplified ADRC-based control structure.

where $z_{v1} \to v_{dc}$, and $z_{v2} \to F(t)$ represents the observed total disturbance of the system. Then the system input is designed as

$$i_{bat}^* = K_{eso}(v_{dc}^* - v_{dc}) - \frac{z_{v2}}{b_v}. \tag{5.10}$$

The characteristic polynomial of (5.9) is

$$\left| s\begin{bmatrix} 1 & 0 \\ 0 & 1 \end{bmatrix} - \begin{bmatrix} -l_{v1} & 1 \\ -l_{v2} & 0 \end{bmatrix} \right| = \begin{vmatrix} s + l_{v1} & -1 \\ l_{v2} & s \end{vmatrix} = s^2 + l_{v1}s + l_{v2}. \tag{5.11}$$

Hence, l_{v1} and l_{v2} should be positive to ensure the stability of the observer, and they can be selected as $l_{v1} = 2p, l_{v2} = p^2$, respectively, where p determines the bandwidth of the observer.

Take z_{v2} as the synthetic output generated by v_{dc} and i_{bat}^*. The internal transfer functions of ESO can be expressed as:

$$G_1(s) = \frac{z_{v2}}{v_{dc}} = \frac{p^2 s}{(s+p)^2}, \tag{5.12a}$$

$$G_2(s) = \frac{z_{v2}}{i_{bat}^*} = \frac{-p^2 b_v}{(s+p)^2}. \tag{5.12b}$$

Therefore, a simplified control structure of the system can be illustrated as shown in Fig. 5.2. Thus the closed loop transfer function of the system is simplified as:

$$G_{cl}(s) = \frac{K_{eso}}{K_{eso} + \frac{G_2(s)}{b_v}G_c(s)G(s) + \frac{1}{G_c(s)G(s)} + \frac{1}{b_v}G_1(s)}, \tag{5.13}$$

where

$$G_c(s) = \frac{1}{\tau_c s + 1}, \tag{5.14a}$$

$$G(s) = \frac{1-d}{C_{dc}s + 1/R_{dc}}. \tag{5.14b}$$

τ_c represents the current loop time constant, denoting the dynamic response of the inductor current. With proper tuning of the current loop PI gains, τ_c can be designed with a significantly small value. The roots of the denominator of (5.13) determines the stability of the system.

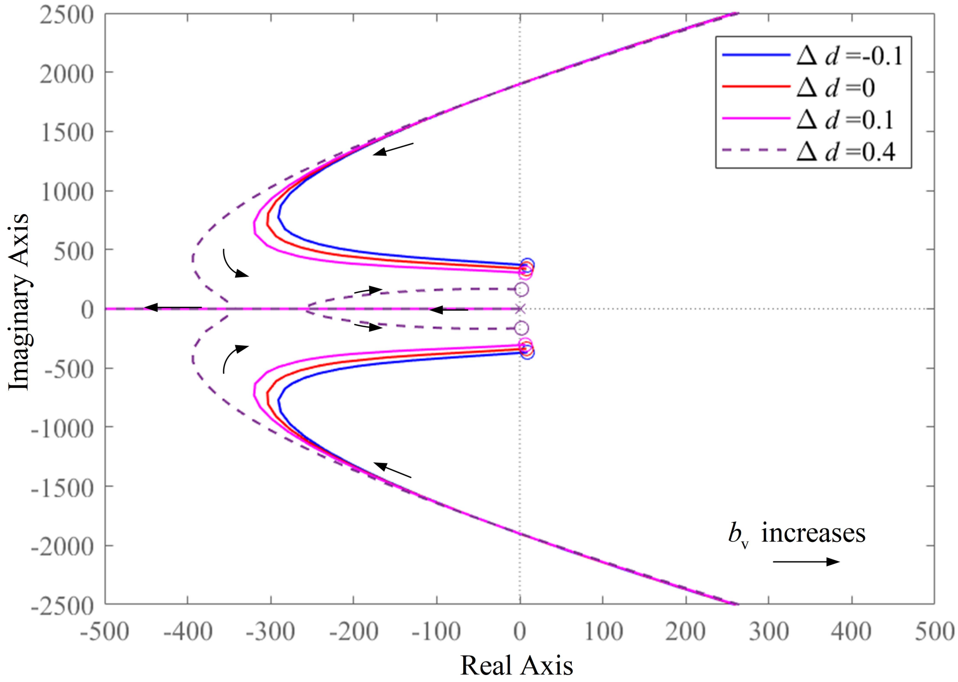

Figure 5.3: Root locus of b_v and Δd.

Note that b_v exists in the numerator of $G_2(s)$ as the gain. Thus the denominator of $G_\mathrm{cl}(s)$ can be written in the form of root locus on b_v as

$$N_2 + b_\mathrm{v} N_1 = 0, \tag{5.15}$$

where

$$N_1 = K_\mathrm{eso} + \frac{G_2(s)}{b_\mathrm{v} G_\mathrm{c}(s) G(s)} + \frac{1}{G_\mathrm{c}(s) G(s)}, \tag{5.16a}$$

$$N_1 = G_1(s). \tag{5.16b}$$

The duty cycle d can be considered with a constant steady-state value plus a small variation as $d = D + \Delta d$. The test system takes D as 0.48. Fig. 5.3 shows part of the root locus of $G_\mathrm{cl}(s)$ on b_v (from 0 to infinity) with varying Δd which is close to the imaginary axis. From Fig. 5.3, the root trajectories show similar characteristics when Δd is small. When b_v starts from 0, critical roots are located in the unstable region (right-hand side of the imaginary axis). As b_v increases, the roots move to the left and enter the stable region. However, the roots will move back to the right when b_v continues increasing. Thus there is a limited range of b_v to ensure the stability of the system. When the Δd is large (see the dotted lines in Fig. 5.3), though the root locus shows a different shape compared with the other three, the general trend is still the same. These root trajectories illustrate that even though the actual duty cycle can be slightly different from the value in the steady-state operating point, it does not influence the selection of b_v when considering the system stability.

In the ADRC-based control strategy, the current loop is thought of as being tuned with a fast enough response, which is represented by a first-order system in the control diagram. Fig. 5.3 shows the root locus of $G_\mathrm{cl}(s)$ on b_v with different value of τ_c. It can be seen that as τ_c increases, the whole locus moves to the right, with the range of b_v which ensures the stability getting narrower. When τ_c increases

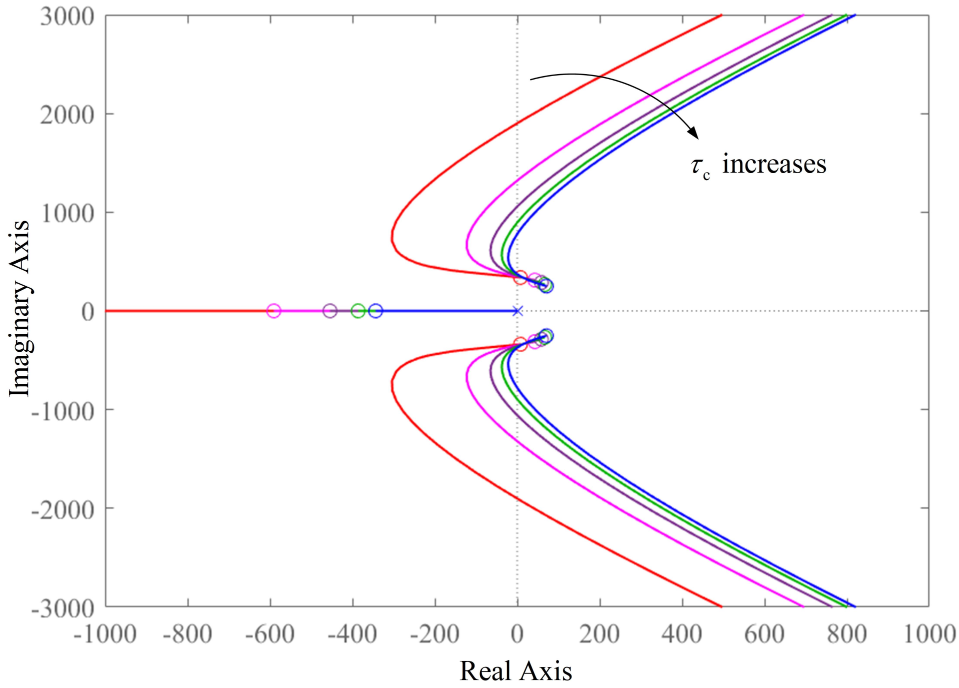

Figure 5.4: Root locus of b_v and τ_c.

to an specific extent, a part of the root locus will be totally located in the unstable region, meaning that no b_v can be selected to ensure the stability. This can be explained by the bandwidth requirement of the double-loop control structure. A large τ_c is interpreted as a small bandwidth in the current loop, which requires that the voltage loop bandwidth should be limited as well. Hence, when the current loop is not fast enough, the voltage loop should be designed with a smaller bandwidth by decreasing p and K_{eso} to ensure stability.

5.3 Simulation verification

5.3.1 PV-battery systems

To demonstrate the theoretical analysis of the proposed control scheme, a grid-connected PV-battery system simulation model has been built in Matlab/Simulink, which is shown in Fig. 5.5. The model consists of the following components:

- **PV arrays**;
- **A DC-DC boost converter** connecting the PV array with the DC bus. The *maximum power point tracking* (MPPT) control is adopted to gain the maximum power of the PV array;
- **A DC to 3-phase voltage source converter (VSC)**. The VSC is controlled by the *grid voltage orientation control* (GOOC) scheme, which is a grid-following control method widely used in grid-interface converters. Active power regulation is also adopted in the VSC controller, which ensures that no power is supplied or absorbed by the grid;
- **A lithium-Ion battery**;

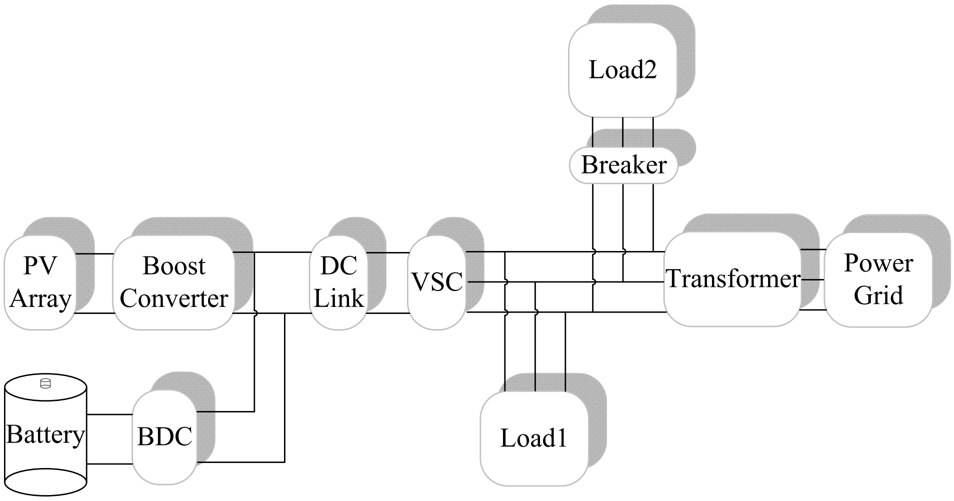

Figure 5.5: PV-battery simulation system.

- **A Bidirectional DC-DC converter** connecting the battery in parallel with the PV array;
- **Two 3-phase loads**;
- **A 100 kVA 260 V/25 kV 3-phase transformer**;
- **A 25 kV power grid**.

Model parameters are provided in Table 5.1.

5.3.2 Simulation process

The simulation operation is described as follows:

(*i*) During 0-$1\,\mathrm{s}$, the power generated by the PV array is held nearly constant at the rated $9\,\mathrm{kW}$ by the MPPT control. Load 1 ($3\,\mathrm{kW}$) is turned on, and the surplus power flows into the battery. Considering the energy-consuming element like resistance and energy storage elements like inductor and capacitor, the power delivered to the battery would be less than $6\,\mathrm{kW}$.

(*ii*) During 1-$2\,\mathrm{s}$, the breaker is switched on to connect Load 2 ($8\,\mathrm{kW}$) to the prosumer. A total of $11\,\mathrm{kW}$ consumed power is applied in the system. The PV system does not supply sufficient power, therefore a complementary power (more than $2\,\mathrm{kW}$) is provided by the battery.

(*iii*) After $2\,\mathrm{s}$, the breaker is switched off to disconnect Load 2. The system turns back to the initial condition.

5.3.3 Simulation results

The simulation results of the proposed scheme is compared with a double-loop controller with conventional PI regulators. The control parameters are provided in Table. 5.2.

Table 5.1: PV-battery microgrid system parameters in Section 5.3

P_{pv}	PV maximum power	$9\,\text{kW}$
C_{bat}	Battery maximum capacity	$40\,\text{A h}$
v_{bat}	Battery nominal voltage	$260\,\text{V}$
P_{L1}	Load 1 power	$3\,\text{kW}$
P_{L2}	Load 2 power	$8\,\text{kW}$
v^*_{dc}	Nominal DC link voltage	$500\,\text{V}$
v_{sec}	Nominal secondary phase voltage	$260\,\text{V}$
f_{grid}	Grid frequency	$50\,\text{Hz}$
C_{dc}	DC-link capacitor	$4000\,\mu\text{F}$
L_{conv}	BDC inductor	$2.35\,\text{mH}$
R_{dc}	DC paralleled resistor	$10\,\text{k}\Omega$

Table 5.2: Control Parameters of Simulations in Section 5.3

K_{pvdc}, K_{ivdc}	Voltage PI gains	$2.512, 197.2$
K_{pcdc}, K_{icdc}	Current PI gains	$0.5, 7.85$
K_{eso}	ADRC voltage error gain	2.512
p	ESO bandwidth	$1800\,\text{rad/s}$
b_{v}	ESO input gain	97
f_{sw}	Switching frequency	$10\,\text{kHz}$

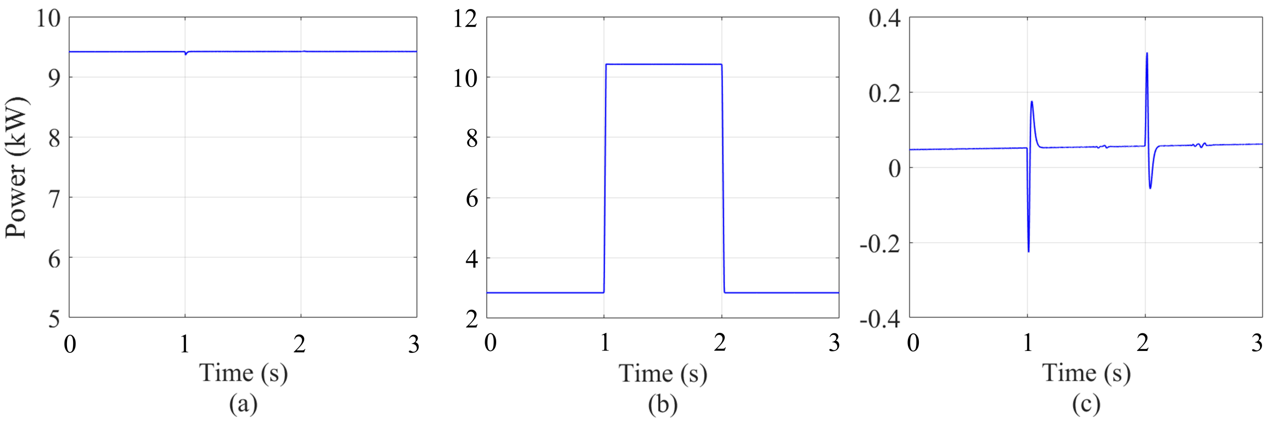

Figure 5.6: Simulation Results. (a) PV power; (b) Load power; (c) Power from the grid.

Conventional PI-based voltage controller

To effectively compare the proposed scheme with the PI control, parameters of the PI voltage controller have been regulated to achieve satisfactory performance. Figs. 5.6, 5.7 and 5.8 show the power flow and the DC-link voltage with PI-based double-loop controller.

In Fig. 5.6, it can be seen that the PV arrays generate constant power, while the power from the grid is controlled to be zero. The load was increased at $1\,\text{s}$ and then de-loaded at $2\,\text{s}$.

1. Battery power: In Fig. 5.7, a negative value of the power means that the battery is absorbing power from the PV array and a positive value means the battery is providing complementary power for

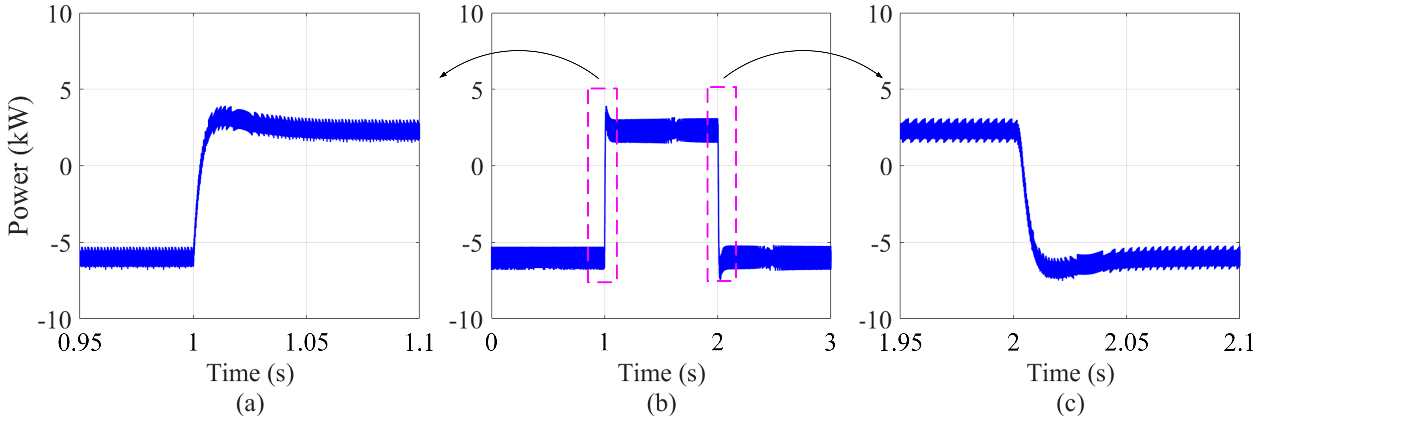

Figure 5.7: Power from the battery with conventional PI-based double-loop controller. (a) Zoomed-in results amid loading; (b) Power change; (c) Zoomed-in results amid de-loading.

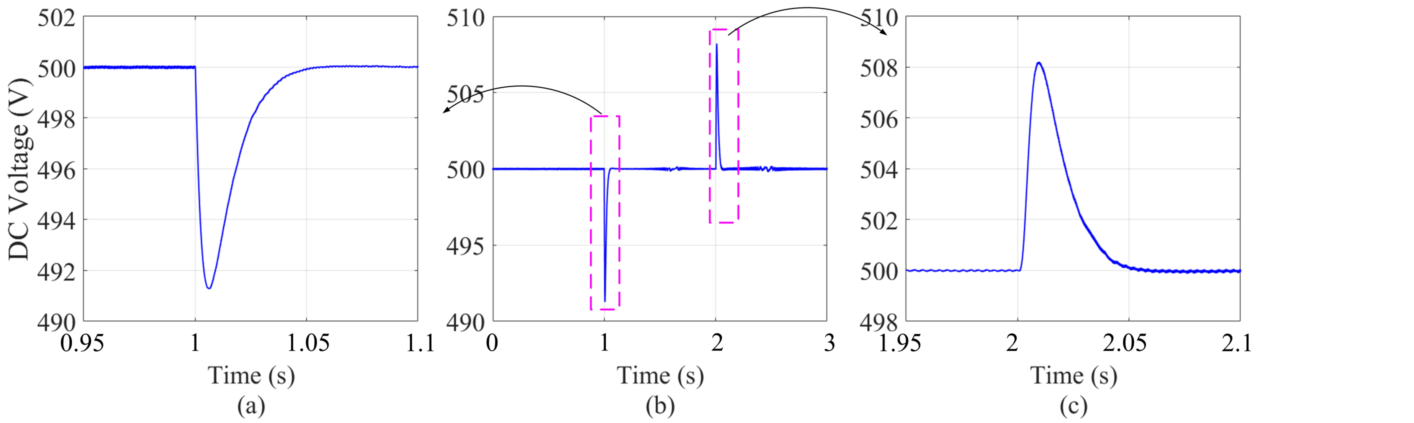

Figure 5.8: DC voltage with conventional PI-based double-loop controller. (a) Zoomed-in results amid loading; (b) DC voltage change; (c) Zoomed-in results amid de-loading.

the loads. At $1\,\mathrm{s}$ when load 2 is connected, all the added load is consumed by the increased power from the battery. Fluctuations can be seen in the battery power due to the internal characteristic of the battery model.

2. DC voltage: In Fig. 5.8, it is clear that the DC voltage dropped immediately after load 2 was connected at $1\,\mathrm{s}$ by around $8.2\,\mathrm{V}$ to the nadir, and it then raised back to $500\,\mathrm{V}$. The time period of this transient state was about $0.05\,\mathrm{s}$. During the period when Load 2 is disconnected, the DC voltage showed an opposite variation, but with nearly the same voltage difference.

Proposed ADRC-based voltage controller

Parameters of the ADRC-based voltage controller are shown in Table. 5.2. The DC voltage error gain K_{eso} is selected the same as K_{pvdc} to effectively evaluate the performance of the ADRC-based controller compared with the PI-based method. Relevant simulation results are shown in Figs. 5.9 and 5.10.

1. Battery power: In Fig. 5.9, the battery power shows a similar shape with that in Fig. 5.7, while the power response is much faster than that of system with PI-based voltage controller. This can also be seen in the DC voltage curves.

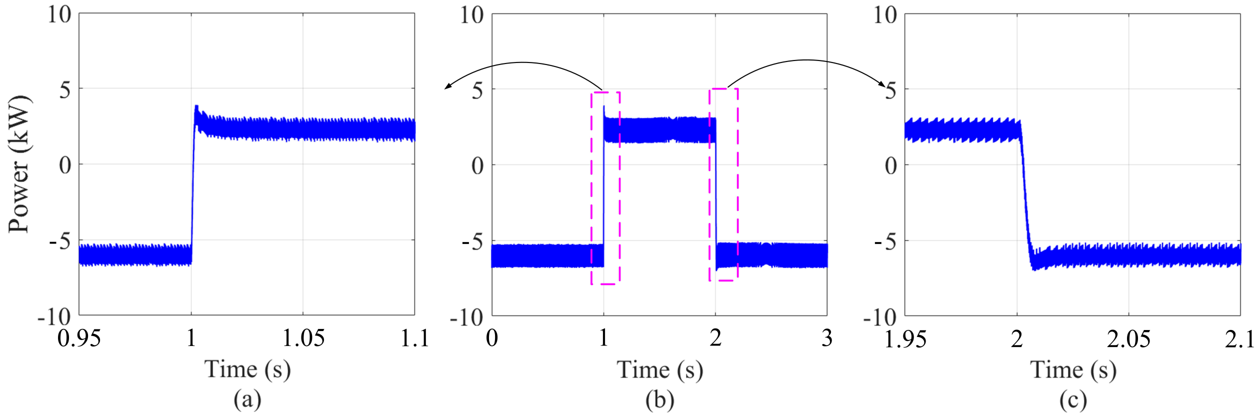

Figure 5.9: Power from the battery with ADRC-based double-loop controller. (a) Zoomed-in results amid loading; (b) Power change; (c) Zoomed-in results amid de-loading.

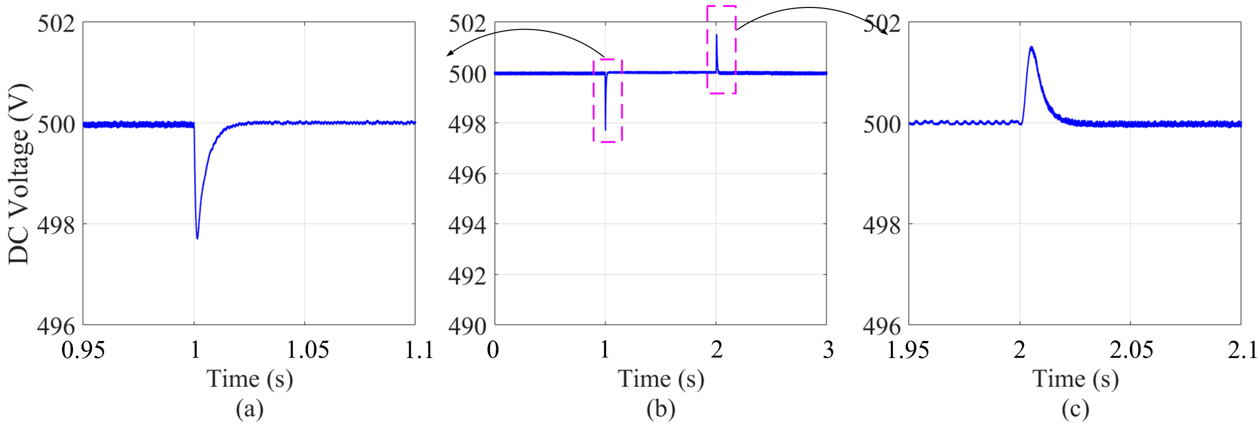

Figure 5.10: DC voltage with ADRC-based double-loop controller. (a) Zoomed-in results amid loading; (b) DC voltage change; (c) Zoomed-in results amid de-loading.

2. DC voltage: Fig. 5.10 shows that the voltage dropped immediately after Load 2 was connected at $1\,\mathrm{s}$ by around $2.1\,\mathrm{V}$ to the nadir, which is much smaller than that in Fig. 5.8. This transient state lasts only for about $0.02\,\mathrm{s}$ when the voltage returns to the original value, which is much shorter than that of using PI-based voltage controllers as well.

Above all, it can be concluded that the ADRC-based strategy is able to effectively control the power delivery between the battery and other power conversion units in the system as well as the DC voltage. A better transient performance of the PV-battery system is gained from the rejection of the total disturbance. The ADRC strategy is able to not only effectively control the power delivery between the battery and the system but also efficiently regulate the DC voltage after a large load change.

5.4 Summary

This chapter discusses the control strategy for the bidirectional DC/DC converter of the PV-battery system to provide FFR to the grid. An ADRC-based control scheme for BDC is proposed to improve the conventional PI-based double-loop controller. The scheme applies voltage-current double loop as the main control structure, and improves the power response and DC voltage regulation by observing and rejecting the total disturbance. The parameter selection method is discussed based on the stability analysis with root locus. Simulation results verify the effectiveness and the feasibility of the proposed control scheme in comparison with the conventional PI-based controller. A better performance with a faster power response and slighter voltage drop/rise during transients is achieved by adopting the ADRC scheme to the BDC.

Fast frequency response is believed to be a good choice for inertia support. However, FFR provided by battery storage depends on the measurement of the grid frequency, by which inverters act as controlled-current sources, as studied in this chapter. As discussed in Chapter 2, the frequency measurement such as a PLL introduces a non-negligible time delay in practical implementation. Consequently, the inertia provided by FFR is so-called synthetic inertia, not genuine inertia from synchronous generators. If prosumers were to become providers of genuine inertia, the integrated inverters need to work as voltage sources, which will be discussed in the next chapter.

Chapter 6

Inertia Support by Grid-forming prosumers based on Matching Approach

Chapter 5 discussed using prosumers' battery storage to provide fast frequency response (FFR) in order to improve the inertia of the system. Due to the responsiveness of power electronic converters, FFR can be activated much faster than primary frequency response, as explained in Chapter 2. However, the problem is that grid-following converters are integrated into the grid as controlled current sources. When the grid experiences a step load change, a grid-following converter needs to detect this load change by frequency measurement units such as a phase-locked loop (PLL) so that the converter can adjust its current output according to the measured load change. This inevitably introduces a time delay in the order of a few hundred milliseconds [210]. Therefore, FFR provided by grid-following converters is slower than inertial response because it cannot respond naturally to a disturbance due to the time delay introduced by the PLL. In addition, grid-following converters can only operate in a strong grid with a stiff frequency and voltage [23]. In a weak grid, such as microgrids with a large penetration of inverter-interfaced generation, the PLL used for grid synchronisation might fail to operate properly [142].

In comparison, by grid-forming control, the inverter acts as a voltage source, which responds naturally to the load change in the system. Grid-forming converters both improve the frequency response and enables synchronisation in a weak grid. The inertia can be improved by the inherent inertial response by these voltage-source-like converters. This is made possible by 'extracting' energy from the DC-link capacitor much like synchronous machines extract kinetic energy from rotating masses; this results in a natural inertial response compared to a synthetic one provided by FFR. Accordingly, the energy stored in the DC-link capacitor can be regarded as equivalent to the rotor of a synchronous generator that serves as immediate energy storage to the grid, and thereby the genuine inertia is improved. The issue is that this energy is limited, so it needs to be augmented by an additional energy source such as a battery or a supercapacitor. Against this backdrop, the emergence of prosumer-owned PV-battery systems offers a possibility to use batteries as inertia providers. Even though the capacity of residential batteries is relatively small, the combination of all grid-forming prosumers in the community serves as the source of sufficient energy supply.

6.1 Inertial response in a conventional power system

The inertial response in conventional power systems is performed by the physical inertia of the rotating parts of synchronous generators. Assume a conventional power system with n synchronous generators installed. The energy stored in the rotors of synchronous machines during steady state can be expressed as:

$$E = \frac{1}{2}J_1\omega_{\mathrm{g}}^2 + \frac{1}{2}J_2\omega_{\mathrm{g}}^2 + \cdots + \frac{1}{2}J_n\omega_{\mathrm{g}}^2 = \frac{1}{2}J\omega_{\mathrm{g}}^2, \tag{6.1}$$

where $J = J_1 + J_2 + \cdots + J_n$ is the system inertia and ω_{g} is the grid angular frequency. During the first instant of a contingency when the grid frequency drops from ω_{g} to ω, the energy difference required from the rotors is:

$$\Delta E = \frac{1}{2}J\omega_{\mathrm{g}}^2 - \frac{1}{2}J\omega^2 = \frac{1}{2}J(2\omega_{\mathrm{g}} - \Delta\omega)\Delta\omega, \tag{6.2}$$

where $\Delta\omega = \omega_{\mathrm{g}} - \omega$ is the frequency difference. As $\Delta\omega \ll 2\omega_{\mathrm{g}}$, (6.2) can be simplified as:

$$\Delta E = J\omega_{\mathrm{g}}\Delta\omega. \tag{6.3}$$

Observe in (6.3) that $\Delta\omega$ is small during the first instant of a transient state provided that J is sufficiently large, which highlights the importance of inertia.

With the penetration of inverter-interfaced renewable energy sources (RES) with no physical inertia, the number of synchronous generators is reduced to m. Thereby the inertial response is:

$$E = \frac{1}{2}J_1\omega_{\mathrm{g}}^2 + \cdots + \frac{1}{2}J_m\omega_{\mathrm{g}}^2 = \frac{1}{2}\hat{J}\omega_{\mathrm{g}}^2, \tag{6.4}$$

where $\hat{J}$ is the reduced inertia. As $\hat{J}$ is much smaller than J, distributed energy sources (DER) are expected to contribute to the compensation of the load variation. In this case, during the inertial response, the energy difference is expressed as:

$$\Delta E = \hat{J}\omega_{\mathrm{g}}\Delta\omega + \Delta E_{\mathrm{DER}}, \tag{6.5}$$

where ΔE_{DER} is the energy provided by DER. Hence, if ΔE_{DER} is instant and sufficient, the power difference is properly compensated, thus making $\hat{J}\omega_{\mathrm{g}}\Delta\omega \to 0$. Consequently, the system inertia is equivalently improved.

6.2 Inertia support by grid-forming prosumers based on matching control

6.2.1 Battery-based grid forming converter

The basic principle of the matching approach is explained in Chapter 2. This method establishes a link between the DC-link voltage and the rotor angular frequency. Frequency regulation can be realized by controlling the DC-link voltage. This can be understood as the DC-link voltage reducing to extract energy from the capacitor, such like the rotor decelerating to release energy. With battery storage augmenting the DC-link capacitor, the controller for the DC-side converter captures the change of the DC-link voltage which reflects the load disturbance from the grid. It then generates the desired battery-side current to adjust to the change in the voltage as a supplementary energy source for the DC-link capacitor. Proper control of the DC voltage helps regulate the frequency instantly, thus enhancing the inertial response. In this case, the conventional frequency droop method in controlling synchronous generators is adopted as the voltage droop in converters, which enables proper power sharing between paralleled converters.

The matching-approach-based controller for a battery storage has been explained in Chapter 3, in which the matching part is implemented in the inverter control, and the frequency regulation (which is translated into the DC voltage control problem) is realized in the battery charging controller in the form of $v_{\mathrm{dc}}/i_{\mathrm{bat}}$ droop controller. A detailed control diagram is shown in Fig. 3.13, which will not be pasted here. Such a grid-forming converter sourced by a single battery is referred to as a battery-based grid-forming converter (BGFC).

6.2.2 Simulation verification

The case study considers a typical residential microgrid with a diesel generator emulating the low-inertia grid, which is shown in Fig. 6.1. The microgrid model is built in Matlab/Simulink, which consists of the following components:

1. **A PV generator**. The PV-interfaced generation module consists of a PV array, a boost converter and an inverter. The DC-DC boost converter that connects the PV array to the DC bus is implemented with the MPPT algorithm; the DC/AC three-phase grid inverter is controlled in a *grid-following mode*.

2. **Battery-based grid-forming converters**. Two identical BGFCs are interfaced by adopting the proposed control scheme, in order to study the power sharing between them. All parameters in both BGFCs are the same. Both BGFCs are contributing to the inertial response and primary frequency control.

3. **A diesel generator**. A diesel-driven three-phase synchronous generator is implemented to emulate the low-inertia grid. The primary frequency control of the generator is disabled to see how the BGFCs help regulate the frequency. The generator, however, provides inertial response due to its inherent characteristic, which helps support the frequency in the first few seconds after a disturbance.

4. **Household loads**. Residential household loads are connected to the microgrid as power consumers. Each load is modelled as a constant impedance load. As we aim to focus on the inertia performance, only active loads are considered in this case. Even so, reactive power droop is applied in the voltage amplitude regulator as a more realistic control structure.

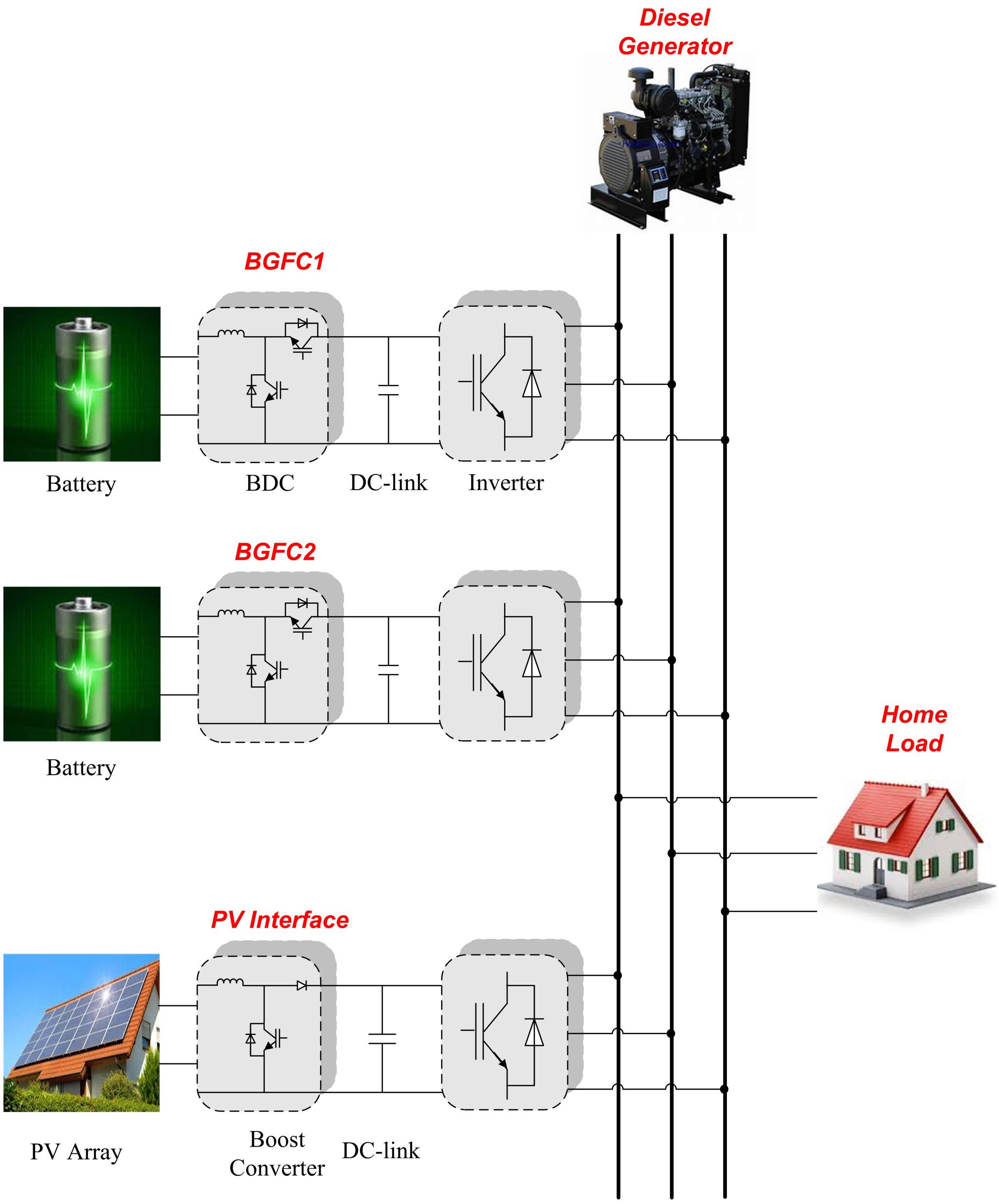

Figure 6.1: Residential microgrid test system.

The microgrid is initially supplied by a $400\,\mathrm{V}$, $50\,\mathrm{Hz}$, $60\,\mathrm{kW}$ three-phase diesel generator and the PV array providing, respectively $6\,\mathrm{kW}$, $9.4\,\mathrm{kW}$ (maximum) the $15\,\mathrm{kW}$ load. Two BGFCs serve as the backup power supply, so their power set-points are both zero. As a load disturbance, we increase the active power consumed by the household load. Load disturbance is imposed when the system has reached the steady state. The configuration and the relevant parameters of an individual BGFC are the same as the case in Chapter 3.

Simulation I: Increasing the load disturbance

In Simulation I, the system response to different levels of load disturbance is tested. The voltage droop coefficient is chosen as $m_{\mathrm{v}} = 1$.

Figs. 6.2-6.4 show the simulation results with the load increasing by $1.5\,\mathrm{kW}$, $3\,\mathrm{kW}$ and $6\,\mathrm{kW}$, respectively. Fig. 6.2 shows the power flow of each power unit. The PV module generates a constant

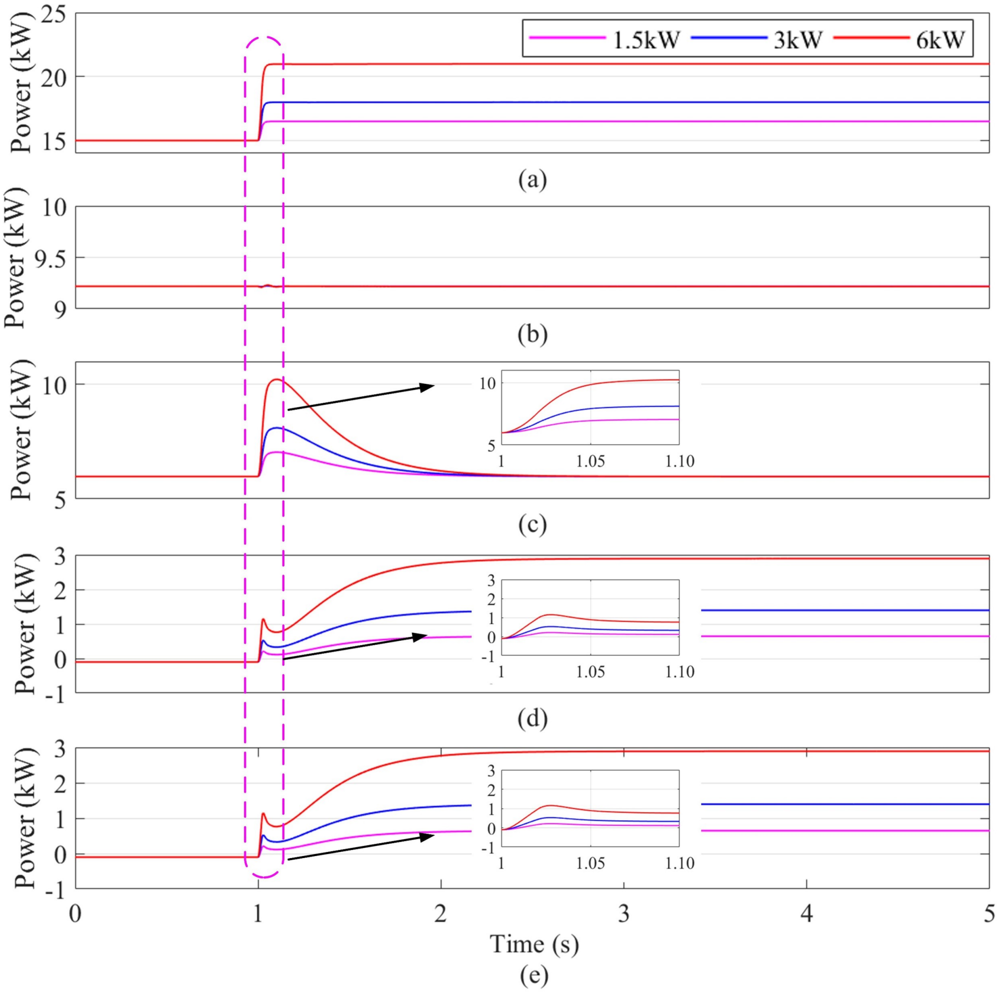

Figure 6.2: Power flows in Simulation I. (a) load power; (b) PV power; (c) diesel generator power; (d) BGFC1 power; (e) BGFC2 power.

power which reaches its maximum power point. As the sum of set-point powers of all units exceeds the amount of the load power, excessive power would flow to the batteries, which can be seen in Fig. 6.2 (d) and (e). That is why the power of BGFC 1 and 2 are negative. At $1\,\mathrm{s}$, the load change increases, which results in a power imbalance. From Fig. 6.2 (d) and (e), it can be seen that the BGFC powers increased rapidly at $1\,\mathrm{s}$, reaching the peak at $1.025\,\mathrm{s}$, and then dropped back until $1.1\,\mathrm{s}$. After that, the BGFC primary frequency control is activated, resulting in a steady increase of the power to compensate for the frequency deviation.

The diesel generator power (Fig. 6.2 (c)) increased smoothly at $1\,\mathrm{s}$ and reached its peak at $1.1\,\mathrm{s}$. Then it dropped back slowly to $6\,\mathrm{kW}$. The sudden increase in power from $1\,\mathrm{s}$ to $1.1\,\mathrm{s}$ is the inertial response provided by the generator. Observe that the inertial response of the batteries is shorter in duration due to the dominant inertial response of the diesel generator. As both BGFCs have identical controllers, they provide the same frequency support as illustrated in Figs. 6.2 (d) and (e).

By comparison, the PV generated power has an almost negligible oscillation at the first instants after the load change, going back to the original value soon. This oscillation has no contribution to the inertial response.

From Figs. 6.2 (c), (d), and (e), it is clear that with the increase of the load disturbance, the

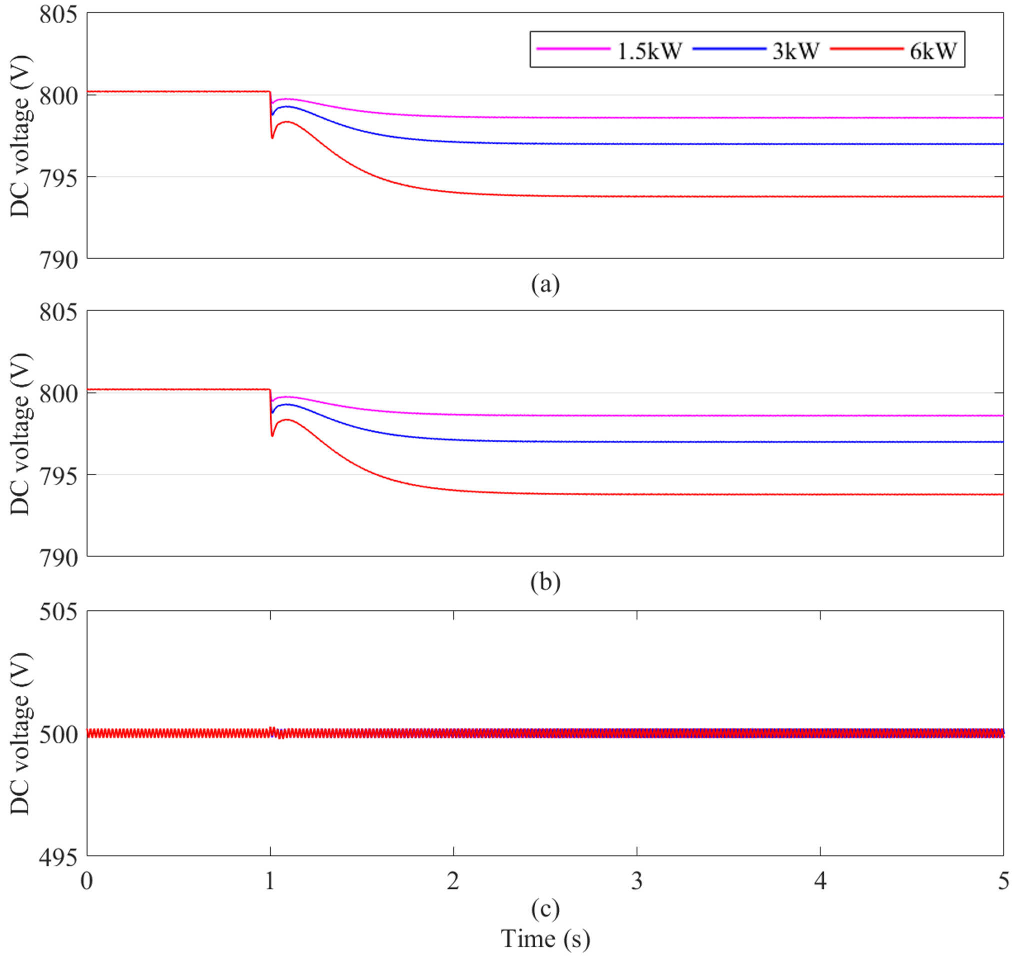

Figure 6.3: DC voltages of (a) BGFC1; (b) BFC2; (c) PV generation in Simulation I.

contributions on inertial response from the the diesel generator and BGFCs both increase. Dominant inertial response is provided by the diesel generator, while the contribution from the batteries can be adjusted by changing the voltage droop gain m_{v}, which will be discussed in Simulation II.

Fig. 6.3 shows the variations of the DC voltages in the BGFCs and the PV generation, which illustrates the difference between the grid-forming control (batteries) and grid-following control (PV). Observe that the DC-link voltage of the PV array is nearly constant during the load change, while BGFCs experienced a voltage drop due to the energy being released for frequency support. This results illustrate that the changing load is initially compensated by the grid-forming converters as they provide genuine inertia, the same as the diesel generator.

Fig. 6.4 shows the grid voltage and the grid frequency. It can be seen that the frequency stays stable at about $50.013\,\mathrm{Hz}$ and experiences a sudden drop at the first instant of the load change. The frequency then quickly recovers due to the combined inertial response from the diesel generator and the BGFCs, followed by a steady transition to the post-disturbance level of about $49.91\,\mathrm{Hz}$, $49.81\,\mathrm{Hz}$, and $49.61\,\mathrm{Hz}$ due to the action of droop control.

According to the results in Simulation I, it can be concluded that matching-based BGFCs provide genuine inertia to the system, like synchronous generators. They contribute to the inertial response instantly after the load disturbance, which helps enhance the system inertia. In Fig. 6.4, It is observed that the RoCoF is 1.72, 3.22, and $6.13\,\mathrm{Hz/s}$ corresponding to $1.5\,\mathrm{kW}$, $3\,\mathrm{kW}$ and $6\,\mathrm{kW}$ load change,

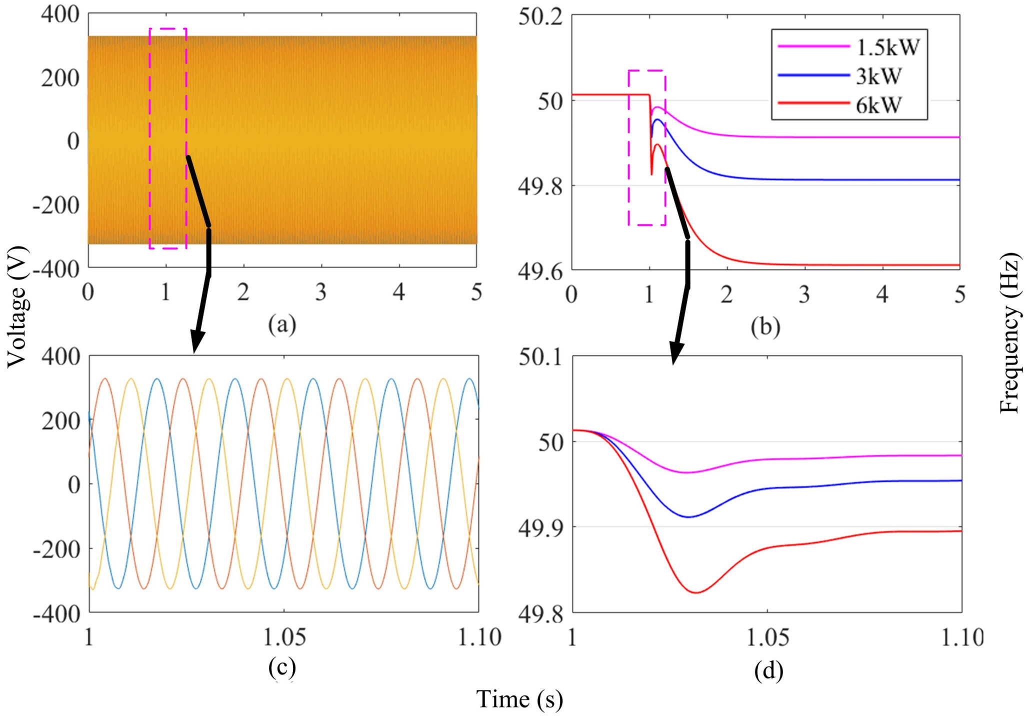

Figure 6.4: Grid voltage: (a) and (c); grid frequency: (b) and (d).

respectively. Such steep RoCoF is not allowed in a real power system. However, it can be decreased by further improving the inertia by the actions of parameter adjustment and higher penetration of BGFCs, and this will be discussed in Simulation II and III.

Simulation II: Increasing the voltage droop coefficient

The voltage droop coefficient m_{v} determines the power sharing and frequency deviation of the respective BGFCs. However, as the matching control makes the DC voltage equivalent to the output frequency, m_{v} also serves as a proportional gain of the DC-link voltage, which regulates the output DC current directly according to the voltage error resulted from load changes.

Fig. 6.5 shows the power flow and the frequency response of the system with $m_{\mathrm{v}} = 1, 4, 10$, respectively. The load increased by $6\,\mathrm{kW}$ at $1\,\mathrm{s}$. It can be seen that with the increase in the voltage droop coefficient, the frequency deviation decreases from $\Delta f = 0.19\,\mathrm{Hz}$ when $m_{\mathrm{v}} = 1$ to $\Delta f = 0.1\,\mathrm{Hz}$ when $m_{\mathrm{v}} = 10$. The RoCoF is thus decreased from $6.13\,\mathrm{Hz/s}$ to $3.70\,\mathrm{Hz/s}$. The results illustrate that a larger m_{v} helps improve the inertial response.

A notable change can be observed in the frequency nadir in Fig. 6.5 (d). Even though the frequency drop Δf decreases with the increase of m_{v}, the time period Δt during which the frequency drops to the nadir decreases as well. This can be explained by the fact that the droop coefficient m_{v} is also the proportional gain of the DC-link voltage error. A larger proportional gain results in a faster transient response. As the RoCoF is calculated by $\frac{\Delta f}{\Delta t}$, an decrease at both the denominator and the numerator might not necessarily reduce the RoCoF. So if the focus is on the frequency drop, it can be reduced by simply increasing m_{v}. Nevertheless, if the RoCoF is the focus, simply increasing m_{v} might not effectively reduce it in some cases.

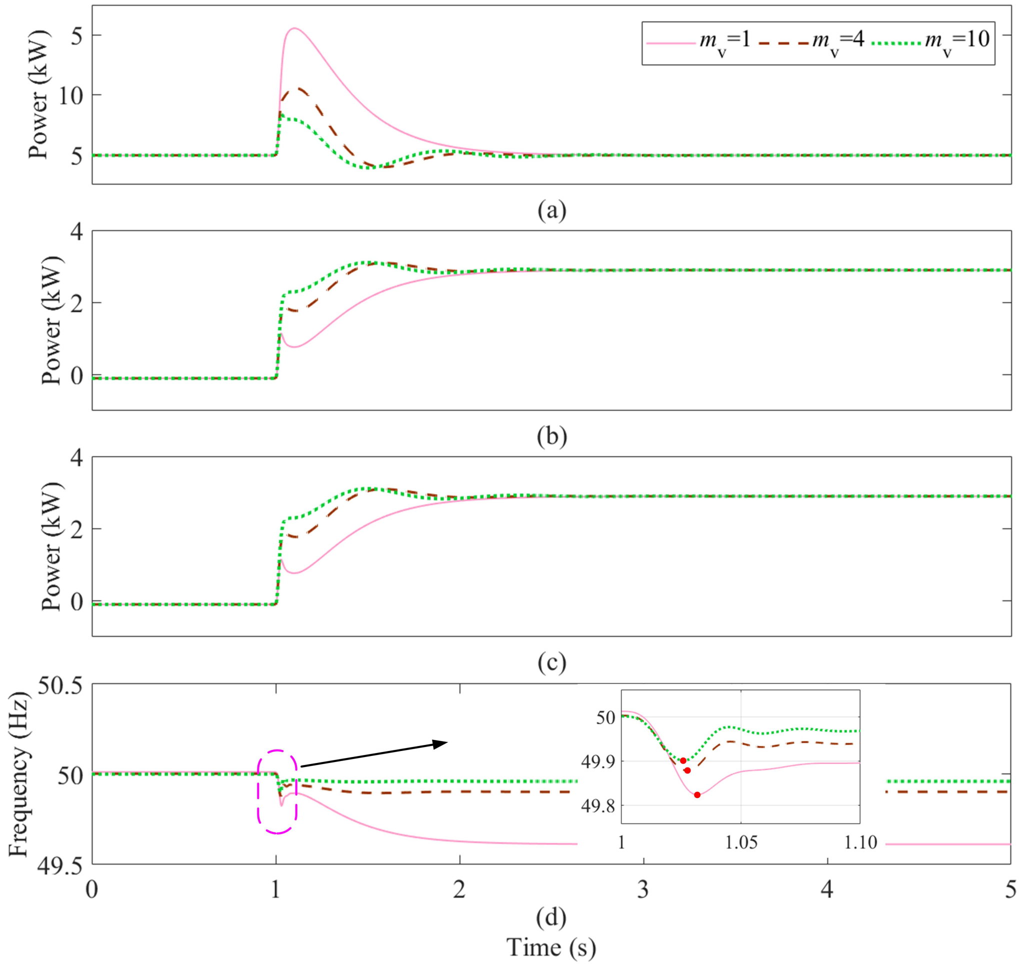

Figure 6.5: Results in Simulation II. (a) diesel generator power; (b) BGFC1 power; (c) BGFC2 power; (d) grid frequency.

In addition, note that this m_{v} is the droop coefficient of the $v_{\mathrm{dc}}/i_{\mathrm{bat}}$ droop control. Compared with typical P/f droop, this droop gain m_{v} is inversely proportional to the P/f droop gain m_{p}. According to the conclusion in Chapter 4, a too large value of m_{p} may result in instability. Hence, in the $v_{\mathrm{dc}}/i_{\mathrm{bat}}$ droop, stability can also be enhanced by properly increasing m_{v}. BGFCs with larger m_{v} generate more power during the transient state, which contribute more to the inertial response and the primary regulation of the frequency.

Simulation III: Increasing the number of BGFCs

Simulation I and II tested the system with two BGFCs, while real residential microgrids can be made up of many grid-forming prosumers. As more grid-forming converters are involved in contributing to the frequency regulation, more power can be provided during the transient state with the increasing number of BGFCs, thus enhancing the inertial response.

In Simulation III, the microgrid is expanded to systems with six and ten BGFCs, respectively. Fig. 6.6 shows the power flow and the frequency response of the system with two, six and ten BGFCs, respectively with $m_{\mathrm{v}} = 1$. The load increase is also set as $6\,\mathrm{kW}$. It can be seen that with the increase in the number of BGFCs, the frequency deviation decreases from $\Delta f = 0.1\,\mathrm{Hz}$ with six BGFCs to $\Delta f = 0.07\,\mathrm{Hz}$ with ten BGFCs. The RoCoF is thus decreased from $6.13\,\mathrm{Hz/s}$ to $2.26\,\mathrm{Hz/s}$. With the

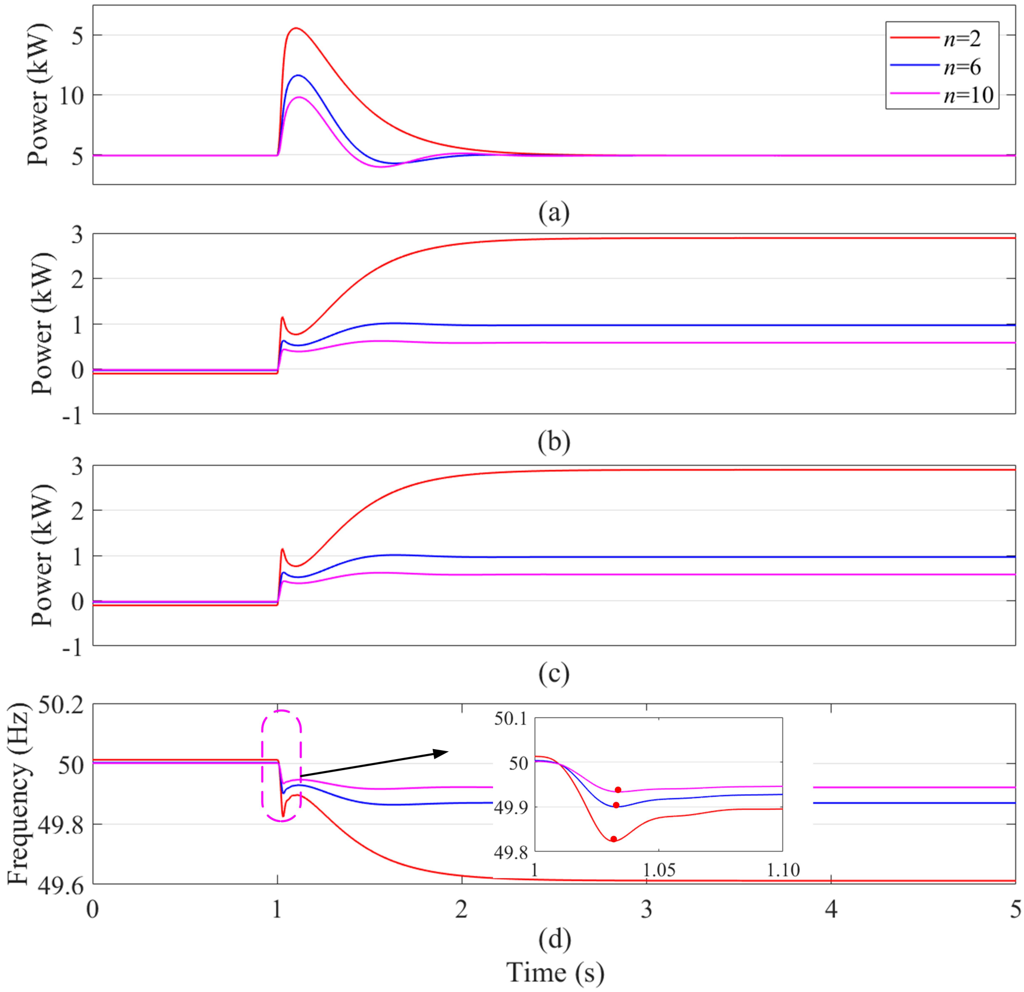

Figure 6.6: Results in Simulation III. (a) diesel generator power; (b) BGFC1 power; (c) BGFC2 power; (d) grid frequency.

increasing number of BGFCs, the inertial response can be further improved.

Furthermore, observe the frequency nadir in Fig. 6.5 (d) that Δf decreases with the increase of BGFCs, while Δt does not change much during this process. Hence, the RoCoF is directly reduced, which is different from the effect by increasing m_{v} as discussed in Simulation II. This is because more BGFCs are contributing to the inertial response, while the dynamic response of each voltage controller is not changed. More distributed power is provided by BGFCs.

Consequently, to improve the inertial response of the whole system, more BGFCs can be integrated, and m_{v} can be properly increased at the same time to meet the requirement of the RoCoF.

6.3 Adaptive voltage droop based on a piecewise power function

Section 6.2 shows that BGFCs controlled by matching control improve the system inertia by providing genuine inertial response. According to the results in Section 6.2.2-Simulation II, increasing the voltage droop gain m_{v} enhances the inertial response. As batteries have a fast response, they often serve as energy storage for the system instead of normal generation units. This means that batteries are not expected to be discharged normally during the steady state. In other words, they operate similar to slack buses in a conventional power system but with zero output power in steady state [84]. To

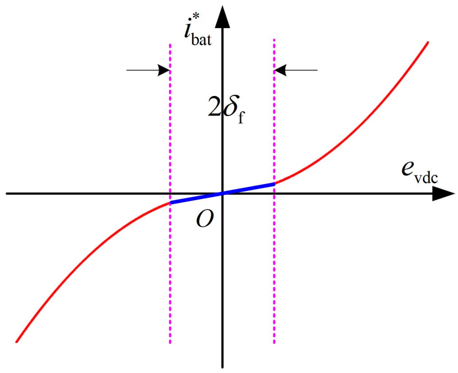

Figure 6.7: Characteristic curve of the piecewise function.

achieve this, m_{v} is expected to be small in steady state. This can be seen from the active power sharing relations (3.4):

$$m_{\mathrm{P1}}P_1 = m_{\mathrm{P2}}P_2 = \cdots = m_{\mathrm{P}n}P_n.$$

A higher power droop gain m_{P} results in a lower power output. As m_{v} is the droop gain of $v_{\mathrm{dc}}/i_{\mathrm{bat}}$ which is inversely proportional to m_{P}, it should be small in the steady state to lower the power output.

In this case, m_{v} is expected to be small in the steady state to achieve a small power output and to be large during the load change to provide sufficiently fast inertial response. [84] proposed a changing droop slope based on the output power change. The moment of demand variation is detected by comparing the real-time output power with the average power in last few time periods. Once the demand variation is detected, the droop gain for the energy storage systems (ESS) is changed by following an exponential equation. However, the measurement of power requires the measurement of AC voltages and currents. A low-pass filter is also needed to get the accurate power, as shown in Fig. 4.1 in Chapter 4, which inevitably introduces a time delay. The change of the droop gain might not be instantaneous. Comparatively, in matching control, a change in the power output is reflected instantly by the change in the DC voltage. Therefore, the droop gain can be adjusted adaptively based on the voltage change without detecting the demand variation by the measurement of AC quantities.

Based on this idea, the $v_{\mathrm{dc}}/i_{\mathrm{bat}}$ droop is modified by a piecewise power function expressed as

$$i^*_{\mathrm{bat}} = m_{\mathrm{v}} \cdot \begin{cases} \dfrac{e_{\mathrm{vdc}}}{\delta_{\mathrm{f}}^{1-\alpha_{\mathrm{f}}}}, & |e_{\mathrm{vdc}}| < \delta_{\mathrm{f}} \\ |e_{\mathrm{vdc}}|^{\alpha_{\mathrm{f}}} \cdot \mathrm{sign}(e_{\mathrm{vdc}}), & |e_{\mathrm{vdc}}| \geq \delta_{\mathrm{f}} \end{cases} \quad \text{s.t.} \quad i^{\min}_{\mathrm{bat}} < i^*_{\mathrm{bat}} < i^{\max}_{\mathrm{bat}}, \tag{6.6}$$

where $e_{\mathrm{vdc}} = v^*_{\mathrm{dc}} - v_{\mathrm{dc}}$, and $\alpha_{\mathrm{f}} > 1$. δ_{f} is selected based on the steady-state frequency deviation requirement.

Fig. 6.7 shows the characteristic curve of the function. During the steady state, the initial voltage error is very small, within $[-\delta_{\mathrm{f}}, \delta_{\mathrm{f}}]$. The adaptive droop controller operates in the linear region. The equivalent droop gain is reduced by the gain of $\frac{1}{\delta_{\mathrm{f}}^{1-\alpha_{\mathrm{f}}}}$ when $\delta_{\mathrm{f}} < 1$, performing a small power output. When the system experiences a step load change resulting in a relatively larger voltage difference, the adaptive droop controller reaches the nonlinear power function region. The equivalent droop gain can be calculated by the derivative of the curve. A larger voltage error gives a larger droop gain, which contributes more to the inertial response.

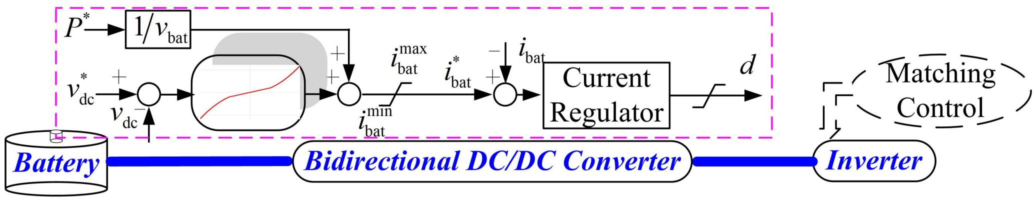

Figure 6.8: Control diagram of a single BGFC with the piecewise droop controller.

Table 6.1: Piecewise droop controller parameters

m_{v}	Constant droop gain	1
δ_{f}	Voltage error threshold	$0.3\,\mathrm{V}$
α_{f}	Power of the function	3

A simplified control diagram of a single BGFC with the piecewise droop controller is shown in Fig. 6.8.

6.3.1 Simulation verification

Simulations are carried out taking the same case as in Section 6.2. The step load change is still $6\,\mathrm{kW}$, applied to test the frequency response. The relevant parameters of the piecewise droop controller are shown in Table. 6.1.

Fig. 6.9 shows the power flow, DC voltages and frequency response of the system with a constant droop gain and a piecewise droop controller. It can be seen from Fig. 6.9 (a), (b) and (c) that BGFCs generate more power with the piecewise droop controller, contributing more to the inertial response. The voltage drops of the two BGFCs during the first instants after the disturbance are reduced from $2.9\,\mathrm{V}$ to $0.6\,\mathrm{V}$ by the effort of the piecewise droop, as can be seen from Fig. 6.9 (d), (e), while the maximum RoCoF is decreased from $6.13\,\mathrm{Hz/s}$ to $3.54\,\mathrm{Hz/s}$. Simulation results illustrate that with proper selection of δ_{f} and α_{f}, the piecewise droop controller can ensure the battery storage generates small amount of power in steady state while predominantly contributes to the inertial response during the demand variation.

Note that in Fig. 6.9 (a), the power from the diesel generator experience a more notable oscillation during the inertial response when the piecewise droop controller is applied. This illustrates that a too high voltage droop gain may result in power oscillation as large amount of power is provided instantly from the battery storage. Hence, the output of the piecewise droop controller should be limited by the maximum battery current as shown in Fig. 6.8.

6.4 Summary

This chapter argues that prosumer-owned batteries can be integrated into the grid by grid-forming control to provide genuine inertia. Compared with grid-following converters, batteries with grid-forming control respond naturally to a load change, as well as avoiding the time delay introduced by

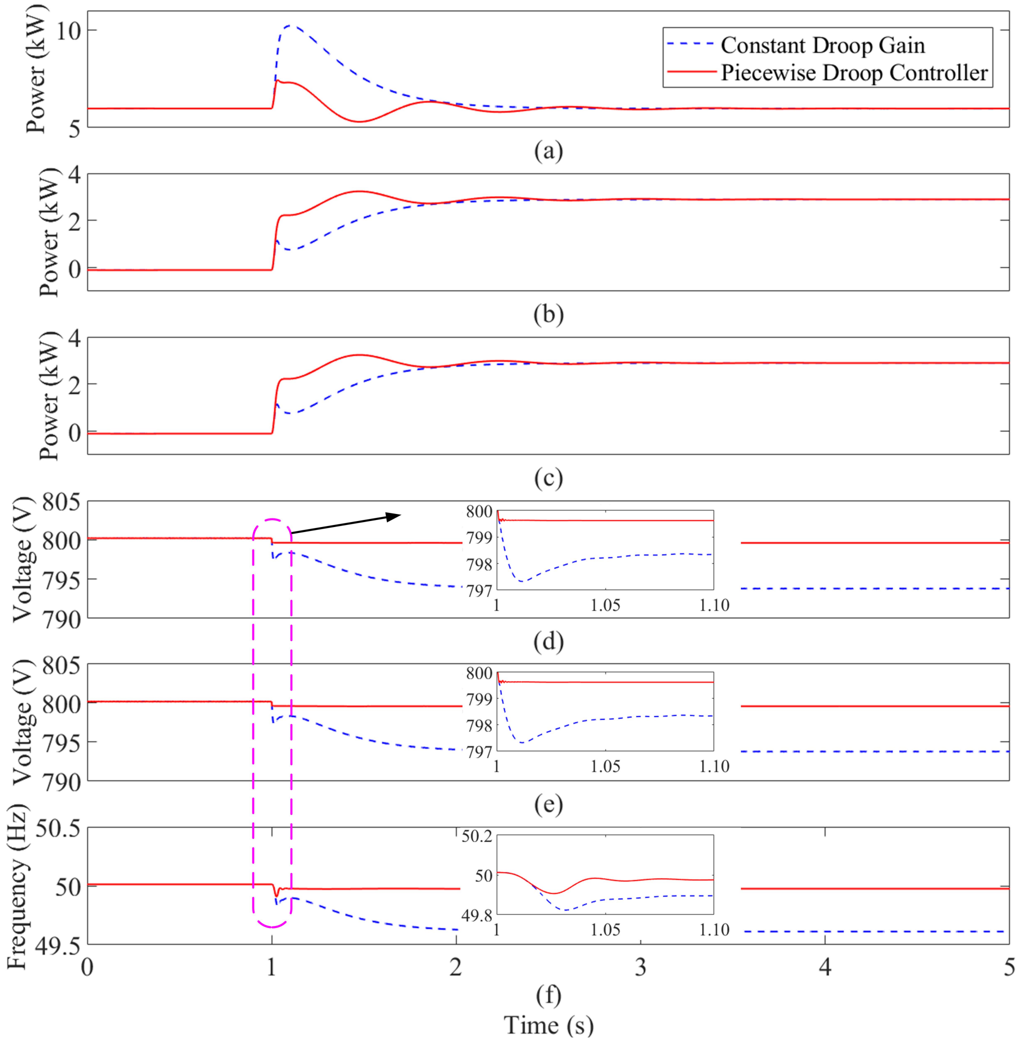

Figure 6.9: Results with the piecewise droop controller. (a) diesel generator power; (b) BGFC1 power; (c) BGFC2 power; (d) BGFC1 DC voltage; (e) BGFC2 DC voltage; (f) grid frequency.

PLLs. Hence we applied matching control to ensure inertial response after a contingency because matching control makes it easy to regulate the frequency by controlling the DC voltages. Furthermore, to ensure the batteries provide small amount of power in steady state while contributing dominantly during demand variation, a piecewise droop controller based on the DC voltage difference is proposed. The controller changes the droop gain adaptively based on the system conditions without depending on external signals.

Simulation results show that: 1) BGFCs contribute to the frequency regulation by genuine inertial response; 2) the inertial response can be improved by adjusting the droop coefficient in the DC voltage controller; 3) the RoCoF can be effectively reduced by a higher penetration of BGFCs; 4) the proposed piecewise droop controller ensures the battery storage generates a small amount of power in steady state while predominantly contributes to the inertial response during the demand variation. Batteries can thereby be rationally utilized for their better performance.

Chapter 7

Conclusion

The rise of prosumers creates the possibility to improve the performance of LV distribution networks. These prosumers, when integrated by grid-forming converters, improve the resiliency of the LV feeders as well as enhancing the inertial response by providing genuine inertia.

Residential microgrids supplied exclusively by residential prosumers can experience instability when the number of grid-forming converters increases. DC primary sources of prosumers with slow dynamic response may also cause instability problems.

Grid-forming converters, on the other hand, provide genuine inertia because of their voltage-source-like characteristics. Their inherent inertial response can be further improved by proper control strategies.

The present work firstly studies the stability of the residential microgrids, focusing on the separation from the main network. In particular, the impact of the integration of large numbers of grid-forming converters is further investigated. Second, this work proposes advanced controllers for the prosumer to provide fast frequency response (FFR), to enhance the emulated inertia for the whole system. As FFR provided by distributed energy resources (DER) requires a frequency measurement, which limits the behavior of the inertial response, grid-forming control is expected to make prosumers provide genuine inertia like voltage sources.

7.1 Summary of the results

Chapter 3 discusses control methods for grid-forming prosumers, including both the inverter control and the DC-stage control. The control methods consider not only three-phase connections, but also single-phase prosumers which is more realistic in practical residential microgrids. In addition, the chapter proposes a control strategy for hybrid PV-battery systems to support islanded operation of a residential microgrid based on matching with power sharing methods, which enables both maximum power point tracking (MPPT) and grid-forming functionality. Simulation results show that the PV can be considered as a constant power source injecting power to the system, while the battery storage performs frequency regulation.

Chapter 4 studies the stability of a LV distribution feeder operated as an islanded residential microgrid. The eigenvalue analysis for various cases has revealed that: 1) practically instability is caused with the increasing number of grid-forming inverters; 2) this instability is caused by a real eigenvalue which is sensitive to the microgrid expansion; 3) stability can be enhanced by adjusting the gains of the droop controller and the voltage controller; 4) primary energy source should have a sufficiently fast dynamic response to ensure stability.

Chapter 5 discusses the active disturbance rejection control (ADRC)-based control strategy for the bidirectional DC/DC converter (BDC) of the PV-battery system to provide FFR to the grid. The proposed controller applies voltage-current double loop as the main control structure to improve the power response and DC voltage regulation by observing and rejecting the total disturbance. Simulation results show a better performance in the ADRC-based controller, with a faster power response and a smaller voltage drop/rise during the transient state.

Chapter 6 applies prosumer-owned batteries integrated by matching control to provide genuine inertia. A piecewise droop controller based on the DC voltage difference is proposed to improve the performance of the battery-based grid-forming converter (BGFC). Simulation results show that: 1) BGFCs contribute to the frequency regulation by genuine inertial response; 2) the inertial response can be improved by adjusting the droop coefficient in the DC voltage controller; 3) the RoCoF can be effectively reduced by a higher penetration of BGFCs; 4) the proposed piecewise droop controller ensures the battery storage generates a small amount of power in the steady state while predominantly contributes to the inertial response during the demand variation.

7.2 Future work

Some areas relevant to this work require further investigation. The basic idea behind the work is to operate a LV feeder with a large number of grid-forming prosumers, while protection issues are not considered. Protection is tangential to the stability analysis of the resiential microgrid but needs further study to make the microgrid configuration practical. Economic aspects of the operation of LV distribution feeders as microgrid also require further research. As the DC side is hybrid by PV and batteries, the optimal energy management between PVs, batteries and the network remains areas of active research. The state of charge (SOC) of the battery should also be taken into consideration when designing the network, in order not to negatively influence the batteries' lifetime.

Moreover, when using the batteries controlled by grid-forming methods to enhance the inertia, batteries are assumed to have infinitely fast response, while in practice, the response time varies depending on the particular battery chemistry. This is crucial when the battery is used to augment the capacity of the DC-link capacitor for inertial response, which requires further investigations.

Bibliography

[1] A. Tayyebi, D. Groß, A. Anta, F. Kupzog, F. Dörfler, Frequency stability of synchronous machines and grid-forming power converters, IEEE Journal of Emerging and Selected Topics in Power Electronics 8 (2) (2020) 1004–1018.

[2] F. Milano, F. Dörfler, G. Hug, D. J. Hill, G. Verbič, Foundations and challenges of low-inertia systems, in: 2018 Power Systems Computation Conference (PSCC), IEEE, 2018.

[3] Clean Energy Council, Clean Energy Australia Report 2021, Tech. rep. (2021).

[4] Solar Choice, Solar panels cost data: Solar Choice Price Index | June 2021, Tech. rep.
URL `https://www.solarchoice.net.au/blog/solar-power-system-prices`

[5] A. C. Luna, N. L. Diaz, M. Graells, J. C. Vasquez, J. M. Guerrero, Cooperative energy management for a cluster of households prosumers, IEEE transactions on consumer electronics 62 (3) (2016) 235–242.

[6] Western Power, Study into the feasibility of a microgrid at Kalbarri, Tech. rep.
URL `bit.ly/3kh9kyg`

[7] R. Majumder, Some aspects of stability in microgrids, IEEE Transactions on power systems 28 (3) (2013) 3243–3252.

[8] N. Hatziargyriou, H. Asano, R. Iravani, C. Marnay, Microgrids, IEEE power and energy magazine 5 (4) (2007) 78–94.

[9] J. M. Guerrero, M. Chandorkar, T.-L. Lee, P. C. Loh, Advanced control architectures for intelligent microgrids—part i: Decentralized and hierarchical control, IEEE Transactions on Industrial Electronics 60 (4) (2012) 1254–1262.

[10] S. A. Raza, J. Jiang, A benchmark distribution system for investigation of residential microgrids with multiple local generation and storage devices, IEEE Open Access Journal of Power and Energy 7 (2019) 41–50.

[11] S. A. Raza, J. Jiang, Intra-and inter-phase power management and control of a residential microgrid at the distribution level, IEEE Transactions on Smart Grid 10 (6) (2019) 6839–6848.

[12] S. A. R. Naqvi, J. Jiang, Cooperative control and power management for islanded residential microgrids with local phase-wise generation and storage units, in: 2018 7th International Conference on Renewable Energy Research and Applications (ICRERA), IEEE, 2018, pp. 239–244.

[13] Q. Sun, J. Zhou, J. M. Guerrero, H. Zhang, Hybrid three-phase/single-phase microgrid architecture with power management capabilities, IEEE Transactions on Power Electronics 30 (10) (2014) 5964–5977.

[14] G. G. Talapur, H. M. Suryawanshi, L. Xu, A. B. Shitole, A reliable microgrid with seamless transition between grid connected and islanded mode for residential community with enhanced power quality, IEEE Transactions on Industry Applications 54 (5) (2018) 5246–5255.

[15] B. Singh, S. Kumar, Distributed incremental adaptive filter controlled grid interactive residential photovoltaic-battery based microgrid for rural electrification, IEEE Transactions on Industry Applications 56 (4) (2020) 4114–4123.

[16] M. Jafari, Z. Malekjamshidi, J. Zhu, M.-H. Khooban, A novel predictive fuzzy logic-based energy management system for grid-connected and off-grid operation of residential smart microgrids, IEEE Journal of Emerging and Selected Topics in Power Electronics 8 (2) (2018) 1391–1404.

[17] M. Jafari, Z. Malekjamshidi, D. D.-C. Lu, J. Zhu, Development of a fuzzy-logic-based energy management system for a multiport multioperation mode residential smart microgrid, IEEE Transactions on Power Electronics 34 (4) (2018) 3283–3301.

[18] V. A. Freire, L. V. R. De Arruda, C. Bordons, J. J. Márquez, Optimal demand response management of a residential microgrid using model predictive control, IEEE Access 8 (2020) 228264–228276.

[19] J. Guerrero, D. Gebbran, S. Mhanna, A. C. Chapman, G. Verbič, Towards a transactive energy system for integration of distributed energy resources : home energy management , distributed optimal power flow , and peer-to-peer energy trading, Renewable and Sustainable Energy Reviews (2020) 1–35.

[20] D. Azuatalam, K. Paridari, Y. Ma, M. Förstl, A. C. Chapman, G. Verbič, Energy management of small-scale PV-battery systems: A systematic review considering practical implementation, computational requirements, quality of input data and battery degradation, Renewable and Sustainable Energy Reviews 112 (2019) 555–570. doi:10.1016/J.RSER.2019.06.007.

[21] M. Alramlawi, P. Li, Design optimization of a residential pv-battery microgrid with a detailed battery lifetime estimation model, IEEE Transactions on Industry Applications 56 (2) (2020) 2020–2030. doi:10.1109/TIA.2020.2965894.

[22] J. Rocabert, A. Luna, F. Blaabjerg, P. Rodriguez, Control of power converters in ac microgrids, IEEE transactions on power electronics 27 (11) (2012) 4734–4749.

[23] A. Tayyebi, Z. Miletic, F. Dörfler, F. Kupzog, W. Hribernik, Gridforming converters–inevitability, control strategies and challenges in future grid applications, in: International Conference on Electricity Distribution (CIRED), 2018.

[24] C. Arghir, T. Jouini, F. Dorfler, Grid-forming control for power converters based on matching of synchronous machines, arXiv preprint arXiv:1706.09495 (2017).

[25] J. M. Guerrero, L. G. De Vicuna, J. Matas, M. Castilla, J. Miret, A wireless controller to enhance dynamic performance of parallel inverters in distributed generation systems, IEEE Transactions on power electronics 19 (5) (2004) 1205–1213.

[26] Y. A.-R. I. Mohamed, H. H. Zeineldin, M. Salama, R. Seethapathy, Seamless formation and robust control of distributed generation microgrids via direct voltage control and optimized dynamic power sharing, IEEE Transactions on Power Electronics 27 (3) (2011) 1283–1294.

[27] Y. A.-R. I. Mohamed, E. F. El-Saadany, Adaptive decentralized droop controller to preserve power sharing stability of paralleled inverters in distributed generation microgrids, IEEE Transactions on Power Electronics 23 (6) (2008) 2806–2816.

[28] Y. A.-R. I. Mohamed, A. A. Radwan, Hierarchical control system for robust microgrid operation and seamless mode transfer in active distribution systems, IEEE Transactions on Smart Grid 2 (2) (2011) 352–362.

[29] S.-J. Ahn, J.-W. Park, I.-Y. Chung, S.-I. Moon, S.-H. Kang, S.-R. Nam, Power-sharing method of multiple distributed generators considering control modes and configurations of a microgrid, IEEE Transactions on Power Delivery 25 (3) (2010) 2007–2016.

[30] G. Chen, E. Feng, Distributed secondary control and optimal power sharing in microgrids, IEEE/CAA Journal of Automatica Sinica 2 (3) (2015) 304–312.

[31] I. U. Nutkani, P. C. Loh, P. Wang, F. Blaabjerg, Linear decentralized power sharing schemes for economic operation of ac microgrids, IEEE Transactions on Industrial Electronics 63 (1) (2015) 225–234.

[32] J. M. Guerrero, L. G. De Vicuna, J. Matas, M. Castilla, J. Miret, Output impedance design of parallel-connected ups inverters with wireless load-sharing control, IEEE Transactions on industrial electronics 52 (4) (2005) 1126–1135.

[33] S. Tabatabaee, H. R. Karshenas, A. Bakhshai, P. Jain, Investigation of droop characteristics and x/r ratio on small-signal stability of autonomous microgrid, in: 2011 2nd Power Electronics, Drive Systems and Technologies Conference, IEEE, 2011, pp. 223–228.

[34] W. Yao, M. Chen, J. Matas, J. M. Guerrero, Z.-M. Qian, Design and analysis of the droop control method for parallel inverters considering the impact of the complex impedance on the power sharing, IEEE Transactions on Industrial Electronics 58 (2) (2010) 576–588.

[35] C. K. Sao, P. W. Lehn, Control and power management of converter fed microgrids, IEEE Transactions on Power Systems 23 (3) (2008) 1088–1098.

[36] M. Mao, Z. Dong, Y. Ding, L. Chang, A unified controller for a microgrid based on adaptive virtual impedance and conductance, in: 2014 IEEE Energy Conversion Congress and Exposition (ECCE), IEEE, 2014, pp. 695–701.

[37] K. De Brabandere, B. Bolsens, J. Van den Keybus, A. Woyte, J. Driesen, R. Belmans, A voltage and frequency droop control method for parallel inverters, IEEE Transactions on power electronics 22 (4) (2007) 1107–1115.

[38] S.-J. Chiang, C. Yen, K. Chang, A multimodule parallelable series-connected pwm voltage regulator, IEEE Transactions on Industrial Electronics 48 (3) (2001) 506–516.

[39] X. Yu, A. M. Khambadkone, H. Wang, S. T. S. Terence, Control of parallel-connected power converters for low-voltage microgrid—part i: A hybrid control architecture, IEEE Transactions on Power Electronics 25 (12) (2010) 2962–2970.

[40] D. M. Vilathgamuwa, P. C. Loh, Y. Li, Protection of microgrids during utility voltage sags, IEEE Transactions on Industrial Electronics 53 (5) (2006) 1427–1436.

[41] Y. Gu, W. Li, X. He, Frequency-coordinating virtual impedance for autonomous power management of dc microgrid, IEEE Transactions on Power Electronics 30 (4) (2014) 2328–2337.

[42] P. Sreekumar, V. Khadkikar, A new virtual harmonic impedance scheme for harmonic power sharing in an islanded microgrid, IEEE Transactions on Power Delivery 31 (3) (2015) 936–945.

[43] M. Savaghebi, Q. Shafiee, J. C. Vasquez, J. M. Guerrero, Adaptive virtual impedance scheme for selective compensation of voltage unbalance and harmonics in microgrids, in: 2015 IEEE Power & Energy Society General Meeting, IEEE, 2015, pp. 1–5.

[44] K. M. Cheema, A comprehensive review of virtual synchronous generator, International Journal of Electrical Power & Energy Systems 120 (2020) 106006.

[45] H.-P. Beck, R. Hesse, Virtual synchronous machine, in: Electrical Power Quality and Utilisation, 2007. EPQU 2007. 9th International Conference on, IEEE, 2007, pp. 1–6.

[46] K. Sakimoto, Y. Miura, T. Ise, Stabilization of a power system with a distributed generator by a virtual synchronous generator function, in: 8th International Conference on Power Electronics-ECCE Asia, IEEE, 2011, pp. 1498–1505.

[47] Y. Hirase, K. Abe, K. Sugimoto, Y. Shindo, A grid-connected inverter with virtual synchronous generator model of algebraic type, Electrical Engineering in Japan 184 (4) (2013) 10–21.

[48] Q.-C. Zhong, G. Weiss, Synchronverters: Inverters that mimic synchronous generators, IEEE Transactions on Industrial Electronics 58 (4) (2011) 1259–1267.

[49] Q.-C. Zhong, G. Weiss, Synchronverters: Inverters that mimic synchronous generators, IEEE transactions on industrial electronics 58 (4) (2010) 1259–1267.

[50] Q.-C. Zhong, Virtual synchronous machines: A unified interface for grid integration, IEEE Power Electronics Magazine 3 (4) (2016) 18–27.

[51] W. Li, H. Wang, Y. Jia, S. Yang, H. Liu, Frequency control strategy of grid-connected pv system using virtual synchronous generator, in: 2019 IEEE Innovative Smart Grid Technologies-Asia (ISGT Asia), IEEE, 2019, pp. 1618–1622.

[52] A. Karimi, Y. Khayat, M. Naderi, T. Dragičević, R. Mirzaei, F. Blaabjerg, H. Bevrani, Inertia response improvement in ac microgrids: A fuzzy-based virtual synchronous generator control, IEEE Transactions on Power Electronics 35 (4) (2019) 4321–4331.

[53] Y. Hirase, K. Abe, K. Sugimoto, K. Sakimoto, H. Bevrani, T. Ise, A novel control approach for virtual synchronous generators to suppress frequency and voltage fluctuations in microgrids, Applied Energy 210 (2018) 699–710.

[54] M. Ashabani, Y. A.-R. I. Mohamed, Integrating vscs to weak grids by nonlinear power damping controller with self-synchronization capability, IEEE Transactions on Power Systems 29 (2) (2013) 805–814.

[55] S. Y. Altahir, X. Yan, A. S. Gadaalla, New control scheme for virtual synchronous generators of different capacities, in: 2017 IEEE International Conference on Energy Internet (ICEI), IEEE, 2017, pp. 131–135.

[56] Z. Peng, J. Wang, D. Bi, Y. Dai, Y. Wen, The application of microgrids based on droop control with coupling compensation and inertia, IEEE Transactions on Sustainable Energy 9 (3) (2017) 1157–1168.

[57] J. Liu, Y. Miura, T. Ise, Comparison of dynamic characteristics between virtual synchronous generator and droop control in inverter-based distributed generators, IEEE Transactions on Power Electronics 31 (5) (2015) 3600–3611.

[58] T. Zheng, L. Chen, Y. Guo, S. Mei, Comprehensive control strategy of virtual synchronous generator under unbalanced voltage conditions, IET Generation, Transmission & Distribution 12 (7) (2018) 1621–1630.

[59] X. Zheng, C. Wang, S. Pang, Injecting positive-sequence current virtual synchronous generator control under unbalanced grid, IET Renewable Power Generation 13 (1) (2019) 165–170.

[60] M. Chen, X. Xiao, C. Yuan, S. Tao, Flexible power control of virtual synchronous generators under unbalanced grid voltage conditions, in: 2017 IEEE Energy Conversion Congress and Exposition (ECCE), IEEE, 2017, pp. 2881–2888.

[61] T. Jouini, C. Arghir, F. Dörfler, Grid-friendly matching of synchronous machines by tapping into the dc storage, IFAC-PapersOnLine 49 (22) (2016) 192–197.

[62] I. Cvetkovic, D. Boroyevich, R. Burgos, C. Li, M. Jaksic, P. Mattavelli, Modeling of a virtual synchronous machine-based grid-interface converter for renewable energy systems integration, in: Control and Modeling for Power Electronics (COMPEL), 2014 IEEE 15th Workshop on, IEEE, 2014, pp. 1–7.

[63] I. Cvetkovic, D. Boroyevich, R. Burgos, C. Li, P. Mattavelli, Modeling and control of grid-connected voltage-source converters emulating isotropic and anisotropic synchronous machines, in: Control and Modeling for Power Electronics (COMPEL), 2015 IEEE 16th Workshop on, IEEE, 2015, pp. 1–5.

[64] I. Cvetkovic, D. Boroyevich, R. Burgos, Y.-H. Hsieh, F. C. Lee, C. Li, P. Mattavelli, Experimental verification of a virtual synchronous generator control concept, in: Control and Modeling for Power Electronics (COMPEL), 2016 IEEE 17th Workshop on, IEEE, 2016, pp. 1–8.

[65] R. Teodorescu, F. Blaabjerg, M. Liserre, P. C. Loh, Proportional-resonant controllers and filters for grid-connected voltage-source converters, IEE Proceedings-Electric Power Applications 153 (5) (2006) 750–762.

[66] P. W. Sauer, M. A. Pai, Power system dynamics and stability, Vol. 101, Prentice hall Upper Saddle River, NJ, 1998.

[67] B. Wang, G. Verbič, W. Xiao, A. C. Chapman, Enhanced battery controller for inertia support in residential microgrid based on active disturbance rejection control, Electric Power Systems Research 189 (2020) 106646.

[68] C. Arghir, F. Dörfler, The electronic realization of synchronous machines: Model matching, angle tracking, and energy shaping techniques, IEEE Transactions on Power Electronics 35 (4) (2019) 4398–4410.

[69] J. W. Simpson-Porco, F. Dörfler, F. Bullo, Synchronization and power sharing for droop-controlled inverters in islanded microgrids, Automatica 49 (9) (2013) 2603–2611.

[70] F. Dorfler, F. Bullo, Synchronization and transient stability in power networks and nonuniform kuramoto oscillators, SIAM Journal on Control and Optimization 50 (3) (2012) 1616–1642.

[71] M. Colombino, D. Groß, J.-S. Brouillon, F. Dörfler, Global phase and magnitude synchronization of coupled oscillators with application to the control of grid-forming power inverters, IEEE Transactions on Automatic Control 64 (11) (2019) 4496–4511.

[72] H. One, Distributed generation technical interconnection requirements—interconnection at voltages 50 kv and below, Report, Toronto (2009).

[73] P. Kundur, J. Paserba, V. Ajjarapu, G. Andersson, A. Bose, C. Canizares, N. Hatziargyriou, D. Hill, A. Stankovic, C. Taylor, et al., Definition and classification of power system stability ieee/cigre joint task force on stability terms and definitions, IEEE transactions on Power Systems 19 (3) (2004) 1387–1401.

[74] Z. Shuai, Y. Sun, Z. J. Shen, W. Tian, C. Tu, Y. Li, X. Yin, Microgrid stability: Classification and a review, Renewable and Sustainable Energy Reviews 58 (2016) 167–179.

[75] M. Farrokhabadi, C. A. Cañizares, J. W. Simpson-Porco, E. Nasr, L. Fan, P. A. Mendoza-Araya, R. Tonkoski, U. Tamrakar, N. Hatziargyriou, D. Lagos, et al., Microgrid stability definitions, analysis, and examples, IEEE Transactions on Power Systems 35 (1) (2019) 13–29.

[76] P. Kundur, N. J. Balu, M. G. Lauby, Power system stability and control, Vol. 7, McGraw-hill New York, 1994.

[77] M. J. Gibbard, D. J. Vowles, P. Pourbeik, Small-signal stability, control and dynamic performance of power systems, University of Adelaide press, 2015.

[78] A. Elrayyah, Y. Sozer, M. Elbuluk, Simplified modeling procedure for inverter-based islanded microgrid, in: 2012 IEEE Energytech, IEEE, 2012, pp. 1–6.

[79] X. Tang, W. Deng, Z. Qi, Investigation of the dynamic stability of microgrid, IEEE Transactions on Power Systems 29 (2) (2013) 698–706.

[80] E. A. A. Coelho, P. C. Cortizo, P. F. D. Garcia, Small-signal stability for parallel-connected inverters in stand-alone ac supply systems, IEEE Transactions on Industry Applications 38 (2) (2002) 533–542.

[81] N. Pogaku, M. Prodanovic, T. C. Green, Modeling, analysis and testing of autonomous operation of an inverter-based microgrid, IEEE Transactions on power electronics 22 (2) (2007) 613–625.

[82] W. R. Issa, M. A. Abusara, S. M. Sharkh, Control of transient power during unintentional islanding of microgrids, IEEE Transactions on Power Electronics 30 (8) (2014) 4573–4584.

[83] L. Herrera, E. Inoa, F. Guo, J. Wang, H. Tang, Small-signal modeling and networked control of a phev charging facility, IEEE Transactions on Industry Applications 50 (2) (2013) 1121–1130.

[84] P. H. Divshali, A. Alimardani, S. H. Hosseinian, M. Abedi, Decentralized cooperative control strategy of microsources for stabilizing autonomous vsc-based microgrids, IEEE transactions on power systems 27 (4) (2012) 1949–1959.

[85] S. Samanta, N. R. Chaudhuri, On Stability Analysis of Power Grids with Synchronous Generators and Grid-Forming Converters under DC-side Current Limitation, arXiv (mar 2021). arXiv:2103.09966.
URL http://arxiv.org/abs/2103.09966

[86] R. O. Burnett, M. M. Butts, P. S. Sterlina, Power system applications for phasor measurement units, IEEE Computer Applications in Power 7 (1) (1994) 8–13.

[87] J. Sun, K. Karimi, Input impedance modeling of line-frequency rectifiers for aircraft power system stability analysis, IEEE Trans. Aerosp. Electron. Syst. 44 (1) (2008) 217–226.

[88] J. Sun, Input impedance analysis of single-phase pfc converters, IEEE Transactions on Power Electronics 20 (2) (2005) 308–314.

[89] J. Sun, K. J. Karimi, Small-signal input impedance modeling of multipulse rectifiers, Tech. rep., SAE Technical Paper (2008).

[90] I. Ray, Review of impedance-based analysis methods applied to grid-forming inverters in inverter-dominated grids, Energies 14 (9) (2021). doi:10.3390/en14092686.
URL https://www.mdpi.com/1996-1073/14/9/2686

[91] M. Amin, M. Molinas, Small-signal stability assessment of power electronics based power systems: A discussion of impedance- and eigenvalue-based methods, IEEE Transactions on Industry Applications 53 (5) (2017) 5014–5030. doi:10.1109/TIA.2017.2712692.

[92] J. Ma, X. Wang, X. Lan, Small-signal stability analysis of microgrid based on perturbation theory, in: 2012 Asia-Pacific Power and Energy Engineering Conference, IEEE, 2012, pp. 1–4.

[93] S. M. Amelian, R. Hooshmand, Small signal stability analysis of microgrids considering comprehensive load models-a sensitivity based approach, in: 2013 Smart Grid Conference (SGC), IEEE, 2013, pp. 143–149.

[94] M. Donnelly, J. Dagle, D. Trudnowski, G. Rogers, Impacts of the distributed utility on transmission system stability, IEEE Transactions on Power Systems 11 (2) (1996) 741–746.

[95] R. Majumder, B. Chaudhuri, A. Ghosh, R. Majumder, G. Ledwich, F. Zare, Improvement of stability and load sharing in an autonomous microgrid using supplementary droop control loop, IEEE transactions on power systems 25 (2) (2009) 796–808.

[96] S. P. Nandanoori, S. Kundu, W. Du, F. Tuffner, K. P. Schneider, Distributed small-signal stability conditions for inverter-based unbalanced microgrids, IEEE Transactions on Power Systems (2020).

[97] S. V. Iyer, M. N. Belur, M. C. Chandorkar, A generalized computational method to determine stability of a multi-inverter microgrid, IEEE Transactions on Power Electronics 25 (9) (2010) 2420–2432.

[98] A. Kahrobaeian, A.-R. M. Yasser, Stability analysis and control of medium-voltage micro-grids with dynamic loads, in: 2013 IEEE Power & Energy Society General Meeting, IEEE, 2013, pp. 1–5.

[99] A. K. Abbasi, M. W. B. Muatafa, A. S. B. Mokhtar, Small signal stability analysis of rectifier-inverter fed induction motor drive for microgrid applications, in: TENCON 2011-2011 IEEE Region 10 Conference, IEEE, 2011, pp. 1015–1019.

[100] G. Diaz, C. Gonzalez-Moran, J. Gomez-Aleixandre, A. Diez, Composite loads in stand-alone inverter-based microgrids—modeling procedure and effects on load margin, IEEE Transactions on Power Systems 25 (2) (2009) 894–905.

[101] A. Kahrobaeian, Y. A.-R. I. Mohamed, Analysis and mitigation of low-frequency instabilities in autonomous medium-voltage converter-based microgrids with dynamic loads, IEEE Transactions on Industrial Electronics 61 (4) (2013) 1643–1658.

[102] C. Rowe, T. Summers, R. Betz, D. Cornforth, Small signal stability analysis of arctan power frequency droop, in: 2011 IEEE Ninth International Conference on Power Electronics and Drive Systems, IEEE, 2011, pp. 787–792.

[103] H. Liang, B. J. Choi, W. Zhuang, X. Shen, Stability enhancement of decentralized inverter control through wireless communications in microgrids, IEEE Transactions on Smart Grid 4 (1) (2013) 321–331.

[104] C. N. Rowe, T. J. Summers, R. E. Betz, D. J. Cornforth, T. G. Moore, Arctan power–frequency droop for improved microgrid stability, IEEE transactions on power electronics 28 (8) (2012) 3747–3759.

[105] M. B. Delghavi, A. Yazdani, An adaptive feedforward compensation for stability enhancement in droop-controlled inverter-based microgrids, IEEE Transactions on Power Delivery 26 (3) (2011) 1764–1773.

[106] J. C. Vasquez, J. M. Guerrero, A. Luna, P. Rodríguez, R. Teodorescu, Adaptive droop control applied to voltage-source inverters operating in grid-connected and islanded modes, IEEE transactions on industrial electronics 56 (10) (2009) 4088–4096.

[107] A. Haddadi, A. Yazdani, G. Joos, B. Boulet, A gain-scheduled decoupling control strategy for enhanced transient performance and stability of an islanded active distribution network, IEEE transactions on power delivery 29 (2) (2013) 560–569.

[108] V. Calderaro, J. Milanovic, M. Kayikci, A. Piccolo, The impact of distributed synchronous generators on quality of electricity supply and transient stability of real distribution network, Electric Power Systems Research 79 (1) (2009) 134–143.

[109] L. Meegahapola, D. Flynn, Impact on transient and frequency stability for a power system at very high wind penetration, in: IEEE PES General Meeting, IEEE, 2010, pp. 1–8.

[110] M. Reza, D. Sudarmadi, F. Viawan, W. Kling, L. van der Sluis, Dynamic stability of power systems with power electronic interfaced dg, in: 2006 IEEE PES Power Systems Conference and Exposition, 2006, pp. 1423–1428. doi:10.1109/PSCE.2006.296510.

[111] A. K. Srivastava, A. A. Kumar, N. N. Schulz, Impact of distributed generations with energy storage devices on the electric grid, IEEE Systems Journal 6 (1) (2012) 110–117. doi:10.1109/JSYST.2011.2163013.

[112] D. Khani, A. Sadeghi Yazdankhah, H. Madadi Kojabadi, Impacts of distributed generations on power system transient and voltage stability, International Journal of Electrical Power Energy Systems 43 (1) (2012) 488–500. doi:https://doi.org/10.1016/j.ijepes.2012.06.007.
URL https://www.sciencedirect.com/science/article/pii/S0142061512002694

[113] H. Kobayashi, Fault ride through requirements and measures of distributed pv systems in japan, in: 2012 IEEE Power and Energy Society General Meeting, 2012, pp. 1–6. doi:10.1109/PESGM.2012.6345319.

[114] B. Tamimi, C. Cañizares, K. Bhattacharya, System stability impact of large-scale and distributed solar photovoltaic generation: The case of ontario, canada, IEEE Transactions on Sustainable Energy 4 (3) (2013) 680–688. doi:10.1109/TSTE.2012.2235151.

[115] D. Hall, R. Colclaser, Transient modeling and simulation of a tubular solid oxide fuel cell, IEEE Transactions on Energy Conversion 14 (3) (1999) 749–753. doi:10.1109/60.790946.

[116] K. Sedghisigarchi, A. Feliachi, Dynamic and transient analysis of power distribution systems with fuel cells-part i: fuel-cell dynamic model, IEEE Transactions on Energy Conversion 19 (2) (2004) 423–428. doi:10.1109/TEC.2004.827039.

[117] K. Sedghisigarchi, A. Feliachi, Dynamic and transient analysis of power distribution systems with fuel cells-part ii: control and stability enhancement, IEEE Transactions on Energy Conversion 19 (2) (2004) 429–434. doi:10.1109/TEC.2003.822302.

[118] Q. Ai, X. Wang, X. He, The impact of large-scale distributed generation on power grid and microgrids, Renewable Energy 62 (2014) 417–423. doi:https://doi.org/10.1016/j.renene.2013.07.032.
URL https://www.sciencedirect.com/science/article/pii/S096014811300387X

[119] I. Xyngi, A. Ishchenko, M. Popov, L. van der Sluis, Transient stability analysis of a distribution network with distributed generators, IEEE Transactions on Power Systems 24 (2) (2009) 1102–1104. doi:10.1109/TPWRS.2008.2012280.

[120] N. Soni, S. Doolla, M. C. Chandorkar, Improvement of transient response in microgrids using virtual inertia, IEEE Transactions on Power Delivery 28 (3) (2013) 1830–1838. doi:10.1109/TPWRD.2013.2264738.

[121] M. A. Zamani, A. Yazdani, T. S. Sidhu, A control strategy for enhanced operation of inverter-based microgrids under transient disturbances and network faults, IEEE Transactions on Power Delivery 27 (4) (2012) 1737–1747. doi:10.1109/TPWRD.2012.2205713.

[122] R. S. Al Abri, E. F. El-Saadany, Y. M. Atwa, Optimal placement and sizing method to improve the voltage stability margin in a distribution system using distributed generation, IEEE Transactions on Power Systems 28 (1) (2013) 326–334. doi:10.1109/TPWRS.2012.2200049.

[123] M. Aman, G. Jasmon, H. Mokhlis, A. Bakar, Optimal placement and sizing of a dg based on a new power stability index and line losses, International Journal of Electrical Power Energy Systems 43 (1) (2012) 1296–1304. doi:https://doi.org/10.1016/j.ijepes.2012.05.053.
URL https://www.sciencedirect.com/science/article/pii/S0142061512002438

[124] A. Al-Hinai, K. Sedhisigarchi, A. Feliachi, Stability enhancement of a distribution network comprising a fuel cell and a microturbine, in: IEEE Power Engineering Society General Meeting, 2004., 2004, pp. 2156–2161 Vol.2. doi:10.1109/PES.2004.1373262.

[125] Y.-Y. Hong, M.-C. Hsiao, Y.-R. Chang, Y.-D. Lee, H.-C. Huang, Multiscenario underfrequency load shedding in a microgrid consisting of intermittent renewables, IEEE Transactions on Power Delivery 28 (3) (2013) 1610–1617. doi:10.1109/TPWRD.2013.2254502.

[126] D. Guezgouz, D. E. Chariag, Y. Raingeaud, J.-C. Le Bunetel, Modeling of electromagnetic interference and plc transmission for loads shedding in a microgrid, IEEE Transactions on Power Electronics 26 (3) (2011) 747–754. doi:10.1109/TPEL.2010.2097608.

[127] W. Uijlings, D. Street, S. London, An independent analysis on the ability of generators to ride through rate of change of frequency values up to 2hz/s, EirGrid, London, UK, Rep 16010927 (2013).

[128] J. Morren, S. W. De Haan, W. L. Kling, J. Ferreira, Wind turbines emulating inertia and supporting primary frequency control, IEEE Transactions on power systems 21 (1) (2006) 433–434.

[129] M. Kayikçi, J. V. Milanovic, Dynamic contribution of dfig-based wind plants to system frequency disturbances, IEEE Transactions on Power Systems 24 (2) (2009) 859–867.

[130] J. F. Conroy, R. Watson, Frequency response capability of full converter wind turbine generators in comparison to conventional generation, IEEE transactions on power systems 23 (2) (2008) 649–656.

[131] M. F. M. Arani, Y. A.-R. I. Mohamed, Analysis and damping of mechanical resonance of wind power generators contributing to frequency regulation, IEEE Transactions on Power Systems 32 (4) (2016) 3195–3204.

[132] N. Kakimoto, S. Takayama, H. Satoh, K. Nakamura, Power modulation of photovoltaic generator for frequency control of power system, IEEE Transactions on Energy Conversion 24 (4) (2009) 943–949.

[133] A. F. Hoke, M. Shirazi, S. Chakraborty, E. Muljadi, D. Maksimovic, Rapid active power control of photovoltaic systems for grid frequency support, IEEE Journal of Emerging and Selected Topics in Power Electronics 5 (3) (2017) 1154–1163.

[134] J. Fang, Y. Tang, H. Li, X. Li, A battery/ultracapacitor hybrid energy storage system for implementing the power management of virtual synchronous generators, IEEE Transactions on Power Electronics 33 (4) (2017) 2820–2824.

[135] L. A. Lopes, et al., Self-tuning virtual synchronous machine: A control strategy for energy storage systems to support dynamic frequency control, IEEE Transactions on Energy Conversion 29 (4) (2014) 833–840.

[136] D. Li, Q. Zhu, S. Lin, X. Bian, A self-adaptive inertia and damping combination control of vsg to support frequency stability, IEEE Transactions on Energy Conversion 32 (1) (2016) 397–398.

[137] J. Zhu, C. D. Booth, G. P. Adam, A. J. Roscoe, C. G. Bright, Inertia emulation control strategy for vsc-hvdc transmission systems, IEEE Transactions on Power Systems 28 (2) (2012) 1277–1287.

[138] J. Renedo, A. Garcı, L. Rouco, et al., Active power control strategies for transient stability enhancement of ac/dc grids with vsc-hvdc multi-terminal systems, IEEE Transactions on Power Systems 31 (6) (2016) 4595–4604.

[139] L. Huang, H. Xin, Z. Wang, K. Wu, H. Wang, J. Hu, C. Lu, A virtual synchronous control for voltage-source converters utilizing dynamics of dc-link capacitor to realize self-synchronization, IEEE Journal of Emerging and Selected Topics in Power Electronics 5 (4) (2017) 1565–1577.

[140] J. Fang, H. Li, Y. Tang, F. Blaabjerg, Distributed power system virtual inertia implemented by grid-connected power converters, IEEE Transactions on Power Electronics 33 (10) (2017) 8488–8499.

[141] Á. Navarro-Rodríguez, P. García, R. Georgious, J. García, S. Saeed, Observer-based transient frequency drift compensation in ac microgrids, IEEE Transactions on Smart Grid 10 (2) (2017) 2015–2025.

[142] Y. Khayat, S. Golestan, J. M. Guerrero, J. C. Vasquez, H. Bevrani, Dc-link voltage control aided for the inertial support during severe faults in weak grids, IEEE Journal of Emerging and Selected Topics in Power Electronics (2020).

[143] M. Ghazavidozein, O. Gomis-Bellmunt, P. Mancarella, Simultaneous provision of dynamic active and reactive power response from utility-scale battery energy storage systems in weak grids, IEEE Transactions on Power Systems (2021).

[144] D. Dong, B. Wen, D. Boroyevich, P. Mattavelli, Y. Xue, Analysis of phase-locked loop low-frequency stability in three-phase grid-connected power converters considering impedance interactions, IEEE Transactions on Industrial Electronics 62 (1) (2014) 310–321.

[145] S. Ma, H. Geng, L. Liu, G. Yang, B. C. Pal, Grid-synchronization stability improvement of large scale wind farm during severe grid fault, IEEE Transactions on Power Systems 33 (1) (2017) 216–226.

[146] J. Fang, R. Zhang, H. Li, Y. Tang, Frequency derivative-based inertia enhancement by grid-connected power converters with a frequency-locked-loop, IEEE Transactions on Smart Grid 10 (5) (2018) 4918–4927.

[147] AEMO, Application of Advanced Grid-scale Inverters in the NEM Important notice, Tech. Rep. August (2021).

[148] J. Zhao, D. Shi, R. Sharma, C. Wang, Microgrid reactive power management during and subsequent to islanding process, in: 2014 IEEE PES T D Conference and Exposition, 2014, pp. 1–5. doi:10.1109/TDC.2014.6863367.

[149] B. V. Solanki, C. A. Cañizares, K. Bhattacharya, Practical energy management systems for isolated microgrids, IEEE Transactions on Smart Grid 10 (5) (2019) 4762–4775. doi:10.1109/TSG.2018.2868130.

[150] M. N. Ambia, A. Al-Durra, C. Caruana, S. Muyeen, Stability enhancement of a hybrid micro-grid system in grid fault condition, in: 2012 15th International Conference on Electrical Machines and Systems (ICEMS), 2012, pp. 1–6.

[151] R. Majumder, A. Ghosh, G. Ledwich, F. Zare, Power sharing and stability enhancement of an autonomous microgrid with inertial and non-inertial dgs with dstatcom, in: 2009 International Conference on Power Systems, 2009, pp. 1–6. doi:10.1109/ICPWS.2009.5442666.

[152] Y. W. Li, C.-N. Kao, An accurate power control strategy for power-electronics-interfaced distributed generation units operating in a low-voltage multibus microgrid, IEEE Transactions on Power Electronics 24 (12) (2009) 2977–2988. doi:10.1109/TPEL.2009.2022828.

[153] H. Mahmood, D. Michaelson, J. Jiang, Reactive power sharing in islanded microgrids using adaptive voltage droop control, IEEE Transactions on Smart Grid 6 (6) (2015) 3052–3060. doi:10.1109/TSG.2015.2399232.

[154] J. He, Y. W. Li, F. Blaabjerg, An enhanced islanding microgrid reactive power, imbalance power, and harmonic power sharing scheme, IEEE Transactions on Power Electronics 30 (6) (2015) 3389–3401. doi:10.1109/TPEL.2014.2332998.

[155] J. Schiffer, T. Seel, J. Raisch, T. Sezi, Voltage stability and reactive power sharing in inverter-based microgrids with consensus-based distributed voltage control, IEEE Transactions on Control Systems Technology 24 (1) (2016) 96–109. doi:10.1109/TCST.2015.2420622.

[156] J. W. Simpson-Porco, Q. Shafiee, F. Dörfler, J. C. Vasquez, J. M. Guerrero, F. Bullo, Secondary frequency and voltage control of islanded microgrids via distributed averaging, IEEE Transactions on Industrial Electronics 62 (11) (2015) 7025–7038. doi:10.1109/TIE.2015.2436879.

[157] A. Milczarek, M. Malinowski, J. M. Guerrero, Reactive power management in islanded microgrid—proportional power sharing in hierarchical droop control, IEEE Transactions on Smart Grid 6 (4) (2015) 1631–1638. doi:10.1109/TSG.2015.2396639.

[158] N. Hatziargyriou, J. Milanovic, C. Rahmann, V. Ajjarapu, C. Canizares, I. Erlich, D. Hill, I. Hiskens, I. Kamwa, B. Pal, P. Pourbeik, J. Sanchez-Gasca, A. Stankovic, T. Van Cutsem, V. Vittal, C. Vournas, Definition and classification of power system stability – revisited amp; extended, IEEE Transactions on Power Systems 36 (4) (2021) 3271–3281. doi:10.1109/TPWRS.2020.3041774.

[159] E. V. Larsen, Wind generators and series-compensated ac transmission lines, in: 2012 IEEE Power and Energy Society General Meeting, 2012, pp. 1–4. doi:10.1109/PESGM.2012.6344581.

[160] Y. Song, D. J. Hill, T. Liu, Impact of dg connection topology on the stability of inverter-based microgrids, IEEE Transactions on Power Systems 34 (5) (2019) 3970–3972.

[161] E. Barklund, N. Pogaku, M. Prodanovic, C. Hernandez-Aramburo, T. C. Green, Energy management in autonomous microgrid using stability-constrained droop control of inverters, IEEE Transactions on Power Electronics 23 (5) (2008) 2346–2352.

[162] W. Du, Z. Chen, K. P. Schneider, R. H. Lasseter, S. P. Nandanoori, F. K. Tuffner, S. Kundu, A comparative study of two widely used grid-forming droop controls on microgrid small-signal stability, IEEE Journal of Emerging and Selected Topics in Power Electronics 8 (2) (2019) 963–975.

[163] M. Liserre, F. Blaabjerg, S. Hansen, Design and control of an lcl-filter-based three-phase active rectifier, Industry Applications, IEEE Transactions on 41 (2005) 1281 – 1291. doi:10.1109/TIA.2005.853373.

[164] R. N. Beres, X. Wang, M. Liserre, F. Blaabjerg, C. L. Bak, A review of passive power filters for three-phase grid-connected voltage-source converters, IEEE Journal of Emerging and Selected Topics in Power Electronics 4 (1) (2016) 54–69. doi:10.1109/JESTPE.2015.2507203.

[165] R. Peña-Alzola, F. Blaabjerg, Chapter 8 - Design and Control of Voltage Source Converters With LCL-Filters, Elsevier Inc, 2018.

[166] A. C. Z. de Souza, M. Castilla, Microgrids design and implementation, Springer, 2019.

[167] L. F. A. Pereira, A. S. Bazanella, Tuning rules for proportional resonant controllers, IEEE Transactions on Control Systems Technology 23 (5) (2015) 2010–2017.

[168] R. A. Mastromauro, M. Liserre, A. Dell'Aquila, Control issues in single-stage photovoltaic systems: Mppt, current and voltage control, IEEE Transactions on Industrial Informatics 8 (2) (2012) 241–254.

[169] A. Kulkarni, V. John, Mitigation of lower order harmonics in a grid-connected single-phase pv inverter, IEEE transactions on power electronics 28 (11) (2013) 5024–5037.

[170] Y. Liao, Z. Liu, H. Zhang, B. Wen, Low-frequency stability analysis of single-phase system with dq-frame impedance approach—part i: Impedance modeling and verification, IEEE Transactions on Industry Applications 54 (5) (2018) 4999–5011.

[171] S. Golestan, J. M. Guerrero, J. C. Vasquez, Single-phase plls: A review of recent advances, IEEE Transactions on Power Electronics 32 (12) (2017) 9013–9030.

[172] W. Xiao, Photovoltaic power system: modeling, design, and control, John Wiley & Sons, 2017.

[173] D. Gebbran, S. Mhanna, Y. Ma, A. C. Chapman, G. Verbič, Fair coordination of distributed energy resources with volt-var control and pv curtailment, Applied Energy 286 (2021) 116546. doi:https://doi.org/10.1016/j.apenergy.2021.116546.
URL https://www.sciencedirect.com/science/article/pii/S0306261921000933

[174] International Energy Agency (IEA), Digitalization & Energy, Tech. rep. (2017).

[175] P. Graham, L. Havas, T. Brinsmead, L. Reedman, Projections for small scale embedded energy technologies - Report to AEMO, Tech. Rep. June (2019).

[176] S. A. Gorji, H. G. Sahebi, M. Ektesabi, A. B. Rad, Topologies and control schemes of bidirectional dc–dc power converters: an overview, IEEE Access 7 (2019) 117997–118019.

[177] Q. Xu, N. Vafamand, L. Chen, T. Dragičević, L. Xie, F. Blaabjerg, Review on advanced control technologies for bidirectional dc/dc converters in dc microgrids, IEEE Journal of Emerging and Selected Topics in Power Electronics (2020).

[178] N. Femia, G. Petrone, G. Spagnuolo, M. Vitelli, Optimization of perturb and observe maximum power point tracking method, IEEE transactions on power electronics 20 (4) (2005) 963–973.

[179] T. Esram, P. L. Chapman, Comparison of photovoltaic array maximum power point tracking techniques, IEEE Transactions on energy conversion 22 (2) (2007) 439–449.

[180] S. Lyden, M. Haque, Maximum power point tracking techniques for photovoltaic systems: A comprehensive review and comparative analysis, Renewable and sustainable energy reviews 52 (2015) 1504–1518.

[181] D. Sera, L. Mathe, T. Kerekes, S. V. Spataru, R. Teodorescu, On the perturb-and-observe and incremental conductance mppt methods for pv systems, IEEE journal of photovoltaics 3 (3) (2013) 1070–1078.

[182] C. Liu, B. Wu, R. Cheung, Advanced algorithm for mppt control of photovoltaic systems, in: Canadian Solar Buildings Conference, Montreal, Vol. 8, Citeseer, 2004, pp. 20–24.

[183] M. Hernes, K. Ljøkelsøy, T. Kleppa, O. Mo, Average model of pwm converter, Sintef Energy Research, www. sintef. no2003 (2003).

[184] A. Saha, S. Chowdhury, S. Chowdhury, P. Crossley, Modeling and performance analysis of a microturbine as a distributed energy resource, IEEE Transactions on Energy Conversion 24 (2) (2009) 529–538.

[185] K. Schmidt-Rohr, How batteries store and release energy: Explaining basic electrochemistry, Journal of Chemical Education 95 (10) (2018) 1801–1810.

[186] D.-J. Lee, L. Wang, Small-signal stability analysis of an autonomous hybrid renewable energy power generation/energy storage system part i: Time-domain simulations, IEEE Transactions on energy conversion 23 (1) (2008) 311–320.

[187] M. Dürr, A. Cruden, S. Gair, J. R. McDonald, Dynamic model of a lead acid battery for use in a domestic fuel cell system, Journal of Power Sources 161 (2) (2006) 1400–1411.

[188] Y. Zhang, Y. W. Li, Energy management strategy for supercapacitor in droop-controlled dc microgrid using virtual impedance, IEEE Transactions on Power Electronics 32 (4) (2016) 2704–2716.

[189] A. Tayyebi, A. Anta, F. Dörfler, Hybrid Angle Control and Almost Global Stability of Grid-Forming Power Converters, arxiv (aug 2020). `arXiv:2008.07661`.
URL `http://arxiv.org/abs/2008.07661`

[190] CIGRE Working Group C6.04, Benchmark Systems for Network Integration of Renewable and Distributed Energy Resources, Cigre technical brochure 575 (2014).

[191] Efficient energy management in smart micro-grids: ZERO grid impact buildings, IEEE Transactions on Smart Grid 6 (2) (2015) 1055–1063. `doi:10.1109/TSG.2015.2392071`.

[192] X. Liu, P. Wang, P. C. Loh, A hybrid AC/DC microgrid and its coordination control, IEEE Transactions on Smart Grid 2 (2) (2011) 278–286. `doi:10.1109/TSG.2011.2116162`.

[193] Y. Zhang, Y. W. Li, Energy Management Strategy for Supercapacitor Virtual Impedance, IEEE Transactions on Power Electronics 32 (4) (2017) 2704–2716.

[194] T. Dragicevic, J. M. Guerrero, J. C. Vasquez, D. Skrlec, Supervisory control of an adaptive-droop regulated dc microgrid with battery management capability, IEEE Transactions on Power Electronics 29 (2) (2014) 695–706.

[195] K. Sun, L. Zhang, Y. Xing, J. M. Guerrero, A distributed control strategy based on DC bus signaling for modular photovoltaic generation systems with battery energy storage, IEEE Transactions on Power Electronics 26 (10) (2011) 3032–3045. doi:10.1109/TPEL.2011.2127488.

[196] J. Park, S. Choi, Design and control of a bidirectional resonant dc-dc converter for automotive engine/battery hybrid power generators, IEEE Transactions on Power Electronics 29 (7) (2014) 3748–3757. doi:10.1109/TPEL.2013.2281826.

[197] M. Kwon, S. Choi, Control Scheme for Autonomous and Smooth Mode Switching of Bidirectional DC-DC Converters in a DC Microgrid, IEEE Transactions on Power Electronics 33 (8) (2018) 7094–7104. doi:10.1109/TPEL.2017.2753845.

[198] Q. Xu, Y. Yan, C. Zhang, T. Dragicevic, F. Blaabjerg, An offset-free composite model predictive control strategy for dc/dc buck converter feeding constant power loads, IEEE Transactions on Power Electronics 35 (5) (2019) 5331–5342.

[199] O. Andrés-Martínez, A. Flores-Tlacuahuac, O. F. Ruiz-Martinez, J. C. Mayo-Maldonado, Nonlinear model predictive stabilization of dc–dc boost converters with constant power loads, IEEE Journal of Emerging and Selected Topics in Power Electronics 9 (1) (2020) 822–830.

[200] J. Neely, S. Pekarek, R. DeCarlo, N. Vaks, Real-time hybrid model predictive control of a boost converter with constant power load, in: 2010 Twenty-Fifth Annual IEEE Applied Power Electronics Conference and Exposition (APEC), IEEE, 2010, pp. 480–490.

[201] S. Yousefizadeh, J. D. Bendtsen, N. Vafamand, M. H. Khooban, F. Blaabjerg, T. Dragičević, Tracking control for a dc microgrid feeding uncertain loads in more electric aircraft: Adaptive backstepping approach, IEEE Transactions on Industrial Electronics 66 (7) (2018) 5644–5652.

[202] Q. Xu, C. Zhang, C. Wen, P. Wang, A novel composite nonlinear controller for stabilization of constant power load in dc microgrid, IEEE Transactions on Smart Grid 10 (1) (2017) 752–761.

[203] L. Benadero, R. Cristiano, D. J. Pagano, E. Ponce, Nonlinear analysis of interconnected power converters: A case study, IEEE Journal on Emerging and Selected Topics in Circuits and Systems 5 (3) (2015) 326–335.

[204] B. A. Martinez-Treviño, A. El Aroudi, E. Vidal-Idiarte, A. Cid-Pastor, L. Martinez-Salamero, Sliding-mode control of a boost converter under constant power loading conditions, IET Power Electronics 12 (3) (2019) 521–529.

[205] S.-C. Tan, Y.-M. Lai, K. T. Chi, General design issues of sliding-mode controllers in dc–dc converters, IEEE Transactions on Industrial Electronics 55 (3) (2008) 1160–1174.

[206] Y. Zhao, W. Qiao, D. Ha, A sliding-mode duty-ratio controller for dc/dc buck converters with constant power loads, IEEE Transactions on industry Applications 50 (2) (2013) 1448–1458.

[207] J. Han, From pid to active disturbance rejection control, IEEE transactions on Industrial Electronics 56 (3) (2009) 900–906.

[208] Zhiqiang Gao, Scaling and bandwidth-parameterization based controller tuning, Proceedings of the 2003 American Control Conference, 2003. 6 (2003) 4989–4996. `doi:10.1109/ACC.2003.1242516`.

[209] W. Xue, W. Bai, S. Yang, K. Song, Y. Huang, H. Xie, ADRC with Adaptive Extended State Observer and its Application to Air-Fuel Ratio Control in Gasoline Engines, IEEE Transactions on Industrial Electronics 62 (9) (2015) 5847–5857. `doi:10.1109/TIE.2015.2435004`.

[210] N. Miller, D. Lew, R. Piwko, Technology capabilities for fast frequency response, GE Energy Consulting, Tech. Rep. (2017).